Isospin influence on the reaction mechanisms in the $^{78}Kr +^{40}Ca$ and $^{86}Kr +^{48}Ca$ collisions at 10 AMeV

TESI DI DOTTORATO

Candidata:
Brunilde Gnoffo

Tutors:
Chiar.ma Prof.ssa. F. Rizzo
Dott.ssa S. Pirrone

a Danilo...l'Amore della mia vita

Contents

Introduction

One of the characteristics which makes unique heavy ions collisions is the possibility to realize a wide variety of reaction mechanisms as Fusion reactions, multifragmentation, Fission, break-up of the projectile and/or of the target, etc...etc . A large number of theoretical and experimental studies were performed in order to investigate the properties of the reaction mechanisms and their dependence on the characteristics of the entrance channel. At low energy one of the most widely studied mechanisms is unquestionably the fusion reaction, with Compound Nucleus (CN) formation and subsequent decay modes. In fact, this process, leading to the formation of nuclei under extreme conditions of temperature and spin, allows the investigation of various aspects characterizing the nuclear matter. Moreover fusion of heavy nuclei is one of the method for the production of transuranium elements. A serious competitor of the Compound Nucleus reactions is Quasifission, a process in which the intermediate di-nuclear system break-ups by passing the stage of Compound Nucleus formation. Thus at low energy in the central collisions, the overlap of contributions of Fusion Evaporation, Fusion-Fission and Quasi-Fission is observed, whereas in semi-peripheral collisions binary deep-inelastic and the break-up of the projectile occur.

At intermediate and low energy the isospin degree plays a crucial role in the competition among different reaction mechanisms, affecting the quantities which influence the fragments production modes, as for example the fission barrier and the level density parameter. The charge distribution exhibit an even-odd effect (*staggering*), explained by considering the pairing force, whereas its oscillation amplitude seems to depend on the isospin degree of freedom. Moreover it is experimentally found that the neutron enrichment influences the ratio between statistical and dynamical fission.

The isospin physics is one of the topic of many experimental campaigns performed inside the scientific program of the CHIMERA group. In particular in the

present thesis I will go to show the results relative to the analysis of the data of the ISODEC experiment, performed in order to study the competition among the various fragment production modes in the reactions $^{78}Kr +^{40}Ca$ and $^{86}Kr +^{48}Ca$, realized at E_{lab} of 10 AMeV. The experiment was realized in Catania, at INFN-Laboratori Nazionali del Sud, by using the 4π multidetector CHIMERA, a powerful tool for the detection of charged particles.

The guideline in the choice of the characteristics of the entrance channel was to obtain the production of compound nuclei with similar spin distribution and excitation energy in a large domain of N/Z. In fact the bombarding energy was chosen in order to ensure the formation of excited systems in a suitable energy range, while at higher excitation energy, the influence of the initial neutron richness could be blurred by a long disintegration cascade. Moreover the chosen combination of projectile and target leads to the formation of composite systems with a big difference in the N/Z ratio.

For the two reactions, elastic scattering measurements are performed to extract the normalization factor used to evaluate the absolute cross sections. The kinematic characteristic and the angular distributions of the reaction products suggest the presence of a relaxed component, related to fusion reaction followed by evaporation or binary decay. Nevertheless signals ascribable to a non equilibrated component are present. Different contribution weights of the various reaction mechanisms have been found for the two systems. The neutron enrichment seems to limit the formation of the composite system and to inhibit the fission decay channel. The data are compared to the theoretical predictions of different models: HIPSE followed by $GEMINI ++$, $GEMINI ++$ and the DNS (DiNuclear System).

A selection method is developed in order to discriminate the breakup of the projectile from the other processes which populate the same region of the phase space. Afterwards the nature of the break-up is investigated by studying the angular distributions of the fragments produced in the splitting of the PLF in the reference frame of their reconstructed source (PLF).

The thesis is organized in the following way: in chapter 1 the physics case is introduced, in chapter 2 the descriptions of the experimental apparatus and of the identification techniques are presented; finally, in chapter 3 the results of the data analysis are discussed.

Chapter 1

Heavy Ion Collisions at low energy

1.1 General features of Heavy Ion Collisions

Heavy ions induced reactions with stable and radioactive beams are a powerful tool for the investigation of the properties of nuclear matter. The study of these reactions is a forefront area of nuclear research, in fact the large palette of the projectiles, ranging from light ions to heavy ions, and the different bombarding energies available, allow the exploration in a wide range of densities and temperatures. Because of the large number of interacting nucleons it is possible to observe a wide variety of processes. Heavy Ion Collisions can completely disintegrate nuclei leading to an explosion of nucleons or nuclear fragments, they can transfer large angular momenta causing fission because of high instability or they can lead to fusion of the two interacting nuclei, making a composite systems and dissipating a large amount of energy into internal excitation energies, then emitted in radiations or particles form. Moreover by using these reactions to make unusual nuclear species, one can also investigate nuclear structure and dynamics at "its limits".

The reaction mechanisms presented in these collisions have a strongly dependence on the bombarding energy and so it is possible to make a qualitative classification based on the energy of the entrance channel. The free mean path λ, which provides the independence of nucleons with respect to each other, is compared to the typical distance between nucleons inside nucleus($\sim 2fm$) [1], in order to have the relative importance of the mean field compared to the nucleon -nucleon collisions.

The so called low energy domain (E≤ 15 AMeV), is dominated by the competition among the formation and the decay modes of the Compound Nucleus and binary processes like Quasi elastic scattering, Quasi Fission and Deep Inelastic Collisions [2, 3, 4]. The fermionic nature of the nucleons leads to a drastic reduction of the nucleon-nucleon in medium cross section because Pauli principle blocks the interaction between nucleons; the large values of λ at low energy, thus, suggest the relevance of mean-field approaches, the nucleus behaves like a set of indistinct nucleons, immersed in the field which they themselves generate.

At high energy (E≥ 100 AMeV), in contrast, the value of λ is small because of the minus importance of the Pauli blocking principle, thus the two body nucleon-nucleon interaction plays the dominant role. In this energy domain the reaction mechanism is governed by participant spectator picture. In the Fire Ball [5], the overlapping zone between projectile and target nuclei, large excitation energy and high nuclear density will be reached.

The intermediate energy regime, placed between these energy regions, calls for a hybrid description. This peculiar energy domain is characterized by the competition between the one-body dissipation energy mechanisms, typical of the low energy, and the two body nucleon-nucleon dissipation mechanism, dominant at high energies [6, 7, 8].

1.2 Reaction mechanisms at low energy

The most important parameter to take into consideration for the application of semiclassical concepts is the de Broglie wavelength $\lambda_B(r)$ of the relative motion between the projectile and the target, which gives a quantification of the more or less quantal nature of the system and it is given from the following expression [9]:

$$\lambda_B(r) = \frac{\hbar}{P(r)} \tag{1.1}$$

where P(r) is the momentum of the relative motion.

In Heavy Ion Collisions $\lambda_B(r)$ is sufficiently short that it may be localised (by building a compact wave packet) in a region small compared to the interaction surface, justifying the use of the semiclassical approach [10]. This description in terms of classical trajectories allows to classify the low energy collision according

to the impact parameter as shown in the scheme of Fig. 1.1 [1].

The impact parameter is defined as the perpendicular distance from the asymptotic trajectory of the projectile, during its approaching to the target, to the parallel line passing trough the center of the target nucleus. The trajectory for which the surfaces of nuclei barely touch is the *grazing trajectory*, characterized by the impact parameter b_{gr}; it plays a crucial role, in fact, it is the first trajectory for which the nuclear field of the target nucleus will begin to come into play.

At large values of the impact parameter ($b > b_{gr}$), in the *distant collisions*,

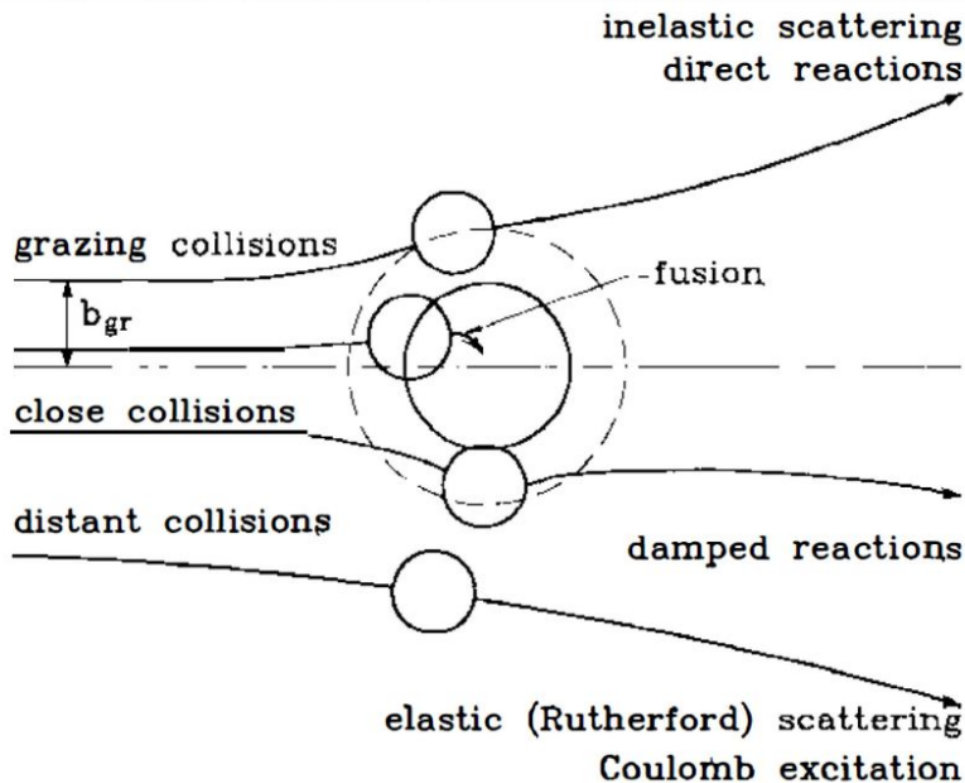Figure 1.1: Classification of the Reaction Mechanisms based on the impact parameter

the Coulomb interaction is the only interaction acting between the projectile and target nuclei. Hence the Rutherford scattering in which, for the conservation of the total energy and momentum, both nuclei remain in their ground states or processes of Coulomb excitation, in which the projectile and/or the target absorb part of the

available energy, take place. The elastic scattering is the main reaction channel at all energies and the probability for a nucleus to be deflected approaching each other is described from the Rutherford formula [11]:

$$\frac{d\sigma_{Ruther}}{d\Omega} = \left(\frac{Z_p Z_t e^2}{2\mu v^2}\right)^2 \frac{1}{sin^4\left(\frac{\theta}{2}\right)} \tag{1.2}$$

When ($b \sim b_{gr}$) the trajectories after the collision are decided from the competition between the Coulomb force and the nuclear interaction. These collisions, called *direct reactions*, occur very quickly, with times less than 10^{-22} s, and with a limited exchange of energy, mass, charge and angular momentum; the reaction products are focused around the beam direction. The most important examples are the *stripping* and *pick-up reactions*. The former are nuclear reactions in which one or more nucleons of the projectile nucleus, are stripped and transferred to the target nucleus. In the latter, in contrast, the projectile captures some nucleons from the target.

At small values of the impact parameter ($0 < b < b_{gr}$) it is possible to observe *the central collisions* and the *close collisions*, characterized from a high dissipation of energy. The dominant processes are *Compound Nucleus reactions*, *Quasi-Fission* and *Deep Inelastic Collision*.

The *Compound Nucleus reaction* is a two step mechanism. In the first step there is the formation of an excited system, made by the nucleons of the projectile and the nucleons of the target, called *Compound Nucleus*. Then the system decays, with emission of light fragments, or through *Fission*.

In *Quasi-Fission* the initial dinuclear system evolves toward a dinuclear configuration in which there is a partial mass equilibration without the formation of *Compound Nucleus*.

In *Deep Inelastic Collision* the initial binary character of the collisions is conserved, the formed systems have large angular momenta, that will be dissipated from the centrifugal forces. They will perform a partial rotation around the center of mass and then they will separate.

We are interested in the most dissipative reaction mechanisms and for this reason in the next sections the *Compound Nucleus reactions*, *Quasi-Fission* and *Deep Inelastic Collision* will be described in details.

In Fig. 1.2 [1]a schematic view of the components of the partial cross section $d\sigma(l)/dl$ as function of the angular momentum (l) is shown.

The classical differential cross section, as partial waves expansion, is given by [10]:

$$\sigma(l) = \frac{d\sigma}{dl} = 2\pi \lambdabar^2 l \tag{1.3}$$

In the *sharp cut-off model*, despite the expected smooth transition across l_{gr}, the absorption is zero for $l > l_{gr}$, thus all values of the orbital angular momentum (l) up to the *grazing* angular momentum contribute to the reaction cross section σ_R, obtaining the following expression:

$$\sigma_R = \int_0^{l_{gr}} dl \frac{d\sigma}{dl} = \pi \lambdabar^2 l_{gr}^2. \tag{1.4}$$

According to Quantum Mechanics it should have been used $(l_{gr} + 1)^2$ but for $l_{gr} \gg 1$(condition easily to meet in Heavy Ion Collisions) the approximation $(l_{gr} + 1)^2 \sim l_{gr}^2$ is valid.
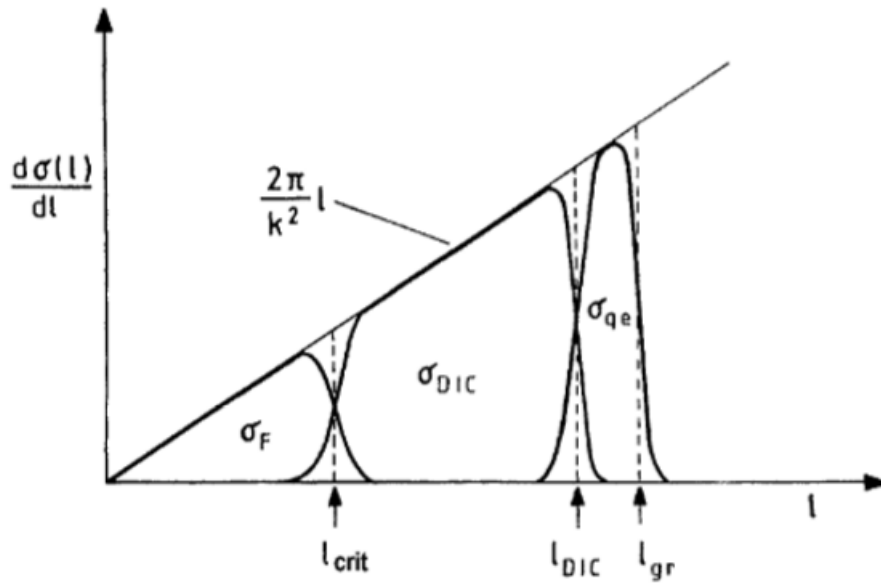

Figure 1.2: Reaction Mechanisms cross section as function of the angular momentum

Vertical dashed lines indicate the extensions of the various l windows in a sharp

cutoff model with the characteristic l values noted at the abscissa, while the smoothed areas represent the diffuse l windows assumed in a smooth cutoff model. We can distinguish three zones among the contributions of the different reaction mechanisms to the reaction cross section. When $l_{crit} < l < l_{DIC}$ the *Deep Inelastic Collisions* occur, for $l < l_{crit}$ we observe the *Compound Nucleus reactions* and for $l_{DIC} < l < l_{gr}$ we find the *Quasi-Elastic collision*. The grazing angular momentum l_{gr} is defined as the angular momentum for which the distance of the closest approach for a Coulomb trajectory is equal to the sum of the nuclear radii ($R_{gr} = r_0(A_1^{1/3} + A_2^{1/3})$), while l_{crit} is the angular momentum for which the pocket, in the potential energy curve, disappears.

1.2.1 Close and Central Collisions

.

The main components of the reaction mechanism can be understood in terms of the effective interaction nuclear potential between the colliding nuclei (an example in Fig. 1.3) [9], which has this following expression [1]:

$$V_l^{eff}(r) = V_N(r) + V_{CB}(r) + V_{centr}(r) \qquad (1.5)$$

It consists of the sum of the nuclear, Coulomb and centrifugal potentials.
The nuclear potential $V_N(r)$ acts within the volume occupied from the ions and it exponentially falls off outside. It gives an attractive contribution at small distance and it becomes repulsive when the two colliding nuclei significantly overlap.
The repulsive contribution of the Coulomb potential between two ions is described as the potential between a point charge and a uniform spherical charge distribution of radius R:

$$V_{CB}(r) = \begin{cases} \frac{1}{4\pi\epsilon_0} \frac{Z_1 Z_2 e^2}{2R_{gr}} \left(3 - \frac{r^2}{R_{gr}^2}\right) & r \leq R_{gr} \\ \frac{1}{4\pi\epsilon_0} \frac{Z_1 Z_2 e^2}{r} & r \geq R_{gr} \end{cases}$$

The centrifugal potential takes into accounts the difficulty of ions that carry large angular momenta to approach each other. It can be expressed as :

$$V_{centr}(r) = \frac{\hbar^2 l(l+1)}{2\mu r^2} \qquad (1.6)$$

Only scattering is possible for very heavy systems and for light systems at high
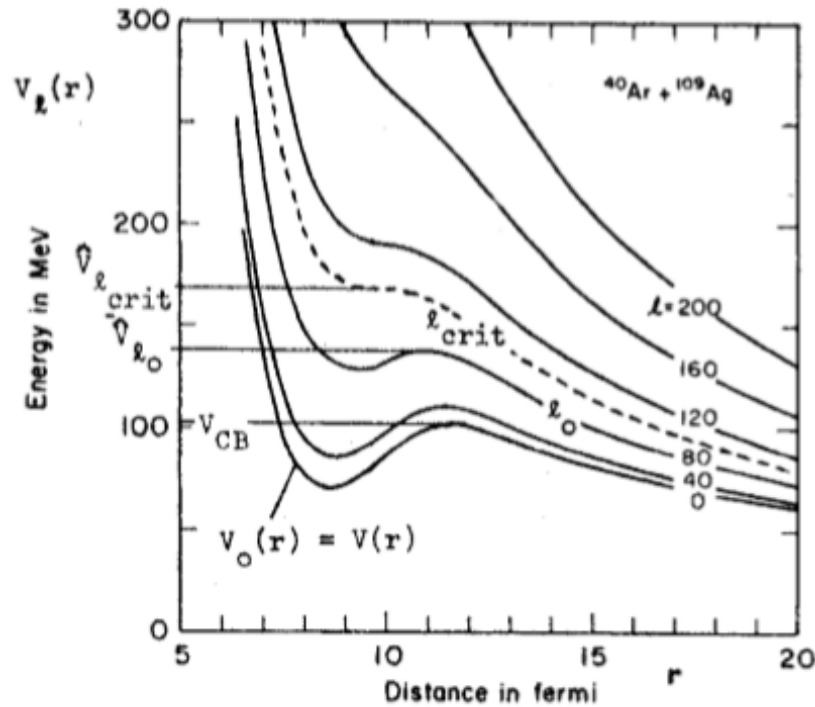
Figure 1.3: Interaction potential vs distance, for different values of the angular momentum in the reaction $^{30}Ar + ^{109}Ag$

angular momenta; in fact the pocket, due to the attractive part of the neutron potential, can be destroyed or by increasing the size of the ions and consequently the Coulomb forces or by increasing the angular momentum causing the filling of the pocket with the centrifugal potential. Obviously, the strength of the dissipative forces plays an important role too. Friction forces, which cause the loss of the initial kinetic energy of the two reaction partners, can be divided into two components: the radial one and the tangential one. Fig. 1.4 [12] displays the effect of the radial friction on the particle trajectory having energy E. While for a moderate value of the radial friction (dotted curve) the system can get trapped in the pocket of the effective potential, for a weak (solid line) and large (broken curve) radial friction, the trajectory is reflected outside the barrier, leading to scattering. The effect of the tangential friction is the reduction of the effective potential because of the loss of the relative angular momentum but on the other hand it may also
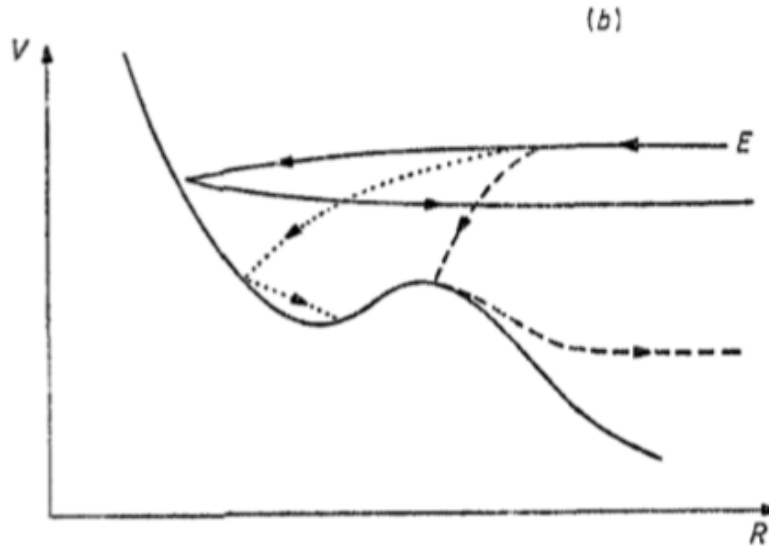
favor the trapping.

Figure 1.4: Effect of radial friction on trajectory with energy E

Two reacting nuclei, in order to make contact, must overcome both Coulomb and centrifugal barriers. *Deep Inelastic Collisions* (DIC) occur when the Coulomb and centrifugal fields are not sufficiently small to lead the di-nuclear systems to fuse. The interacting nuclei will instead separate not dramatically modified, after staying in contact for a relatively long time, during which the combined system rotates with a period smaller than the time for a complete revolution ($10^{-21} \div 10^{-20}$). In contrast after surmounting the Coulomb barrier, the reactants, trapped in an attractive potential pocket, produce a composite di-nuclear system. This system can evolve towards a full equilibrated configuration, the *Compound Nucleus* (CN), which then substantially decays or via evaporation of light particles or through fission, or the di-nuclear system can break-up in fission like events before achieving complete equilibration of all degree of freedom, giving *Quasi-Fission* (QF). Along the years a large amount of experimental and theoretical investigations of key observables (mass distributions, kinematic characteristics, etc...) were performed, in order to study the *DIC, CN and QF* and the salient aspects emerged are described below.
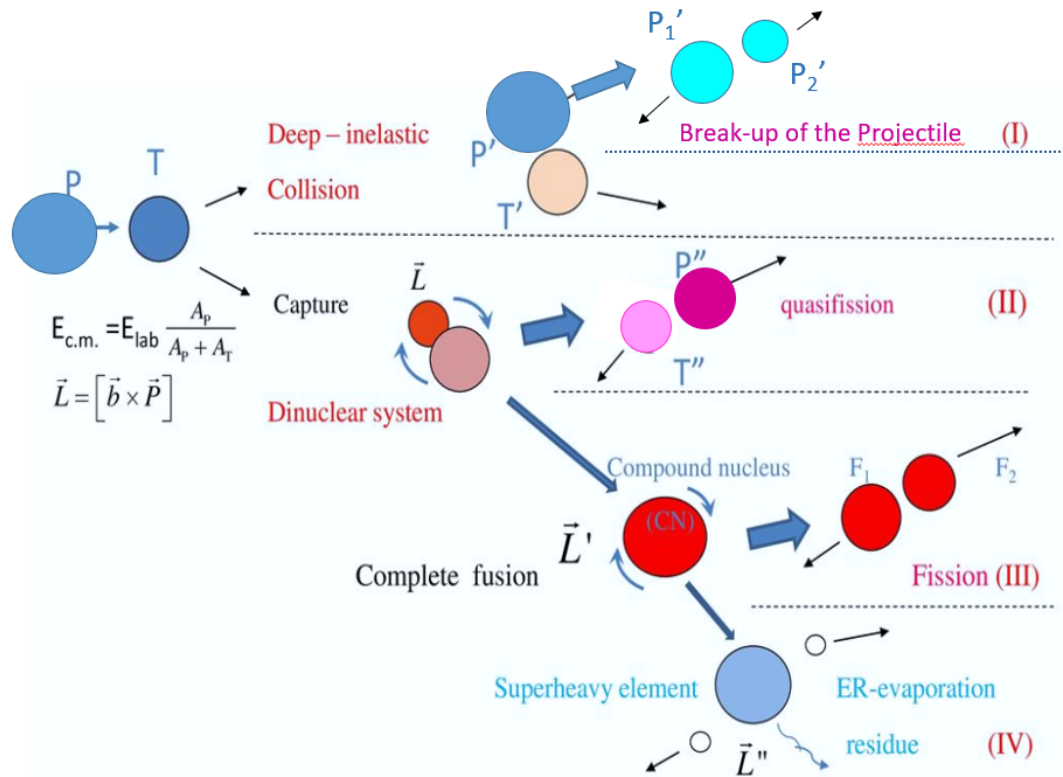
Figure 1.5: Schematic view of the reaction mechanisms of interest

(I) Deep Inelastic Collisions

Heavy ions collisions are characterized by very large losses of energy, this is emphasized by the use of the terms like deep inelastic collisions and strongly damped reactions. The reaction products exhibit different degrees of damping of the entrance channel kinetic energy, varying from zero to very large values. This wide range of energy loss from the relative motion in internal degrees of freedom is evident in the energy spectra Fig. 1.6 a). In general in the energy spectra of fragments with charge close to that of the projectile, it is possible to distinguish between two component, a high-energy or quasi-elastic component and a low-energy or relaxed component. Increasing the mass transfer, either to or from the projectile, the contribution of the elastic component progressively decreases and eventually disappears. For angles very far form the grazing angle the relaxed component is

dominant and the energy spectra consist of just of a gaussian-shaped peak. This is also evident in the so called *Wilczynski plot* Fig. 1.6 b) [13], where the differential cross section $\frac{d^2\sigma}{d\Theta dTKE}$ is shown in the plane TKE and Θ_{cm}, both quantities referred to the primary fragment. We can observe the quasi-elastic ridge moving from elastic energies at the grazing angle towards lower kinetic energies at smaller angles.
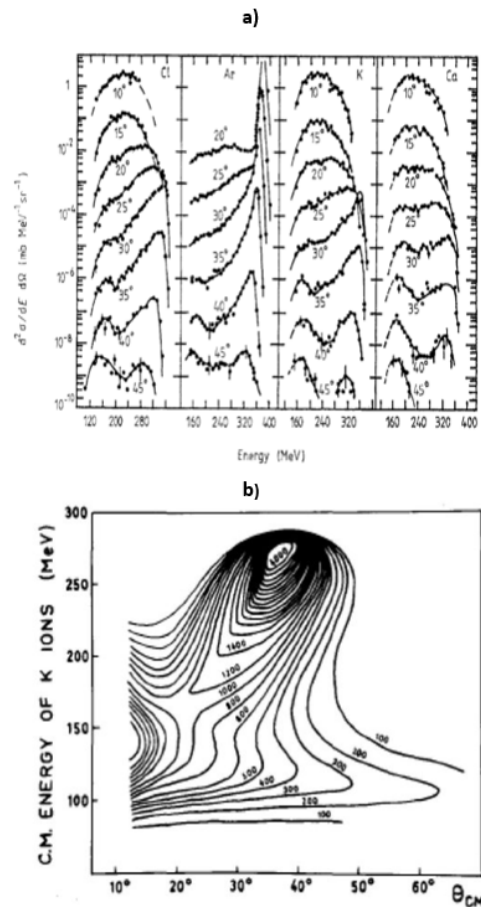

Figure 1.6: For the reaction $^{40}Ar + ^{232}Th$ a) energy spectra for various reaction products, at different angles and b) Contours of constant cross section in the energy-angle plane for potassium ions.

A possible explanation of the behavior exhibited by the energy spectra and the *Wilczynski plot* was proposed by J. Wilczynski Fig. 1.7 [13].

For angular momenta close to the maximum the two nuclei barely overlap and
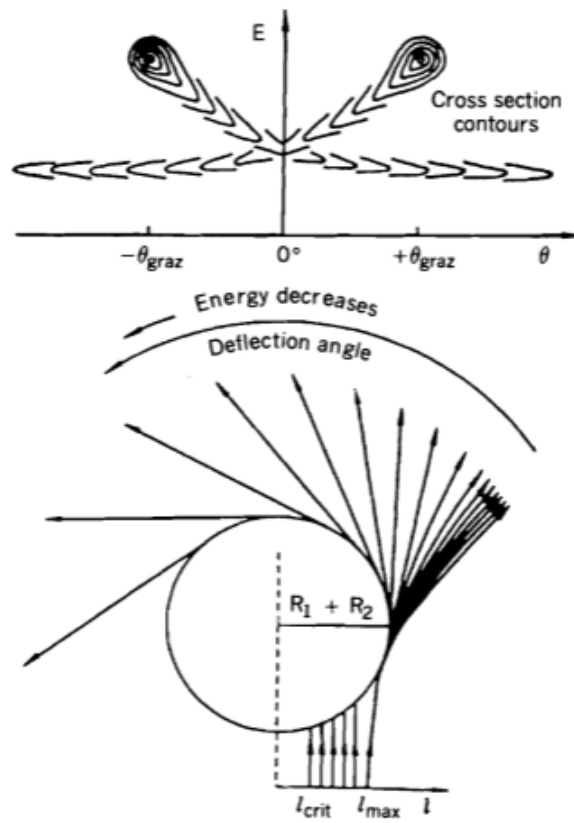
Figure 1.7: Interpretation of the energy spectra and of the Wilczynski plot proposed by J. Wilczynski

grazing collisions occur, so the two nuclei with kinetic energies and masses not modified appreciably, continue along Coulomb- like trajectories. Hence, the yield for these quasi-elastic products are concentrated around the grazing angle. In contrast the trajectories are more strongly altered for smaller impact parameters because of the more intimate contact between the nuclei. The nuclear interaction will become more important and a stronger damping of the kinetic energy and more extensive mass transfer were observed. In this case the trajectories will be bent towards zero degrees. At still lower partial waves negative angle scattering

and even orbiting can occur [14]. Negative and positive angles are not distinguishable by the detectors, so that as the reaction angle passes zero, the cross sections will be recorded as positive, resulting in the two overlapping ridge as shown in the *Wilczynski plot*.

Orbiting occur for light systems while very heavy systems are 'Coulomb-dominated', in fact the inter-nuclear potential tends to become repulsive because of the strong Coulomb forces. The *Wilczynski plot*, in this case, as shown for the reaction $^{209}Bi + ^{136}Xe$ at 1130 MeV in Fig. 1.8 [15], exhibits a vertical quasi-elastic ridge rather then oblique.
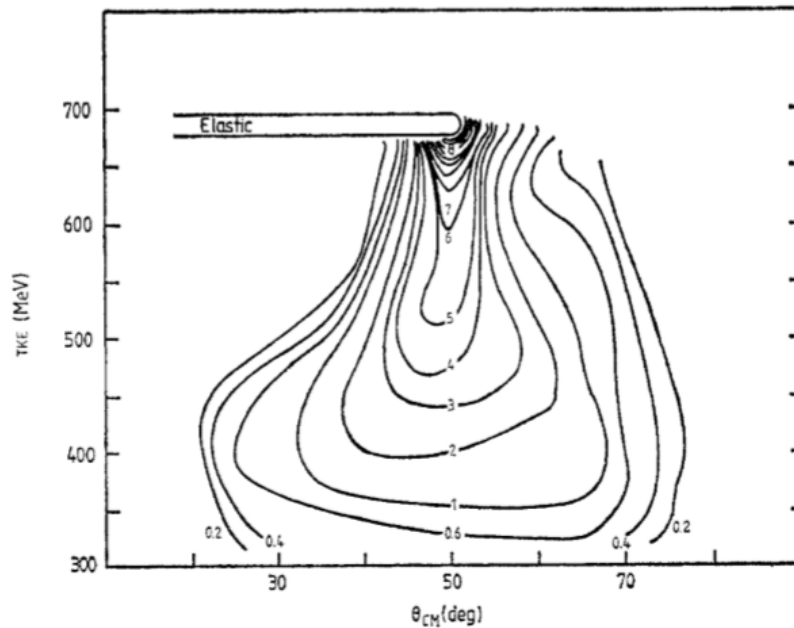
Figure 1.8: Wilczynski plot for the reaction $^{209}Bi + ^{136}Xe$ at 1130 MeV

One can note that the two fragments in which the system splits in the primary process, essentially binary in nature, called *Projectile* and *Target Like Fragment* (PLF and TLF) are emitted with velocity quite similar to the velocity of the Projectile and the Target. This primary fragments de-excite largely through the evaporation of light particles (n, p, a) and γ-rays, and occasionally via fission, which is the process we are interested in. The scenario of this two step mechanism, where one or both of the primary fragments undergoes fission, was largely studied.

(II)(III)(IV) Capture Reactions

At smallest impact parameters the capture reactions occur. These central collisions are characterized from the largest dissipation of energies and a large compression because of the considerable overlap between the two reacting nuclei. Capture reactions are the set of Compound Nucleus reactions and Quasi-Fission, in fact in deep inelasic collisions the dinuclear system is formed but without the full momentum transfer and thus they are not considered capture reactions According to the Bohr hypothesis [16], as mentioned before, the Compound Nucleus reactions can be described as a two-stage process. First the completely equilibrated intermediate system, known as Compound Nucleus, is formed by the complete absorption of the projectile from the target nucleus, in very dissipative reactions, with interaction times longer then thermalization time. The merging of all the nucleons of the two participating nuclei is the result of a strong friction between them. Second the compound nucleus disintegrates without any memories of the entrance channel except for the restrictions imposed from the conservation of the angular momentum, energy and parity.
The Kinetic energy dissipated into degree of freedom, lead to the formation of the compound nucleus as highly excited system. The excitation energy E^* of the compound nucleus, at a given center of mass bombarding energy $E_{c.m.}$, has the following expression:

$$E^* = E_{c.m.} + Q_{fus} \qquad (1.7)$$

Q_{fus} [17] is the $Q-value$ associated with the formation of the Compound nucleus and given by the difference between the masses of the reacting nuclei and the mass of the compound nucleus $Q_{fus} = (M_p + M_t - M_{CN}) * c^2$. The values of Q_{fus} and E^* for the reaction object of interest of this work of thesis are shown in Table 1.1.
  The Compound Nucleus is produced in a highly excited state and can dexcite or via evaporation of light particles or through fission. In the evaporation process, the so called "*evaporation residues*"(ER), are produced, with masses slightly lower than the sum of the masses of the projectile and the target nuclei, and moving forward because of *full momentum transfer* (FMT). The neutron emission is, in general, preferred to that of charge particles, because of the absence of the Coulomb barrier to overcome. Obviously cascade emission are allowed until the excitation energy of the Compound Nucleus is not below of threshold of particles

Reaction	CN	$E_{c.m.}$ (MeV)	Q_{fus} (MeV)	E^* (MeV)
$^{78}Kr + ^{40}Ca$	^{118}Ba	264.41	−46.67	217.74
$^{86}Kr + ^{48}Ca$	^{134}Ba	308.06	−38.54	269.52

Table 1.1: Excitation energy and Q-value for the reactions $^{78}Kr + ^{40}Ca$ and $^{86}Kr + ^{48}Ca$ at 10 AMeV

.

emission. If the evaporation residue remains in an excited state, will tend to return to the ground state through γ emissions. Recently the study of the mechanism of evaporation has attracted the interest of the physics community because it plays a key role in the *super-heavy elements* synthesis.

Evaporation Residues can be populated by the so called incomplete fusion, process without the full momentum transfer, where the mass of the "reduced" CN formed is less than the total mass of the system and the velocities of the evaporation residues and of the fission fragments are different from those of the fragments emitted subsequent to complete fusion. In this process, in the early stage of the collision, the projectile and/or the target may lose cluster of nucleons, emitted as light fragments, which remove an appreciable part of the kinetic energy initially carried by the entire projectile. After the fusion of the remnants of the two colliding nuclei a complete statistical equilibrium of the merging nucleons is achieved. An estimate of the contribution of incomplete fusion could be extracted from the Morgenstern systematic [18].

Another decay mode is Fusion followed by Fission (FF). In fission the excited compound nucleus deforms to a configuration, known as *"transition state" or "Saddle point"* configuration. The deformation lead to an increasing in the surface energy (as the surface area increases) and to a decreasing of the Coulomb energy (because of the higher average distance between the nuclear protons). The Coulomb repulsion between protons decreases faster with elongation than the surface tension increases, and the two are in balance at the saddle point, which represents the height of the barrier to fission. If the nucleus deforms beyond this point, the neck between the two fragments disappears and at the scission point the nucleus break-ups into two fragments.

Serious competitors for the compound nucleus formation are Fast-Fission (fast-fiss) and Quasi -Fission (QF) processes. It should be underlined that in literature a unique definition of these processes and thus a common idea about their physical origin, do not exist. In fact some authors use fast- fission and quasi-fission as different names to indicate the same process [19]. Others authors [20]consider quasi-fission as a process in which the di-nuclear system break-ups bypassing the stage of Compound Nucleus formation, and fast-fission as the inevitable decay of the fast rotating mononucleus, into two fragments. At value of the angular momentum larger than l_B, that is the value at which the fission barrier of the corresponding compound nucleus disappears, the mononucleus decay immediately trough fast-fission, fusion-fission occur for $0 < l < l_B$, quasi fission can occur at all values of l at which capture occurs. In Fig. 1.9is displayed a schematic view of Fusion-Fission, Quasi Fission and Fast Fission processes.
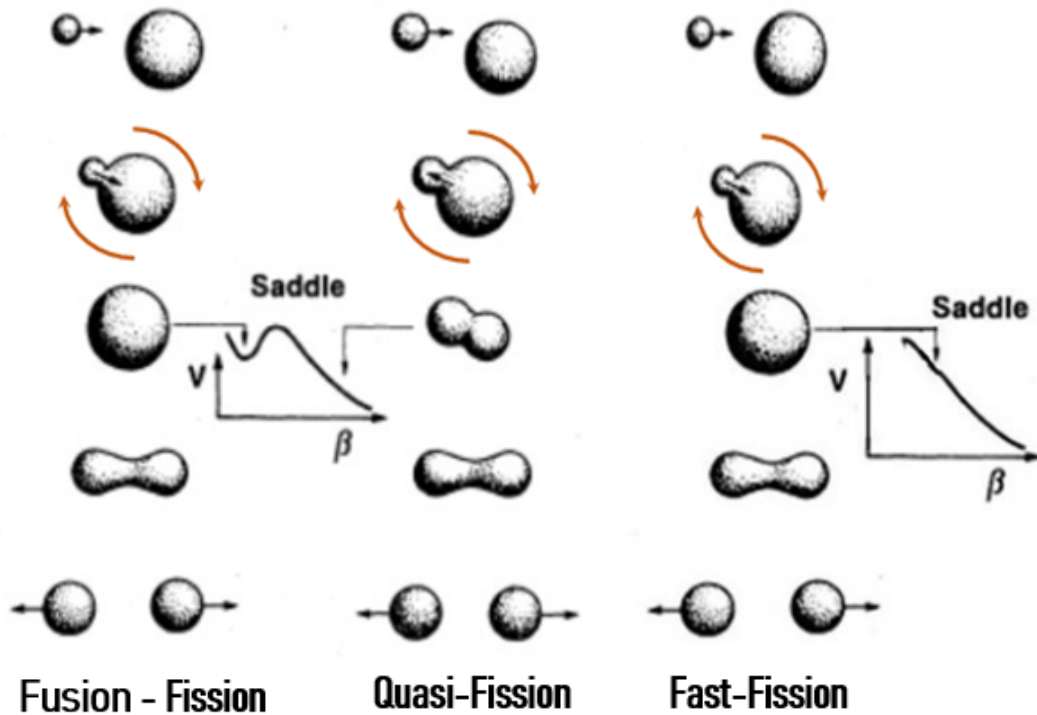

Figure 1.9: Schematic view of Fusion-Fission, Quasi Fission and Fast Fission

In the landscape of the theory of the Liquid Drop Model [21], it is possible to explicit the dependence of fission barrier on the mass and charge, as well displayed by the Fig. 1.10 (a) [22], where the calculated fission barrier heights are shown as function of mass for different isotopes for atomic numbers from 20 to 90 for nonrotating nuclei.
The probability of fission relative to the other decay channels is affected by the height of fission barrier, and strongly depends on the considered region of masses and on the angular momentum. Light composite systems, because of high stability against fission, dexcite mainly via evaporation of light particles. For heavy systems fission barrier is low, and thus fission dominates on the other decay modes. For intermediate mass systems, competition between evaporation of light particles and fission strongly depends on the angular momentum. In fact in this region of masses, as shown in Fig. 1.10 (b) [22], we can observe the highest values of angular momentum at which the saddle point disappears and the barrier goes to zero (maximum angular momentum). This is one of the reasons why the reactions realized with intermediate mass systems have attracted the interest of the scientific community.
 Another source of limitation in the Compound Nucleus formation, is the existence of the *Yrast-line*, which represents the maximum rotational energy that a nucleus can get without disintegrating. At a given excitation energy, the *Yrast-line* is the locus of states with maximum angular momentum.

Fusion-Evaporation, Fusion-Fission, Quasi- Fission and Fast-Fission are full momentum-transfer processes and thus their contributions are included in the theoretical cross section for capture reactions.

$$\sigma_{cap}(E_{c.m.}) = \sigma_{ER}(E_{c.m.}) + \sigma_{FF}(E_{c.m.}) + \sigma_{QF}(E_{c.m.}) + \sigma_{fast-fiss}(E_{c.m.})$$

$$(1.8)$$

Where $\sigma_{cap}(E_{c.m.})$, $\sigma_{ER}(E_{c.m.})$, $\sigma_{FF}(E_{c.m.})$, $\sigma_{QF}(E_{c.m.})$, $\sigma_{fast-fiss}(E_{c.m.})$ are the cross sections respectively for capture reactions, Fusion-Evaporation, Fusion-Fission, Quasi-Fission and Fast-Fission.
The pure cross sections of the Compound Nucleus should be given by the fragments yields from Fusion-Evaporation and Fusion-Fission processes ($\sigma_{CN}(E_{c.m.}) = \sigma_{ER}(E_{c.m.}) + \sigma_{FF}(E_{c.m.})$), but experimentally fission-like (FL) fragments can be a mixture of the contribution of Fusion-Fission (σ_{FF}), Quasi- Fission (σ_{QF})
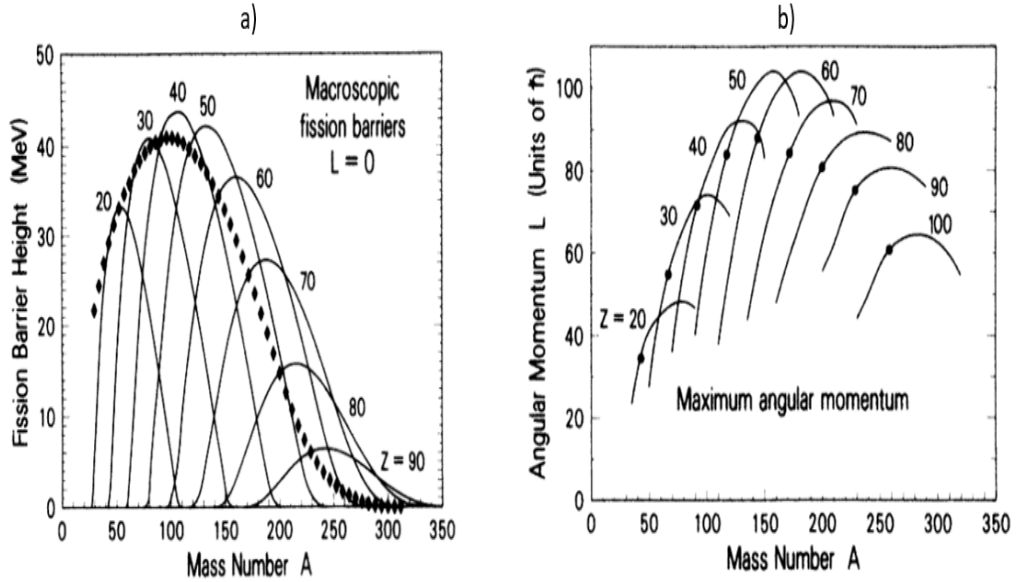
Figure 1.10: (a) Calculated fission barrier heights as function of Z and A for l=0. (b) maximum angular momentum as function of A for Z=20 to 100. The solid points indicate beta-stable nuclei

and Fast-Fission ($\sigma_{fast-fiss}$) and it is very difficult experimentally to distinguish among these various reaction mechanisms because they present similar kinematic characteristic .

$$\sigma_{CN}^{(exp)} = \sigma_{ER} + \sigma_{FL} \tag{1.9}$$

1.3   ISODEC experiment

In this work of thesis I will report the results relative to the ISODEC experiment [24, 23, 4], realized in order to study the isospin influence on the competition among the various fragment production modes in the reactions $^{78}Kr + {}^{40}Ca$ and $^{86}Kr + {}^{48}Ca$ at a laboratory energy of 10 AMeV. In fact, the $\frac{N}{Z}$ ratio in the entrance channel is closely related to the isospin degree of freedom and can influence both the reaction mechanisms and the production of fragments in the exit channel. The ISODEC experiment was performed in Catania, at the INFN-Laboratori Nazion-

ali del Sud, by using the CHIMERA multidetector [25] (described in details in the second chapter), a powerful 4π array for charge and mass identification of reaction products with low energy threshold. At INFN-LNS we also took advantage of the high quality beams, delivered by the Superconductive Cyclotron, with both intensity and timing characteristics suitable for the experiment. The beam current intensity was tuned at 0.8–1enA, value chosen to maintain a low probability for pile-up, and data acquisition dead time was kept below 25%. The pulsed beam was delivered with the timing resolution in the range 800ps–1ns, allowing for a global time resolution of 1– 1.2ns. Self-supporting ^{40}Ca and ^{48}Ca targets, 1mg/cm^2 thick, were made by rolling of high purity foils in a collaboration between INFN-LNL and INFNLNS Target Laboratories. The contaminants, mostly oxygen and tantalum, were checked during the data analysis and found to be negligible. The products were measured event-by-event, using a first level trigger based on the number M of fired telescopes during the acquisition. We used $M \geq 1$ for the elastic scattering measurements and $M \geq 2$ to collect the events for the reactions of interest. Energy and time calibration measurements were performed by using$^{12}C,^{16}O$ and proton beams, delivered by the Tandem SPM of the LNS, at incident energy ranging from 10 to 100 MeV, with step $\Delta E = 20$MeV, impinging on $200\mu gr/cm^2$ thick Au target. Energy calibration of the detectors ensured an accuracy of1%for Si detectors and within 5% for the CsI(Tl) detectors. This combination of beam and target lead to the formation of two isotopes of Barium which differ by 16 neutrons, the maximum difference in neutrons achievable with stable beams. For this reason, from now, I will refer to the system produced in the reaction $^{78}Kr +^{40}Ca$ as neutron-poor system and as neutron-rich system to the one produced in $^{86}Kr +^{48}Ca$. The bombarding energy was chosen in order to ensure the formation of excited systems in a suitable energy range. At higher excitation energy, the influence of the initial neutron richness could be blurred by a long disintegration cascade. This permits the production of compound nuclei with similar spin distribution and excitation energy in a large domain of N/Z. The main characteristics of the two systems, such as the neutron to proton ratio $\frac{N}{Z}$, the center of mass energy over the Coulomb barrier $\frac{E_{c.m.}}{V_{C.B.}}$ and the grazing angular momentum (l_{graz}, estimated by semiclassical- considerations) are tabulated in Table 1.2.

Reaction	CN	$\frac{N}{Z}$	$\frac{E_{c.m.}}{V_{C.B.}}$	l_{graz} ($\hbar$)
$^{78}Kr + ^{40}Ca$	^{118}Ba	1.11	2.90	158
$^{86}Kr + ^{48}Ca$	^{134}Ba	1.39	3.41	190

Table 1.2: Main characteristics of the reactions $^{78}Kr + ^{40}Ca$ and $^{86}Kr + ^{48}Ca$ at 10 AMeV

.

Chapter 2

The CHIMERA detector
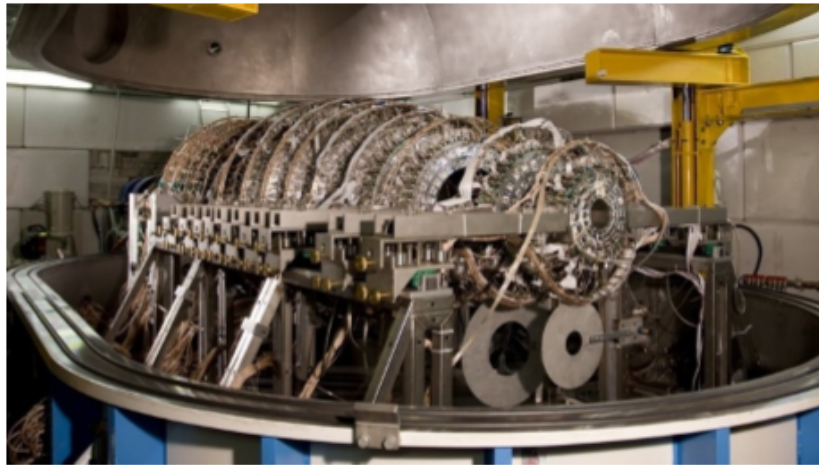
Figure 2.1: a photo of the CHIMERA device in its vacuum chamber at INFN-Laboratori Nazionali del Sud

Key observables in the ISODEC experiment are cross sections, charge distribution, angular distributions, multiplicities and velocities. The precise measurements of these quantities require a 4π solid angle coverage, high granularity and low energy threshold.
Due to its high performance we used the CHIMERA device, installed at INFN-Laboratori Nazionali del Sud in Catania, and shown in Fig. 2.1 in its vacuum chamber.

The CHIMERA (**C**harged **H**eavy **I**on **M**ass and **E**nergy **R**esolving **A**rray) array [24, 25, 26] has been operating for a long time and has proven its capabilities to provide accurate results in the intermediate energy regime (E = 10–100 AMeV), characterized by final states with a large number of charged products, that populate a broad energy range. The device consists of 1192 telescopes, each one made of a Silicon detector, followed by a Cesium Iodide Thallium activated scintillation detector, coupled to a photodiode. The telescopes are arranged in cylindrical geometry around the beam axis direction, covering the polar angle between 1° and 176° and the total azimuthal angle.

Thanks to the accurate study of the structure and to the compactness of the modules, the geometrical efficiency of CHIMERA is really high. In fact, by considering the entrance and the exit holes, the supports of each detector and of the target, the detectors of CHIMERA cover the 94% of the total solid angle.

2.1   Basic characteristics of the apparatus

The CHIMERA device is a set of 1192 telescopes, arranged in 35 rings in a cylindrical geometry along the beam axis, with a total length of 4 m. The mechanical structure of CHIMERA consists of two parts (Fig. 2.3). The forward one is made of 688 modules, covering the polar angle ranges $1° - 30°$, assembled in 18 rings, grouped in couples and supported by 9 wheels. The distance of each ring varies from 350 to 100 cm, with increasing the polar angle. In the backward part, which covers the polar angles between 30° and 176°, 504 modules, grouped on 17 rings, are assembled in such way to composite a sphere of 40 cm in radius. The apparatus works under vacuum.

In Fig. 2.2 the distance to the target, the minimum and maximum polar angle, the number of modules, the opening in azimuthal angle and the solid angle covered by a single module with the corresponding surface are reported for each ring. The number of modules in which each ring is divided is different. This subdivision responds to the need to reduce the solid angle subtended by each individual detector located in the forward part of the device, in which the telescopes have a higher probability to be hit by the particles. The rings, placed near to the target (6-9) have high module sectioning in order to have high granularity, which lowers the probability of "multi-hit" events on the same detector and allows to obtain a remarkable precision in the measurement of polar and azimuth detection angles.

Wheels	Ring	Dist. (cm)	Θmin (deg)	Θmax (deg)	Modules	ΔΦ(deg)	Surface (cm²)	ΔΩ (mSr)/(singlemodule)
1	1	350	1.0	1.8	16	22.5	16.3	0.13
	2		1.8	2.6			25.6	0.21
2	3	300	2.6	3.6	24	15	22.2	0.25
	4		3.6	4.6			29.3	0.33
3	5	250	4.6	5.8	32	11.25	23.3	0.37
	6		5.8	7.0			28.6	0.46
4	7	210	7.0	8.5	40	9	24.2	0.55
	8		8.5	10			29.1	0.66
5	9	180	10	11.5	40	9	24.8	0.77
	10		11.5	13			28.2	0.87
6	11	160	13	14.5	48	7.5	20.8	0.81
	12		14.5	16			23.1	0.90
7	13	140	16	18	48	7.5	26.2	1.34
	14		18	20			29.1	1.49
8	15	120	20	22	48	7.5	23.6	1.64
	16		22	24			25.7	1.78
9	17	100	24	27	48	7.5	29.5	2.95
	18		27	30.0			32.7	3.27
10	19	40	30.0	38.0	32	11.25	24.5	15.33
11	20	40	38.0	46.0	32	11.25	29.3	18.34
12	21	40	46.0	54.0	32	11.25	33.6	21.0
13	22	40	54.0	62.0	32	11.25	37.2	23.25
14	23	40	62.0	70.0	32	11.25	40.1	25.05
15	24	40	70.0	78.0	32	11.25	42.2	26.35
16	25	40	78.0	86.0	32	11.25	43.4	27.15
17	26	40	86.0	94.0	32	11.25	43.9	27.42
18	27	40	94.0	102.0	32	11.25	43.4	27.15
19	28	40	102.0	110.0	32	11.25	42.2	26.35
20	29	40	110.0	118.0	32	11.25	40.1	25.05
21	30	40	118.0	126.0	32	11.25	37.2	23.25
22	31	40	126.0	134.0	32	11.25	33.6	21.0
23	32	40	134.0	142.0	32	11.25	29.3	18.34
24	33	40	142.0	150.0	32	11.25	24.5	15.33
25	34	40	150.0	163.0	16	22.50	56.7	35.45
26	35	40	163.0	176.0	8	45.00	50.9	31.79

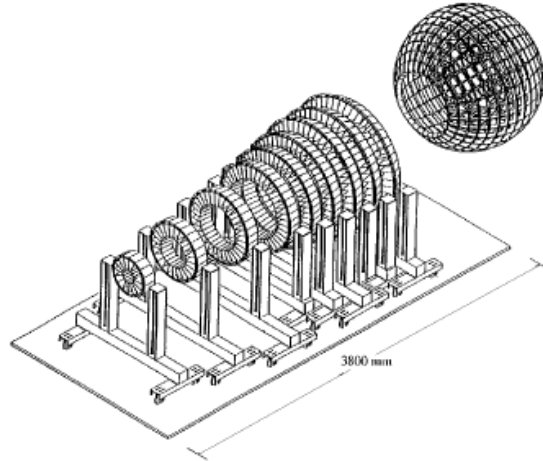Figure 2.2: Relevant features of the CHIMERA device

Figure 2.3: schematic view of the CHIMERA multidetector

2.2 The telescopes

2.2.1 Silicon detectors

The good energy resolution, the quick response times, the relatively low costs, the compact dimensions and the linearity of the response function are the features for which, silicon detectors have been widely used in nuclear physics.

The silicon detectors used in CHIMERA are trapezoidal in shape and made with planar technology [27]. This manufacturing technique allows to obtain detectors with well defined thickness and active zones, as well as exceptionally homogeneous and very thin (500 Å) junction. To ensure a good electrical contact, on the front and rear surfaces of the detector, a thin layer of aluminum (300 Å) was evaporated. This characteristic slightly weakens the energy resolution, introducing a dead layer. However, it improves the time performance of the detector because the rise time of the signal becomes independent of the impact point [28]

The temporal response is also improved by the high electric field within the detector. The junctions are oriented towards the target, with the the highly ionizing particles, which stop in the silicon, hitting in the area with the highest electric field. In this way the charge collection is optimized.

The need to work with high values of the electric field requires that the voltage
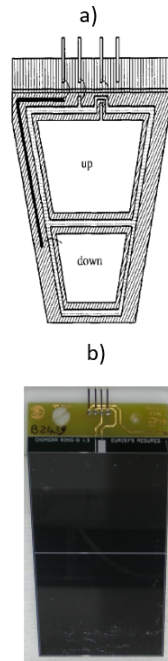
Figure 2.4: a) schematic view and b) picture of Si detector of the rings in the forward part

applied is greater than the one needed for the full depletion of the detector; therefore, the detectors are powered by a voltage 30% higher than the nominal value. The geometry of the silicon detectors changes according to the position they occupy in the apparatus. For the telescopes of the forward part, each cell of the wheels houses two telescopes and thus two silicon detectors (internal and external detector). In order to minimize dead layer, two active zones were obtained from a single slice (wafer) of silicon. Both areas are surrounded by a guard ring, placed at 50 μm and obtained in the dead layer due to passivation of planar technology. The guard ring, in addition, to reduce the surface inverse current, delimits an uniform electric field inside the detector, avoiding the effects on the signal, due to a non-complete depletion of the zones close to the borders. A thin aluminum strip, placed near the guard ring, allows to pick up the signal from the internal detector and avoids the use of external components that would increase the dead layer. Figure Fig. 2.4 a illustrates the non-scaled scheme of a silicon detector of the type of the ring of the forward part: it is possible to see the two active zones,

the guard ring, the aluminum track and the PBC holder for the electrical and mechanical connection of the detector. Fig. 2.4 b shows, as an example, a photo of the detector.

Sphere detectors have a single active zone for each block, also surrounded in this case by a dead layer 500 μm thick, in which the guard ring is made. The silicon wafer is mounted on a thin PCB frame to ensure electrical and mechanical contact.

2.2.2   The CsI (Tl) crystals

The second stage of the ΔE-E telescopes of the CHIMERA multi-detector is constituted by a CsI (Tl) crystal, which measures the residual energy of the particles with sufficient energy to punch through the silicon detector. The choice of thallium activated cesium iodide crystals was suggested by various benefit resulting from the known characteristics of this type of scintillator:

- Mass and charge identification of light particles as well as γ-rays thanks to the shape of the produced signal.

- High density (4.51 gr/cm^3), leading to a large stopping power, thus relatively low thickness to stop high energy particles, in comparison with other scintillators with lower density (for example NaI, 3.67 gr/cm^3)

- Relatively low costs

- simple handing and good resistance to radiation damage and to external factors

- Good light emission yield ($\approx 10^4$ photons/MeV), peaked at λ= 550 nm

- Stability of the response, due to the use of photodiodes (HAMAMATSU photodiode (324 mm^2 surface, 300 μm thick)

The crystals have the shape of a truncated pyramid with a trapezoidal base. [29]. The dimensions of the front surfaces is the same of the silicon detectors, while those on the back faces depend on the crystal thickness. The length of the various crystals is suggested by the need to stop the most energetic particles, essentially protons. In order to optimize the light collection , the front surface, where particles hit, is covered with a 2 μm aluminized mylar foil, while the side walls and the rear

face are wrapped in a 150 μm thick Teflon layer, further coated with a foil of aluminum (150 μm thick) to avoid light dispersion. In CHIMERA, to read the light signal, it has been preferred to use photodiodes [30, 31], because these have some advantages on photomultipliers, such as a response spectrum well fitting the CsI (Tl) emission, greater resistance, lower operational voltage value, greater stability and, last but not least, reduced costs. Beyond the advantages mentioned above, some limitations exist: for example, photodiodes have signal to noise ratios not so good as photomultipliers. The photodiodes used have a thickness of 300μm, an active surface of 18x18 mm and are coupled to the crystals by an optical glue.

2.3 The electronic chain

Signals coming from the silicon and from the photodiode are processed by two different electronic chains that suitably transform them for the reading and memorization processed by the acquisition system. Electronic chains are such to satisfy some requirements, as the high dynamical range (from MeV to GeV), a good temporal response, which allows time of flight measurements, low power dissipation under vacuum conditions and a high level of flexibility in coupling the detectors with other electronic devices. In order to minimize noise and signal losses, which would affect heavily the energy resolution, the preamplifiers of silicon detectors and of photodiodes are placed on a motherboard inside the vacuum chamber. The number of preamplifiers found on a motherboard varies depending on which part of the apparatus is considered: in the forward part, i.e. on the firts 9 wheels, where each cell houses two telescopes, there are four preamplifiers on each mother-board (a pair per telescope, one preamplifier for the silicon and the other one for the scintillator). The two telescopes correspond to the internal and the external ring of the same wheel. Instead, in the sphere the motherboard contains only two preamplifiers relative to a single telescope (one silicon and one scintillator). Power supply systems for detectors and preamplifiers, together with the rest of the electronics, are placed outside the vacuum chamber.

2.3.1 The electronic chain for silicon detectors

 Fig. 2.5 shows the diagram of the electronic chain that processes the output signal from the silicon detector. A charge preamplifier is used as the first stage of

the electronic chain. Such device integrates the silicon signal, providing an output height independent of the detector capacity, but proportional to the charge produced and, thus, to the energy of the detected particles. The output is a single negative fast signal, with a decay time of $\approx 200 \, \mu s$ and a rise time of ≈ 50 ns. The PAC sensitivity changes according to the polar angle. In the forward part, where the most energetic particles are expected, the sensitivity is 2 mV/MeV, while in the backward part the sensitivity is 4.5 mV/MeV. In order to be able to check the electronic stability and for calibration operations, a test input is present on the preamplifiers, providing the possibility to send a pulser signal.
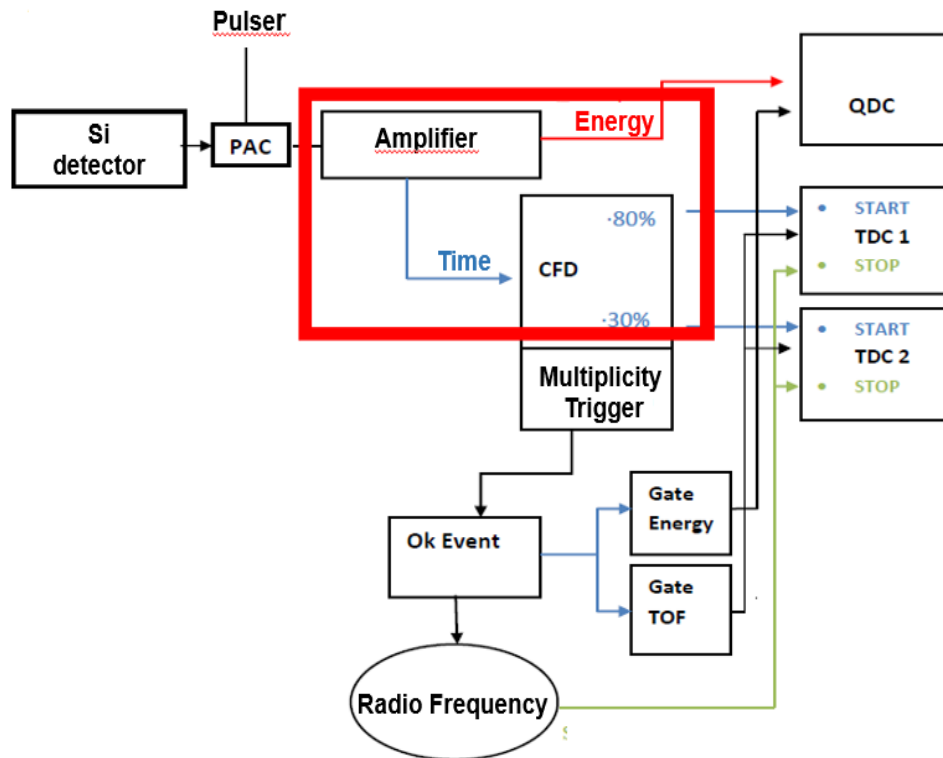

Figure 2.5: Scheme of the electronic chain for Si detectors. In the red rectangle the electronic devices compacted in one module, which allows the application of the pulse-shape technique

The output signal from the preamplifier is processed by the amplifier, a CA-

MAC 16 channels bipolar model or a CAEN module NIM1568B in the case of pulse shape electronics.

In fact, from ring 4 to ring 13, the old CAMAC electronics has been replaced by new compact modules particularly studied to measure the rise time of the silicon signal; in this way it's possible to get the charge of particles stopped in the silicon detectors [32, 33]. In the scheme of Fig. 2.5 all of the electronic components of the new module are inside the red rectangle. Each channel of the CAMAC amplifier produces a negative front bipolar signal (with the positive side cut) as energy output and an unipolar signal as timing output, differentiated to 100 ns and integrated to 20 ns. The working channel can be controlled by using a multiplex output.

The energy signals, with a shaping time of 0.7 μs, are coded by charge digital converters (QDCs), realized on VME 9U standard by CAEN.

Signal conversion is achieved with a low gain or high gain coding, in order to guarantee a good energy resolution, also for low energy particles. When the integrated charge is 1/8 less than the full dynamical range, the conversion takes place thanks to the high gain circuit and the signal is amplified of a factor 8.

The need to carry out precise measurements of time of flight requires the use of a constant fraction discriminator, CFD , processing timing output from the amplifier. The advantage of this use are trigger times signal independent from peak heights, triggering is not on a fixed threshold but on a constant fraction of total peak height.

The CFD, built on a 16-channel CAMAC module, allows to partially eliminate the noise, setting the threshold for the signals coming from the amplifier and provides a logic signal that is used as a START in time of flight measurements. In those measurements the logic called "COMMON STOP" is used: the START signal should consist of the radio frequency signal of the cyclotron, but it is preferable to delay it appropriately, in order to use the signal from as a STOP common to all detectors

For the rings between the external 3 (from the 15th detector) and ring 14, the signals are shaped by PACs and amplifiers, and then processed by two discriminators. The discriminators send logic signals when the input signals overcome respectively the 30% and 80% of the total rise time. These two logic signals, together with the energy signal, are obtained using a CAEN 16 channel Spectroscopy Amplifier NIM1568B. The two logic signals are then sent to two TDCs, that transform into digital information time differences with respect to the

RF/MCP signal used as a common stop: $\Delta T_{30\%} = T_{RF} - T_{30}\%$ and $\Delta T_{80\%} = T_{RF} - T_{80}\%$.

The rise time of the signal is obtained by subtracting these two quantities: $T_{rise} = T_{80}\% - T_{30}\%$. Energy signals are digitized by means of VME QDCs. The gate generation for QDCs, as in the "old" electronic, is performed by a common trigger signal, based on the multiplicity of each reaction event.
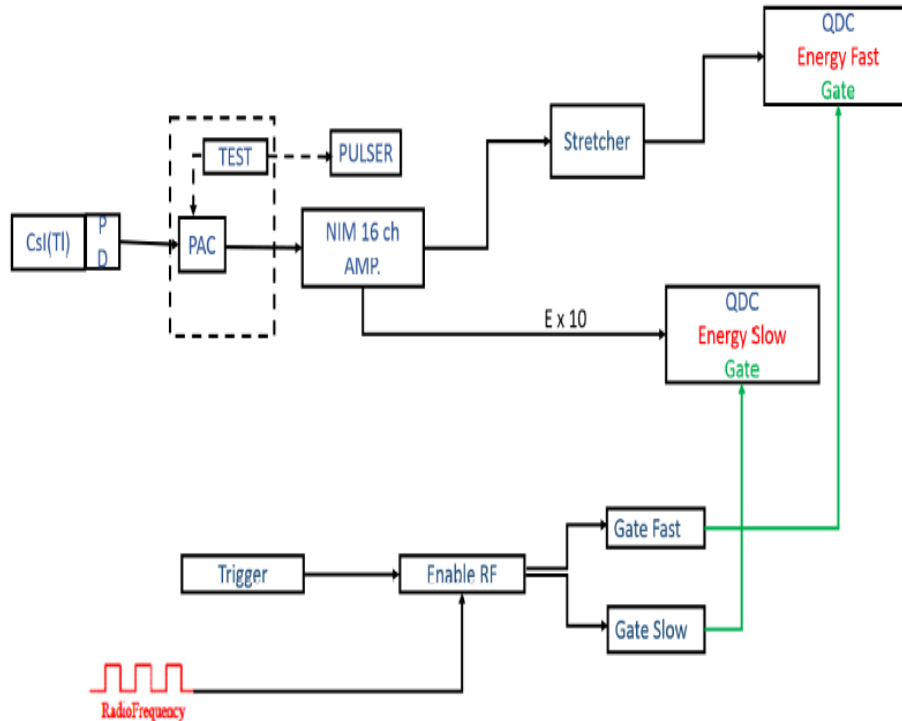
Electronic chain for CsI(Tl) scintillators

Figure 2.6: Scheme of the electronic chainfor CsI(Tl) scintillators

The photodiodes coupled to the CsI(Tl) scintillators are silicon detectors, as a consequence the electronic chain (Fig. 2.6) is not so different from the one used for the silicon detectors, the difference are due to the different behavior of the

CsI(Tl) crystals and to the need of processing of the fast and slow components of the signal. Charge preamplifiers provide the photodiode signal readout. The maximum capacitors required are the order of some hundred pF because these charge preamplifiers have a sensitivity of 50-100 mV/MeV. The output signals have rise-time, longer than 50 ns and that can reach values of the order of μs. The output preamplifier signals are amplified and shaped, by means of a unipolar amplifier, by using typically a shaping time of 2 μs, but it is possible to use different shaping time (0.5, 1, 2, 3 μs).

These amplifier, designed by INFN Sezione di Milano and produced by SILENA, in 16 channels NIM module, have a double output in energy, for each channel, with different gains. The higher signals is 10 times of the lower signals. For the integration of the slow component, the higher signals are sent to the QDCs, in order to be digitized and acquired. While the lower signals are sent to a stretcher and then to the QDCs for the integration of the fast component. The stretched signals lead to a presence of a level, with the same amplitude of the peak, lasting for $\approx 10\,\mu$s, time determined from a gate signal.

Two synchronous gates are sent to the two QDCs. The used gate signals start a few μs later than the time of peak. It is possible to apply the pulse shape discrimination, in order to identify in charge and mass light charged particles as well as γ-rays, by correlating the output signals of the two QDCs. In fact one output will correspond to the charge of the stretched fast signals and the other to the charge integral of the tail of the signal, which is mainly dominated by the slow component. Then, a Data Acquisition System ([34, 39]) that allows a fast overview of growing physical results, is needed in order to collect and store data coming from both Silicon and CsI(Tl) electronic chains.

2.4 Identification techniques

In CHIMERA four different techniques [25, 24] are used to measure energy and speed of the detected particles and to identify them in charge and /or mass. These techniques are:

- ΔE-E technique: uses the signal related to the energy loss in the silicon detector and the signal from the CsI (Tl) related to the residual energy of the particle punching through the silicon detector and which stops in the scintillator. It allows to identify in charge the particles punching through

the first stage of the telescope and for ions with Z <10, it also allows mass identification.

- Signal discrimination technique in the CsI (Tl): called Pulse Shape Discrimination, PSD, allows identification in charge, for most energetic light particles up to Z = 5 and also a good isotopic identification for particles with $Z \leq 4$. The method uses the fast and slow components of the signal in the crystals.

- Time of Flight technique: uses the Si energy signals and the time of flight provided by the Si (start) and the reference time signals provided by the radio frequency coming from the CS (stop). This method allows to perform velocity measurements fro all the particles and it can give information on the mass of nuclei stopped in Si detectors.

- Pulse shape discrimination in Si detectors, this method is based on the analysis of the rise time of Si signals, and it can give information in order to identity in charge the particles and ions stopped in the Si detectors.

2.4.1   ΔE-E method

This technique is based on the formula of Bethe and Bloch [40] which expresses the specific energy loss dE of a charged particle punching through a material of thickness dx:

$$\frac{dE}{dx} \propto \frac{AZ^2}{E} \tag{2.1}$$

Thus, for a fixed thickness dx, the energy loss dE of a particle depends directly from its charge Z and its mass A and is inversely proportional to its energy E. In CHIMERA the energy loss signal ΔE comes from the silicon QDC and the signal relative to the residual energy released by the particle in the second stage, is the fast component of the signal outcoming from the scintillator. Reporting ΔE as a function of the residual energy or of the total energy (the sum of the energy lost plus the residual energy), a family of curves of the type 1 / E are obtained as a function of charge and mass as shown in Fig. 2.7. Since the dependence on Z is quadratic, there is a good separation of the various lines which represent the different charges and, therefore, an excellent identification in Z is possible. The dependence on A is not so strong, because it is just linear, but for the light fragments produced, a good isotopic identification is obtained.
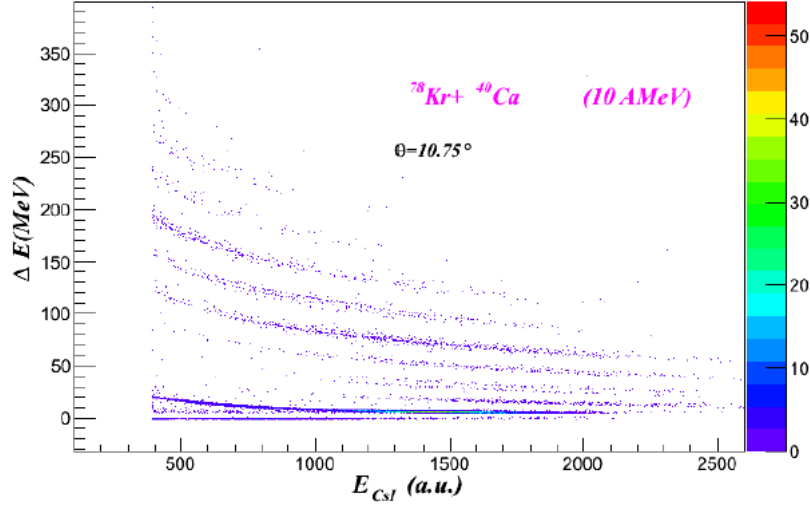
Figure 2.7: ΔE-E bidimensional plot in the reaction $^{78}Kr + ^{40}Ca$ at 10 AMeV, for a detector place at θ_{lab}=10.75°

2.4.2 Pulse shape analysis method for scintillators

The scintillators are widely used for the identification of light particles because emit light signals whose shape varies with the type of incident radiation. The light emitted by the CsI (Tl), after the excitation by the incident particle, presents two components commonly known as *fast* and *slow*, and thus can be expressed as the combination of two exponential components with different time constants:

$$L(t) = L_1 exp^{-\frac{t}{\tau_1}} + L_2 exp^{-\frac{t}{\tau_2}}, \qquad (2.2)$$

where L(t) is the amplitude of the light signal at time t, and L_1 and L_2 are the amplitudes of the fast and slow components of light, while τ_1 and τ_2 are the decay time constants of the two components. These decay times depend on the detected particles. The relationship between the intensities of the two components depends on the specific density of dE / dx ionization and this is the characteristic used in the pulse shape analysis [29]. In fact, if the two components of the light are separated, particles are discriminated with different intensities ratios and it is thus possible to extract the charge and mass of the incident particle. Among the various possible techniques for performing the pulse shape analysis of the signal, it has been chosen for CHIMERA the two- gates method 2.8. This method applied to
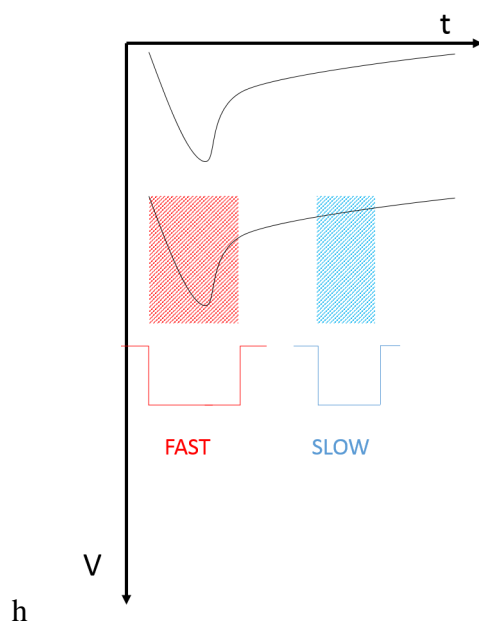
Figure 2.8: Scheme of treatment of Fast and Slow components using the two gate method.
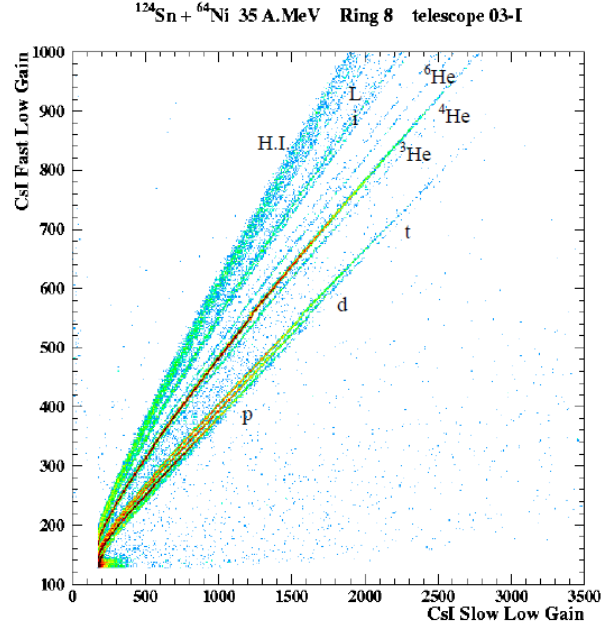
Figure 2.9: $Fast - Slow$ identification scatter plot obtained for one crystal, located at θ= 13.75 ° of the CHIMERA array, in the reaction $^{124}Sn+^{64}$Ni at 35 AMeV

a photodiode [41] is based on the fact that the decay time of the amplifier signal, under proper shaping time conditions, keeps memory of the mass and charge of the detected particles.

This technique consists in processing the two signal components with two QDCs, with different windows of integration in time, since the information on the two components is transported in two different parts of the signal, as shown in 2.8.

In fact, when the signal reaches the amplifier, the information on the fast component remains almost unchanged, while the slow component, characterized by longer times for the signal formation in the amplifier, influences strongly the signal tail, as schematically shown in Fig. 2.8. By means of two gate methods, it is possible to obtain two signals, proportional to the fast and the slow component, produced by the CsI(Tl) amplifier.

The identification plot is obtained by plotting the fast component against the slow component, an example of this identification plot is shown in Fig. 2.1 .

2.4.3 Time of flight technique

The direct measurement of the velocity through the TOF technique is one of the most peculiar characteristic which make the CHIMERA multidetector a unique tool in the study of heavy ion collisions [42]. In addition, the combination of ΔE and TOF measurement (ΔE-TOF technique) allows to identify in mass the fragments stopped in the silicon detector [25, 24, 43]. This identification method and the pulse shape discrimination in silicon technique were fundamental in the realization of the ISODEC experiment. In fact, CHIMERA was designed for the study of heavy ion collisions in the intermediate energy domain and for the first time, in the ISODEC experiment, its use was extended to the study of reaction realized at low energies. In this experiment, because of the low energy, the most of the particles are stopped in the silicon detector and their identification can be made through these two techniques. The pulse shape allows the identification, charge by charge, for reaction products with a value of the atomic number less then 18, instead the time of flight allows the identification of reaction products in a range of masses from those of light IMF to the Evaporation Residues. A procedure in the calculation of the mass, well described in the following, was expressly developed for the analysis of the ISODEC experiment. The measurement of the time of flight in CHIMERA is performed by measuring the difference between the delayed signal of the radio frequency of the cyclotron and the logic signal in exit from the CDF, acting on a given detector, with a fraction set at 30% of the signal height. This difference is converted into channels t_{ch} by a TDC. The calibration curve of the TDC, i.e. the channel / ns correspondence will therefore be a line:

$$t(ns) = \alpha(t_0 - t_{ch}). \tag{2.3}$$

t takes into account not only the real time of flight that the particle takes to get from the target to the detector, but also delays due to cables, to the phase of the cyclotron and the delay in the formation of the signal in the silicon detector. All these effects are included in the time constant t_0, in channels units, depending on the specific detector and its electronics. This constant must be accurately determined together with the conversion factor α (ns/ch) from channels to nanoseconds, which is typically about 250 ps/channel. Before describing the techniques used for the definition of t, it is necessary to distinguish two types of particles:

1. Particles, not having sufficient energy to punch through the silicon detector, lose all their energy and are stopped in this stage of the telescope. By using

the TOF technique, are identified in mass with the non relativistic relationship, which relates energy to the time of flight:

$$E = \frac{1}{2}A\frac{d^2}{t^2},$$ (2.4)

where d is the distance of flight. The energy as a function of time results in $\frac{1}{T^2}$ curves.

2. The particles which punch through the silicon detector, have energy loss ΔE which linearly depend on Z and inversely on the velocity, and thus given by:

$$\Delta E \propto \frac{Z^2 \cdot t^2}{d^2}dx$$ (2.5)

Plotting ΔE as a function of time, it is possible to get curves that have the trend of the type t^2. Fig. 2.10, shows a bidimensional plot ΔE - TOF, in which two zones A and B can be distinguished. Zone A is occupied by particles which stop in silicon, while the curves of zone B are those related to particles punching through the silicon. The two zones are separated by the line passing through the so-called *punching through* points, corresponding to the silicon crossing areas. In the procedure for the determination of t_0 the first step is to find its possible dependence on energy and particle mass.

Remembering the classic expression of energy we have:

$$E = \frac{1}{2}Mv^2 = A\frac{D^2}{2\alpha^2}\frac{1}{(t_0 - t_{ch})^2}$$ (2.6)

where M is the mass of the particle and D is the distance of flight.
Fig. 2.11 shows three loci of the points of the plane corresponding to the detected particles with mass number A = 7, A = 11 and A = 15. By using the previous formula and assuming a linear response with respect to energy for each detector, independent of the mass and the charge of the particle, the dependence of t_0 on the energy has been found for each of the three masses considered .
Actually the independence of t_0 on mass and energy, which is expected in ideal conditions, is obtained only for the particles punching through the silicon detector. That's the reason why the t_0 used in that region is called t_0^{sat}, i.e. saturated. Probable reason is that for particles punching thorough the Silicon detector, the specific ionization is small (no Bragg peak) and the plasma delay effects are negligible;
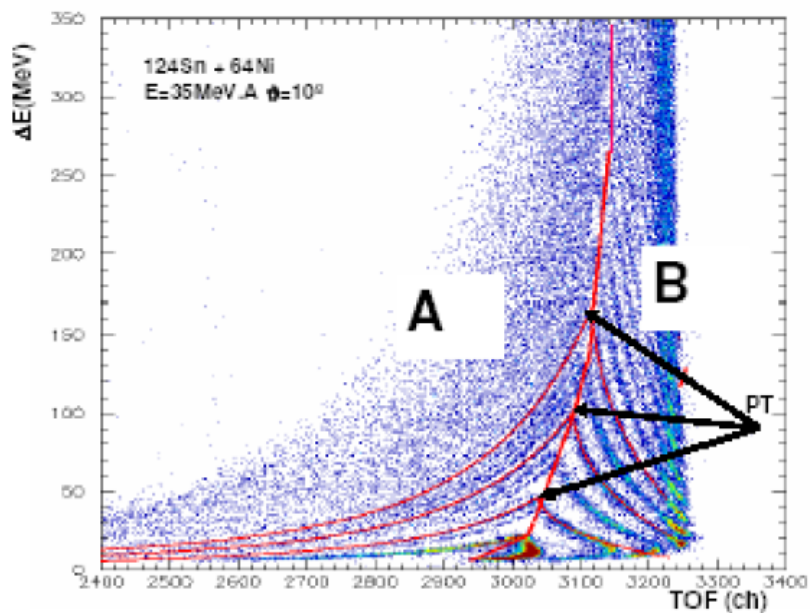
Figure 2.10: ΔE- Tof matrix for a detector placed at $\theta = 10\,^\circ$, in the reaction ^{124}Sn+ ^{64}Ni at 35 AMeV
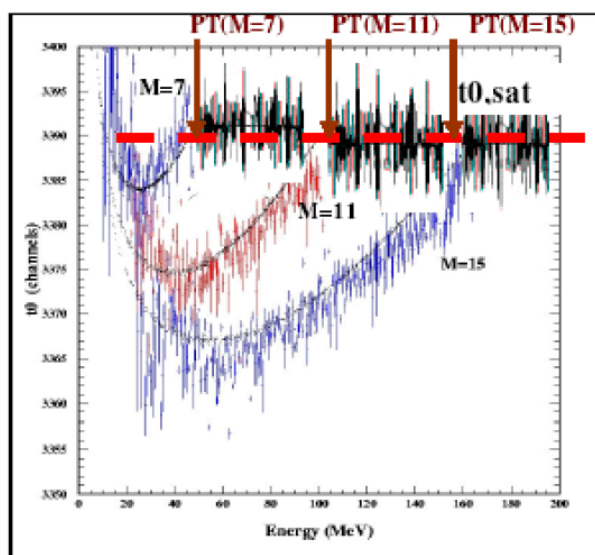

Figure 2.11: The t_0 parameter vs particle kinetic energy

moreover, signals are large enough to be not affected by CFD walk effects, taking place for small signals. The t_0^{sat} in Fig. 2.11 is highlighted by a red dashed line: it is calculated using a fit procedure. For each point lying on a curve corresponding to a Z value (recalling here that each particle passing through the silicon detector has been identified in charge by the ΔE-E technique) in zone B, t_0 is calculated for each telescope, with the formula:

$$t_0^{sat} = t_{ns} + 0.717 \frac{d}{\sqrt{\frac{E}{A}}} \tag{2.7}$$

with d distance of flight, E the energy and A are respectively the mass of the particle.
The mass are calculated by using Charity formula : $A = 2.08 \cdot Z + 0.0029 \cdot Z^2$,.
The distribution of t_0 obtained, is fitted with a Gaussian function and the value of the peak is the value of t_0. Since this value is practically independent of the charge, the operation is carried out for several Z, in order to assume the average value as t_0 at saturation.
There is a certain discrepancy between the value of t_0 of saturation and the value of t_0 for particles which stop in silicon. Thus it is not possible to use t_0 of saturation in the calculation of the time of flight for these particles, because this would lead to wrong calculation of the average value of the mass. The non saturated t_0 is obtained by fitting the experimental data with the semiempirical formula:

$$t_0(A, Z, E)_{i+1} = t_0^{sat} + (S - R(A_i, Z_i, E_i)) \cdot \left| p_0 \sqrt{\frac{A_i}{E - E_0}} - p_1 (1 - exp^{\frac{A_i}{p_2}}) \right| \tag{2.8}$$

with S is detector thickness, R particle range in silicon, E_0 is the energy offset linked to the detection threshold, p_0, p_1 and p_2 are free parameters related to the characteristics of the detector.
In order to determine the value of t_0 an iterative method can be used; it is possible to get the value of the mass from the formula:

$$A_i = \frac{2E[\alpha(t_{0-i} - t)^2]}{d^2} \tag{2.9}$$

The starting point of the used procedure is to insert the value of t_0^{sat} in 2.9, in order to obtain the start mass to put in 2.8. The obtained value of t_0 is then reintroduced into the formula and the procedure is repeated until a convergence is

reached ($A_{i+1} - A1 < 0.5$).

A phenomenological linear dependence of the parameter p_1 on the mass is found. Thus for each telescope the value of p_1 is extrapolated from the straight line passing though the points $P_{min}(p_{min}, A_{min})$ and $P_{proj}(p_{proj}, A_{proj})$. Where A_{min} is the most probable mass corresponding to the minimum charge attributed by the pulse shape technique and p_{min} is the value of p_1 parameter that, introduced in 2.9 and by using the procedure previously described, lead to a value of the mass compatible with A_{min}. While p_{proj} is the value of this parameter for which the mass of the projectile A_{proj} is well reproduced.

2.4.4 Pulse shape analysis for silicon detectors

The integration of PSA, technique of identification is fundamental for the realization of the ISODEC experiment, because this technique allow the charge identification of the fragments stopped in the silicon detector and as seen in the previous subsection is used for the calculation of the p_1 parameter in 2.8 At low energies, in fact, most of the reaction products stops in the first stage of the telescope and can be identified in charge just thanks to the PSA, thus lowering the simultaneous mass and charge identification threshold. This identification technique uses the sensitivity of the silicon pulse shape to the depth of density of ionization track and therefore from the mass, charge and energy of the detected particle. This is essentially due to two effects:

1. The drift times of the charge carriers along the ionization track.

2. The formation and erosion of the "plasma column", a high conductance zone, produced by the high density of charge carriers along the ionization track, which expands radially, due to diffusion of charge carriers .

Generally the plasma formation process is very fast and has a duration of the order of some ps, which is negligible compared to the transit times and the erosion time of such plasma. These last two effects are responsible for the time of charge collection. The rise time of the signal is given by the combination of the erosion time and the transit time. The erosion time τ_{plasma} is defined as the time required to erode the plasma column around the ionizing track until all the electron-hole pairs created are under the action of the electric field; in fact, a dense cloud of charges around the ionizing track screens the most internal charges from the electric field, and this leads to a delay in the generation of the signal with respect to

the moment of impact of the particle. The τ_{plasma} depends on the initial density and the radius of the plasma zone, on the diffusion constant for charge carriers and on the internal electric field strength, it can be expressed as function of mass, charge and energy of the incident particle [46]:

$$\tau_{plasma} \sim a\sqrt{MZ^2} \cdot \sqrt{B(\frac{1}{E}ln\frac{4m_eE}{Ml}F)} \tag{2.10}$$

where a is a normalization constant, M, Z and E are the mass, the charge and energy of the incident particle, respectively, m_e is the mass of the electron, B is the Bethe-Block constant, I is the average ionization energy for the absorbing material (silicon in this case) and F is the applied reverse bias. The carriers transit time depends on the collection speed of holes and electrons and is given by the following expression:

$$\tau_{transit} \sim \frac{S - \frac{R}{2}}{v} \tag{2.11}$$

where S is the thickness of the silicon detector and R is the range of the particle in silicon and v the constant velocity of carrier electrons.
Both effects are responsible for finite charge-collection time. In particular, if fast high band width charge-sensitive preamplifiers are used [44], the total charge-collection time is reflected by the rise time of output signal, and consequently rise-time discrimination may be used as a method for particle identification [46, 47].
PSD, usually is applied for particles impinging on the rear side of the ohmic contact, in which the electric field is lower (*reverse configuration*). This technique is used for the first time with large detectors, as in CHIMERA case, in *direct configuration*(the particles impinge on the front-side of the detector) Fig. 2.12, in order to avoid to compromise time of flight measurements [58]. Considering, for each silicon, the energy as a function of the rise time, the family of curves allowing identification in Z is obtained as shown for the reaction $^{78}Kr + ^{40}Ca$ in Fig. 2.13 .

In our experiment, the pulse shape allows the identification in charge of particles from Z = 2 up to Z = 18, with an energy threshold of about 4.5 AMeV.
The pulse shape analysis was performed using the Psdfit program, developed by J. Han [48]. This program is based on a semiautomatic procedure in which a fit is performed, for each telescope, on the lines corresponding to the various Z values in the energy – rise time bidimensional plot, as in the example of Fig. 2.14. First,
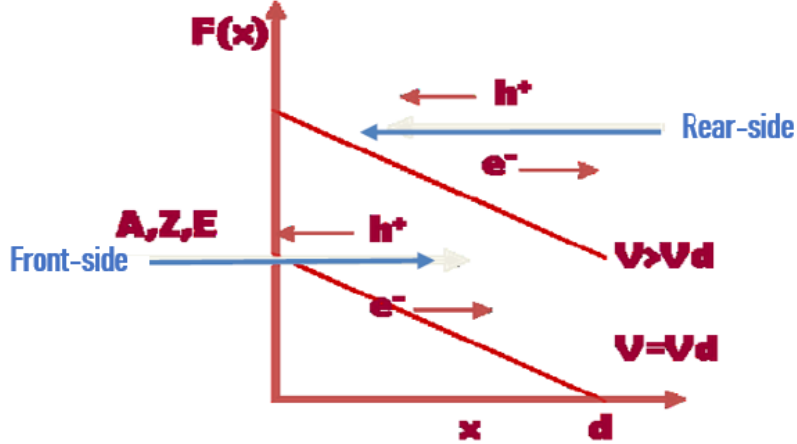
Figure 2.12: Scheme of the electric field F(X) as function of the depth of the track

some reference points, the so-called "clicks" (asterisks in Fig. 2.14), are placed on the lines for the charge identification, then a graphic outline called "cut" (red line dashed) is applied around the area where events are well identified. At this point it is possible to fit the lines. The formula used for the fit is a parametrization, taking into account the drift motion of the electrons and holes within the silicon detector, under the effect of the present electric field and has the following expression:

$$t_{RT} = par[1] \cdot Z \cdot exp(\frac{-E^I}{3.75}) \cdot \frac{1}{-x + d_1} + par[2] \cdot ln|\frac{d_1}{-x + d_1}| + par[3] \cdot ln|\frac{d_2}{-x + d_1}| + par[4]$$
(2.12)

where d is detector thickness, Z is the particle charge and E^I its energy, x is the particle range, d_1 is given by $d_1 = \frac{d}{2} \cdot (par[0] + 1)$, $d_2 = \frac{d}{2} \cdot (par[0] - 1)$ and par[0], par [1], par [2], par [3] and par [4] are 5 free parameters. Once the Z lines are drawn, the analysis program assigns the charge to each particle detected, on the base of the proximity of the experimental point with a line. Events are labeled with different codes, depending on whether they are well or bad identified.
The program is able to carry out, through extrapolation, identification also for those particles on whose lines the clicks have not been applied.
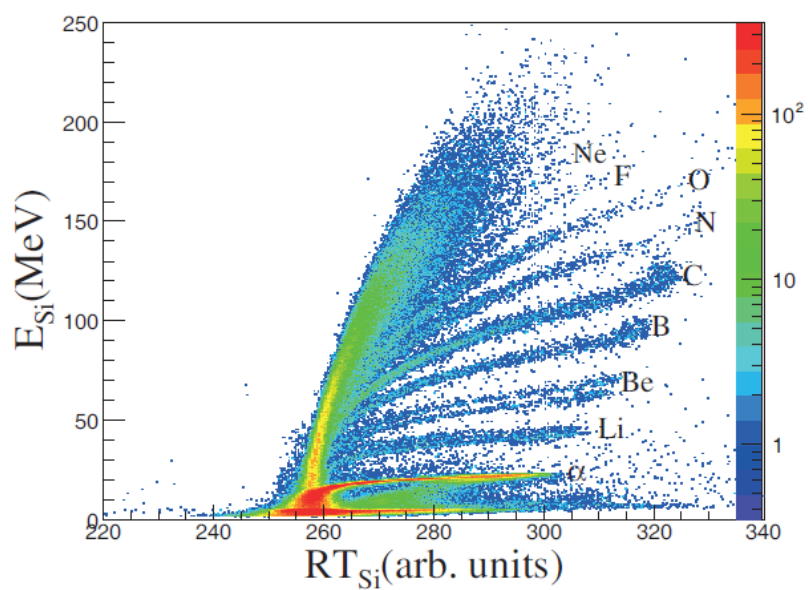
Figure 2.13: Energy-RiseTime plot of particle detected in Silicon detector for the reaction $^{78}Kr + {}^{40}Ca$ at $\theta = 34°$
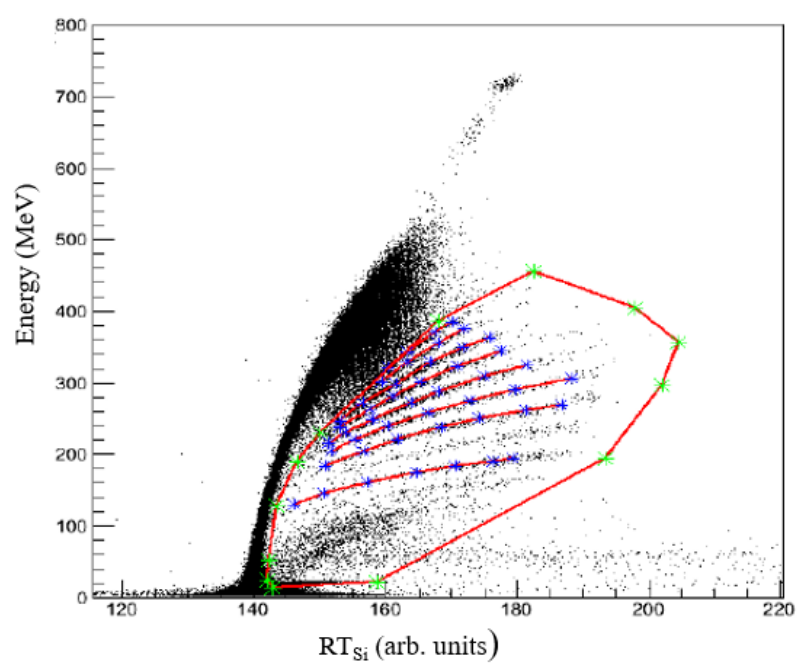
Figure 2.14: Example of fit for the charge attribution with the semiautomatic procedure, in the pulse shape analysis (see text for details)

Chapter 3

Experimental Results

The main goal of this thesis work, as already mentioned, is to put on evidence the isospin influence on the mechanisms involved in the reactions $^{78}Kr +^{40}Ca$ and $^{86}Kr +^{48}Ca$ at 10 AMeV. In fact, it has already been shown that at higher energy the N/Z ratio of the entrance channel drives the reaction dynamics of central collisions [49] and peripheral collisions with the neutron enrichment strongly influencing the competition between the dynamical and statistical break-up of the projectile [50, 51].

For a first general idea of the reaction mechanisms one can look at the mass distributions of the reaction products measured at different angles, shown in Fig. 3.1 for the neutron poor system. One can recognize the contribution of the various processes which populate different zones of the region of masses in a different range of angles. The fusion evaporation channel, with mass centered around A = 100 is mainly present at the very forward angles, while the contribution of the symmetric fusion- fission channel, with a wide maximum in the region A = 40–80, is distributed over a broader angular range. It is possible to distinguish a third component, more focused at forward angle and strongly centered around A = 80, which can be attributed to a kind of binary mechanism, not completely relaxed in mass distribution, as it is in the Deep Inelastic Collisions (DICs). For this latter mechanism, a peak at A = 40 is expected, but because of the energy threshold and of the geometrical acceptance of the device, this is not observed.

It should be noted that the rough data displayed in the Fig. 3.1 were not corrected for the solid angles of the detectors in the various rings of the CHIMERA apparatus.
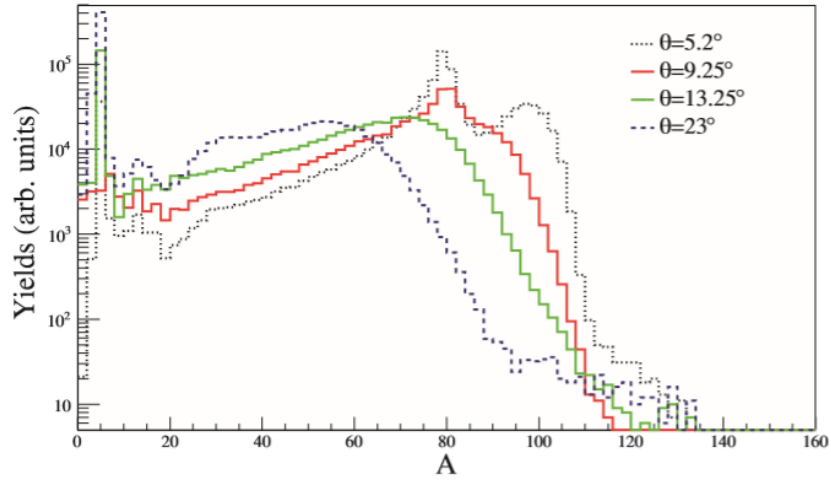
Figure 3.1: Mass distributions of reaction products for the n-poor system at different laboratory angles. The plotted relative differential cross sections were not corrected for solid angles (see text for details).

The contribution of Deep Inelastic Collisions can usually be disentangled by analyzing the correlation between the total kinetic energy (TKE) of the binary system and the emission angle of the fragments in the center of mass frame, $\theta_{c.m.}$. The Total Kinetic Energy of the system is reconstructed from the kinematic characteristics of the heavier fragment, applying energy and momentum conservation. TKE is thus reported as a function of the center of mass emission angle in this sort of Wilczynski plot [13], displayed for the reaction $^{78}Kr + {}^{40}Ca$ in Fig. 3.2. It is clearly possible to discriminate between a less dissipative mechanism that can be attributed to dynamic processes, focused at small angles and concentrated in the region with Total Kinetic Energy greater than 100 MeV, and a more relaxed process giving a constant value of energy of about 85 MeV for any value of the emission angle. In fact, as mentioned previously in the part relative to the deep inelastic collisions in chapter 1, the yields for the quasi-elastic products are concentrated around the grazing angle. A similar result is obtained for the neutron rich system with a DICs contribution even larger than in the neutron poor one. Considering heavier fragments we can calculate the total kinetic energy (TKE) for symmetric fission. The value of TKE = 83.6 MeV obtained for Z = 28 is consistent with the value 84.6 MeV of TKE calculated for the ^{118}Ba fissioning

nucleus. For the neutron rich system which leads to the formation of ^{134}Ba we have obtained similar results. In this case we measured a value of TKE = 76.7 MeV, which is comparable with the calculated value of 79.5 MeV [52]. In both systems, the contribution of rotational term is estimated 15–20% of the total excitation energy [21]. In the following we will present the results obtained in our
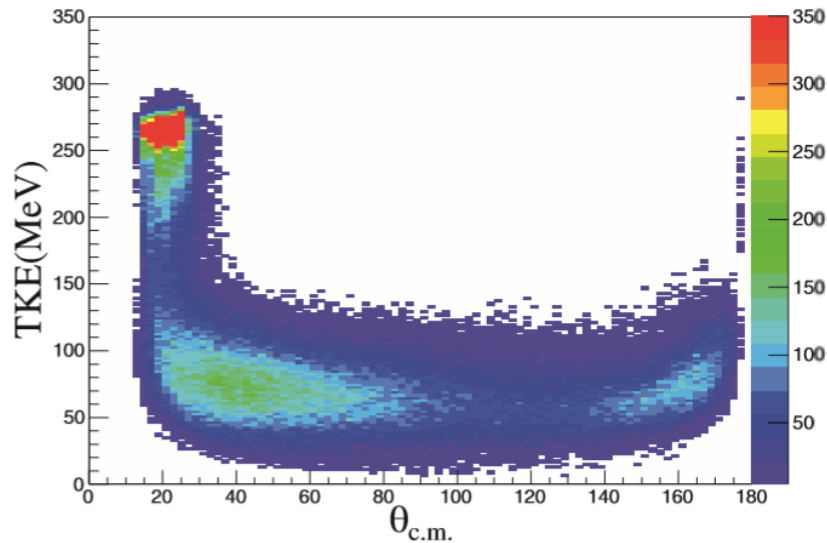

Figure 3.2: Wilczynski plot. Total Kinetic Energy is displayed for the reaction $^{78}Kr +^{40}Ca$ as function of the emission angle of the fragments in the center of mass frame, $\theta_{c.m.}$

analysis. The chapter is divided into three sections. In the first section the Kinematic characteristics, the angular distributions and the cross sections are discussed for the capture reactions. In the second section, the selection method developed in order to discriminate the PLF break up from the other reaction mechanisms and the obtained results after this selection are presented. Finally in the third section, for the capture reactions, the comparison with the theoretical prediction of HIPSE followed by the the statistical code GEMINI++, GEMINI++ and the DNS model is shown.

3.1 Fusion Evaporation and Fission-Like processes

3.1.1 $LAB \longrightarrow C.M.$ reference frame transformation

Quantitative analysis of the kinematic features require to define them in a convenient reference frame. In general, energy and velocity spectra and the angular distribution, measured in the fixed reference frame of the laboratory, must be transformed to the frame of the center-of-mass, for a better understanding of the processes and a comparison with predictions of the theoretical models.

Fig. 3.3 illustrates the transformation from reference frame of the laboratory to
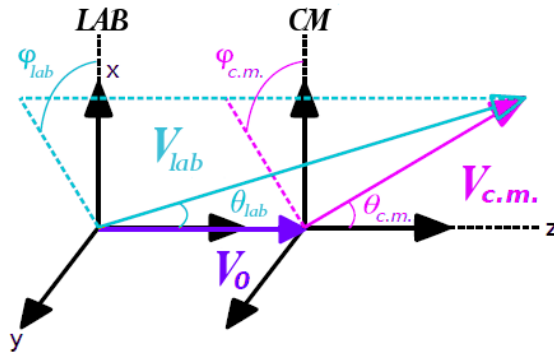

Figure 3.3: Scheme illustrating the transformation from reference frame of the laboratory to the frame of the center-of-mass

the center-of-mass frame. The center-of-mass frame moves along the direction and with the speed, given by the velocity vector $\vec{v}_0$. Thus a particle having a velocity $\vec{v}_{lab}$ in the frame of the laboratory, will have in the center of mass frame a velocity $\vec{v}_{c.m.}$; the transformation from a frame to the other will be defined by the vector equation [53]:

$$\vec{v_{lab}} = \vec{v_{c.m.}} + \vec{v_0} \tag{3.1}$$

Another quantity which is most conveniently analyzed in the center of mass frame is the differential cross section. This quantity is proportional to the probability of a scattering event, in which the particle is detected with an energy between E and $E+dE$ and at a solid angle between Ω and $\Omega + d\Omega$. In the laboratory frame the double differential cross section corresponds to:

$$\frac{d^2\sigma}{dE_{lab}d\Omega_{lab}} \simeq \frac{N_{lab,i}}{N_0\Delta\Omega_{lab}\Delta E_{lab}} \tag{3.2}$$

where the number of counts $N_{lab,i}$ in channel i are normalized to the number of scattering events N_0, to the solid angle $\Delta\Omega_{lab}$ and to the energy bin of each channel ΔE_{lab}, similarly in the center of mass reference frame.

The transformations from one reference frame to another require the conservation of the flux. The laboratory frame distributions are distorted by a transformation Jacobian that arises because the solid angle viewed by the detector in the laboratory frame is different from that in the center of mass frame. The differential cross sections in two frames are related by:

$$\frac{d^2\sigma}{dE_{c.m.}d\Omega_{c.m.}} = \frac{d^2\sigma}{dE_{lab}d\Omega_{lab}}|J| \tag{3.3}$$

Where |J| is the Jacobian (for details about the Jacobian look at [54, 55]) and has the following expression:

$$J = \frac{v_{c.m.}}{v_{lab}}\left(1 - \frac{v_0}{v_{lab}}cos\theta_{lab}\right) \tag{3.4}$$

3.1.2   Energy spectra and velocities in the center of mass frame

The study of the kinematic characteristic of the reaction products provides fundamental information on their production mechanism.

In Fig. 3.4(a) and Fig. 3.4(b) are shown representative examples of fragment energy spectra, in the center of mass system, measured at the laboratory angle $\theta = 10.75°$, for fragments with Z = 3,4,5 and for fragments with Z = 12 ,14,16, respectively. For the reference frame transformation full moment transfer has been assumed. The mean energies of the spectra are Coulomb-like and increase with the charge of the emitted nucleus. It is observed that the spectra evolve from a Maxwellian shape for lighter fragments, towards a more symmetric Gaussian-like shape for the heaviest nuclei. A model [56, 57], in which the decay of fully equilibrated system is assumed, well describes this evolution of the kinetic energy distribution as a function of the fragment size. These center of mass energy spectra for Z from 3 to 16, are centered at the same energy value quite independently of

the angle, which is a signature of highly relaxed production mechanism [58, 59], as confirmed by the velocity spectra analysis.
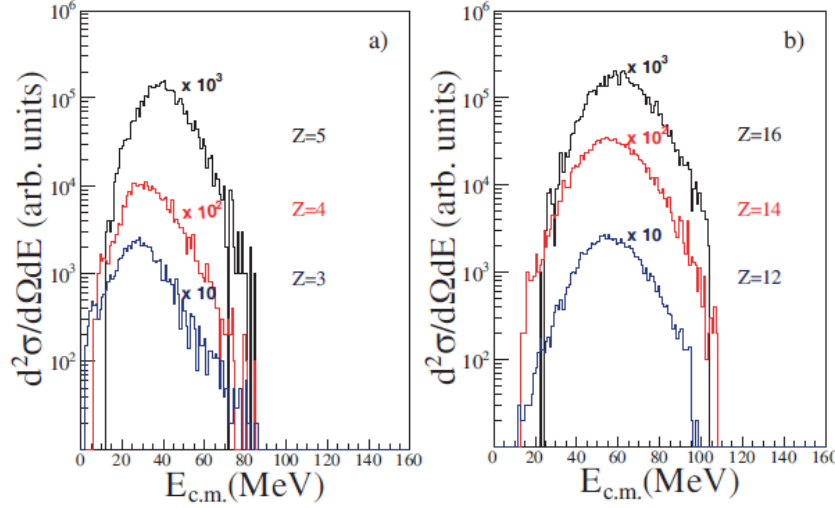

Figure 3.4: Center of mass energy spectra of lighter fragments (a) and heavier fragments (b), produced in the reaction $^{78}Kr +^{40} Ca$ at $\theta_{lab} = 10.75°$

Using the ToF technique, we were able to measure the velocity spectra of the emitted fragments, providing precise measurements of the average velocity $v_{c.m.}$ in the center of mass system. These results are plotted in Fig. 3.5 as a function of Z, at $\theta_{lab} = 5.2°, 10.75°$ and $21°$, for the neutron poor system. We note that, for a given Z, the $v_{c.m.}$ is constant within the experimental uncertainty with respect to the emission laboratory angle. This behavior supports the idea that the emission of these fragments follows the equilibration of a composite system. In other words, it indicates that a high degree of relaxation of the relative kinetic energy has been reached before the decay of the excited nuclear system started. The approximately linear decreasing trend of the $v_{c.m.}$ by increasing the Z of the emitted fragments, suggests a binary process, dominated by the Coulomb interaction between the fragment and its complement [60, 58, 59]. Moreover, the mean values of the velocity, at laboratory angles, are well reproduced by the theoretical predictions (solid line in the figure) of the Viola systematics with the corrections by Hinde [66] for the asymmetric fission, providing the most probable energy released in a statistical fission process [61]. This regular behavior is slightly modified for

heavy residues (Z>30) at more forward angles, probably due to the occurrence of components attributable to a contribution of dynamic process in their production.
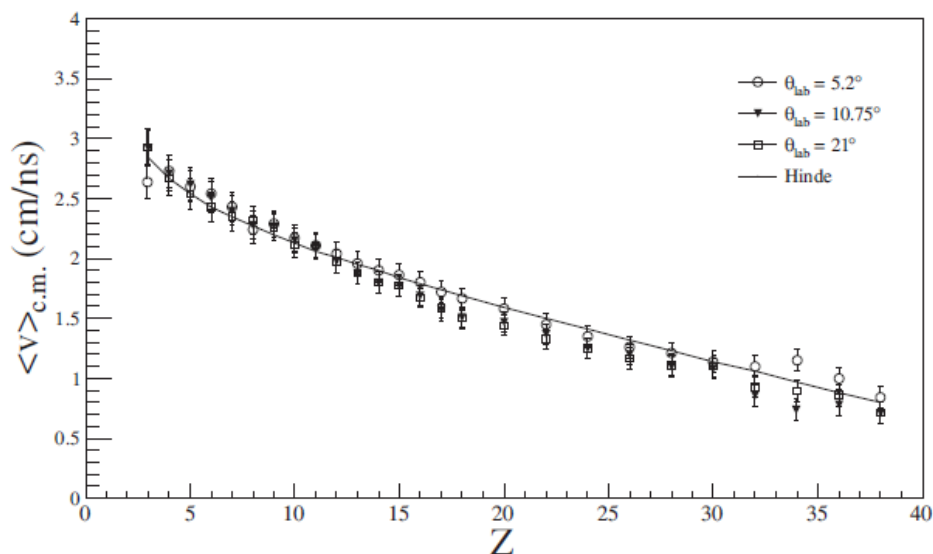

Figure 3.5: Average value of the velocity in the center of mass reference frame at different detection angles as a function of atomic number of the emitted fragments for the reaction $^{78}Kr + ^{40}Ca$. The line represents the Viola-Hinde prediction (see text for detail).

3.1.3 Elastic diffusion and normalization conditions

The normalization parameter for the calculation of the cross sections is extracted from the elastic scattering. In fact, because of the impossibility of good accuracy in the beam current measurements, we decided to use a normalization procedure with respect to the elastic scattering. In order to select the best angle for the normalization, we calculated the grazing angle and we studied the distribution of the elastic diffusion, as detailed below.

Accurate determination of detection angles and beam axis are the experimental conditions required for the precise measurement of the elastic scattering angular distribution. In these measurements care have to be taken in order to limit the counting rate to avoid the damage of the detectors and to limit the dead time of

the acquisition system. For these reasons, the CHIMERA silicon detectors located at the polar angle $\theta_{lab} = 1.4°$, $2.1°$, $3.1°$ and $4.1°$ were covered with a shield in which centered circular holes of 0.5 cm radius were made; this reduced the acceptance of the detector to 4% of its active surface. Thanks to the azimuthal symmetry of the apparatus, the beam axis was accurately determined by counting the elastically scattered particles clearly separated from all other events. In fact, during the experiment different detectors of the same ring of CHIMERA and thus, theoretically, at the same polar angle, have measured a different number of elastic events, showing a dependence of those on the azimuthal angle. This behavior, observed in all the rings and also for other kind of events, is due to a shift of the beam axis with respect to the center of the wheels, where the detectors are arranged. We have determined the angular shift $\Delta\theta$ by using the cross sections $\sigma(\theta - \Delta\theta)$ and $\sigma(\theta + \Delta\theta)$ calculated by the *LISE++* software [63], with θ polar angle, covered by one ring of CHIMERA. The value obtained, $\Delta\theta \simeq 0.13°$, is the one for which $\sigma(\theta - \Delta\theta)/\sigma(\theta + \Delta\theta)$, reproduces the ratio $\frac{N_{max}}{N_{min}}$, where N_{max} and N_{min} are, respectively, the maximum and the minimum number of counts of the elastically scattered particles experimentally observed in the same ring. In particular we performed these calculations for the first rings, those that cover the polar angles $\theta_{lab} = 1.4°$, $2.1°$, $3.1°$ and $4.1°$. In fact, in the other rings the too big angular opening affects the $\frac{N_{max}}{N_{min}}$ and thus for these rings we have geometrically extrapolated the angular shift by assuming the same shift respect to the target as calculated for the most forward rings.

The absolute normalization was derived by comparing the experimental elastic scattering to the Rutherford scattering cross section at very forward angles. The elastic scattering angular distribution was measured in the angular range $1.4° < \theta_{lab} < 9.2°$ in steps of about $1°$, for both reactions. Fig. 3.6 reports, as a function of the laboratory angle, for the two studied reactions, the ratios $\sigma_{el}/\sigma_{Ruth}$ of the elastic and Rutherford cross sections, normalized to the unity in the flat region of the curves; error bars are smaller than the markers. These ratios present the expected angular behavior for this kind of reaction partner at such a bombarding energy. In particular, the extracted quarter point angles (qp), for which $\sigma_{el}/\sigma_{Ruth} = 1/4$ [64], $\theta_{qp}\ n-rich = 7.6°$ and $\theta_{qp}n-poor = 8.6°$, are in agreement with the results of a calculation using a semi-classic (sc) formula, $\theta_{sc}\ n-rich = 6.8°$ and $\theta_{sc}\ n-poor = 8.0°$. θ_{sc} is determined in the context of the Fresnel model which assumes the existence of an interaction radius which separates the domains of the nuclear reactions and elastic scattering. This radius, well

defined for each projectile and target system and almost independent of the energy, determines uniquely the grazing angular momentum l_{gr}, the total reaction cross section σ_R and the quarter point angle θ_{sc} [65].
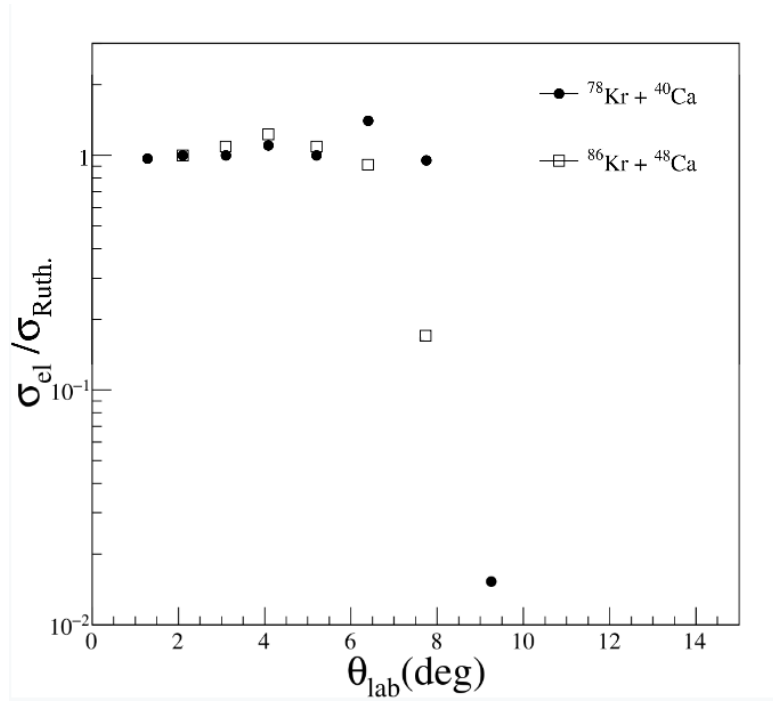

Figure 3.6: Elastic scattering normalized to Rutherford cross sections for the $^{78}Kr +^{40} Ca$ and $^{86}Kr +^{48} Ca$ reactions at 10 AMeV

A numerical integration of the cross section has been performed to take into account the angular acceptance of the detectors. In fact, experimentally the Rutherford cross section is given by:

$$\sigma_{Ruth} = \frac{N_{el}}{\Delta \Omega N_{Monitor} K} \tag{3.5}$$

where N_{el} is the number of counts for the elastic scattering and $\Delta \Omega$ is the solid angle covered, at a given angle, $N_{Monitor}$ is the number of counts in one detector chosen as current monitor and K is the normalization factor which takes into account the number of atoms inside the target and the proportional factor between

the beam current and $N_{Monitor}$. The best angular region for the choice of the normalization parameter is the flat part of the curve of the angular distribution of the elastic scattering where the relative cross section divided for the Rutherford cross section is one. The value of the ratio equal 1, at very small angles, suggest a pure Rutherford scattering. Finally, one of the Si detectors at $\theta_{lab} = 2.1°$ was considered as current monitor.

The normalization factor K obtained with this method is used to calculate all the experimental cross sections presented in the following. This procedure leads to an estimated total error of about 7% on each point in the determination of the elastic cross section.
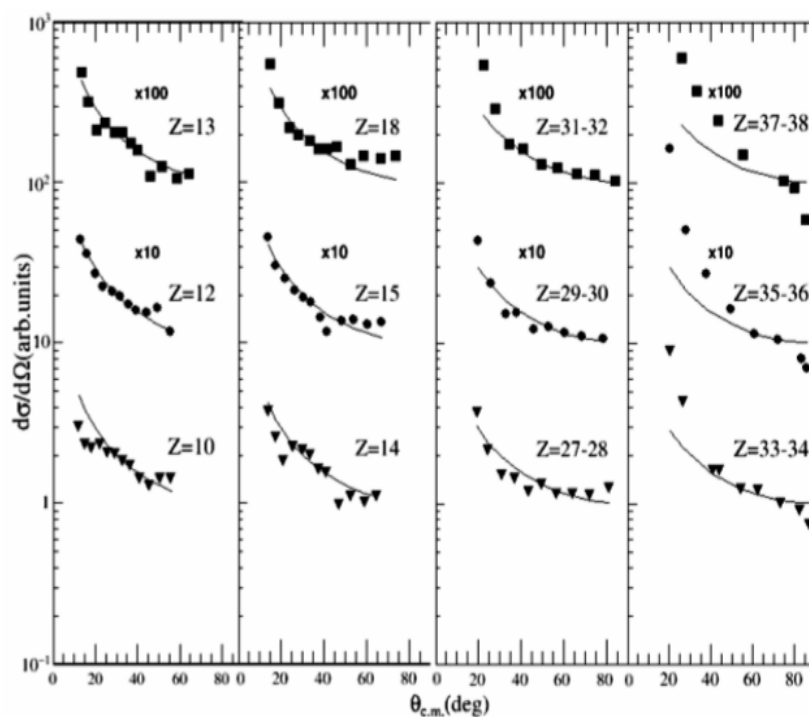
3.1.4 Angular distributions

Figure 3.7: Angular distributions, in the center of mass frame, for some Z from 10 to 38 for the $^{78}Kr +^{40}Ca$ reaction. The solid lines represent the function $1/sin\theta_{c.m.}$

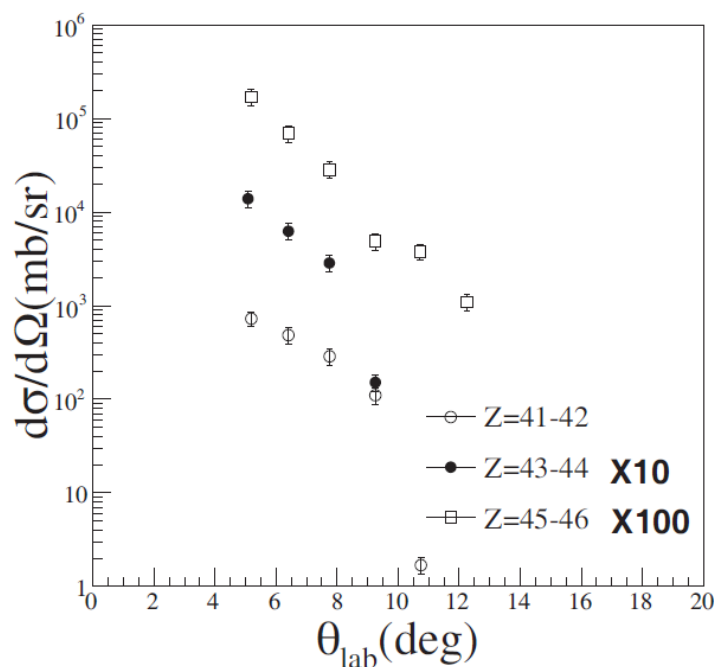Figure 3.8: Heavy ion fragments angular distributions, for the $^{78}Kr + {}^{40}Ca$ reaction.

.

Very important information about the nature of the processes involved can be extracted from the angular distributions of the emitted fragments. In fact, it is possible to distinguish globally equilibrated processes, fission and evaporation following the compound nucleus formation, from partially equilibrated processes. Fig. 3.7 reports some examples of angular distributions in the center of mass frame of fragments with various Z. The data are in good agreement with the $1/sin\theta_{c.m.}$ curve (full line), which is the shape expected for a production from an equilibrated source and thus an emission with the same probability at all angles. This behavior is characteristic of production via a long lived system, with a lifetime comparable to its rotational period (fission and quasi-fission) and implies a loss of the memory of the entrance channel direction. On the contrary fast processes show a preferential emission direction [62]. This trend, together with the energy spectra analysis seen in the previous paragraph, supports the conclusion that the predominant mode of fragment formation is fission, following the fusion process.

However, as we found in a very preliminary analysis, shown in the next section, a three body mechanism superposed on the binary fragmentation of an equilibrated source, cannot be excluded [68]. One can note , still in Fig. 3.7, that for Z>30 the experimental points have higher yields with respect to the $1/sin\theta_{c.m.}$ behavior, especially at small angles. This confirms the presence of an overlapping partially equilibrated mechanism involving a binary reaction process, as emerged from the analysis of the kinematic features and mass distributions. In order to, deeply, study this latter contributions in the future we will do the analysis of the coincidences between the reaction products. If we consider the angular distributions in the laboratory frame of some of the heavier reaction products (Z>40) reported in Fig. 3.8, we see that they are very strongly forward peaked, as expected in the case of evaporation residue, coming from both complete and incomplete fusion. The results shown in this section are shown for the neutron-poor system, but similar features and conclusions are obtained for the neutron-rich system.

Cross sections

The kinematic characteristics of the reaction products suggest that the fragments with $Z \leq 40$ come from the Fission-Like processes while it is possible to consider those with $Z \geq 45$, uniquely, as evaporation residues. The velocity spectra of fragments with $41 \leq Z \leq 44$ exhibit components due to a production by both Fusion-Evaporation and Fission-Like processes. Two different methods are used for the calculation of the cross sections, depending on the production reaction mechanisms.

As previous seen the angular distributions for the Evaporation Residues are very strongly forward peaked. The cross sections are very high at small angles and exhibit the maximum at angles close to zero degrees. This characteristic of the ER is a limiting factor in the accuracy of experimental results and is the major source of error in the calculation of the cross sections. In our experiment, for the reasons explained before, the Si detectors located at the polar angles $\theta_{lab} = 1.4°$, $2.1°$, $3.1°$ and $4.1°$ were covered with a shield. $5.2°$ is the angle corresponding to the first ring not shielded. Thus it was necessary to extrapolate the measured angular distributions to zero degrees. For the extrapolation we assumed that the ratio between the maximum of the cross sections and cross section at $5.2°$, calculated with the LILITA software is the same of the ratio between the yields should be obtained experimentally for these two angles. The unknown maximum exper-

imental yields are obtained by multiplying the ratio calculated with LILITA [67], by the number of counts at 5.2°. After we have obtained the cross sections of ER by integrating the experimental angular distribution completed with that extrapolated to zero degrees.

The production cross sections for each fission fragment σ are obtained by integrating the inclusive angular distributions seen previously, following the $1/sin\theta_{c.m.}$ behavior and by applying the normalization parameter extracted from the elastic scattering:

$$\sigma = \int \frac{d\sigma}{d\Omega} d\Omega = \int \frac{a}{sin\theta_{c.m.}} \frac{1}{k} \frac{1}{N_{Monitor}} d\Omega \qquad (3.6)$$

where $a = \frac{N_{c.m.}}{\Omega_{c.m.}} sin\theta_{c.m.}$ is a normalization factor, obtained for each fragment at the angle for which $\frac{a}{sin\theta_{c.m.}}$ best fit the experimental angular distribution. $N_{c.m.}$ and $N_{Monitor}$ are the number of counts respectively in center of mass frame and of the monitor in the laboratory frame.

The overlap of the contributions for Z = (41–44) from fission-like processes and fusion evaporation, is observed in particular at forward angles, while beyond the angle, corresponding to the ring 5 of CHIMERA, just the production through fission-like is expected. We have estimated the fission-like contribution to the yields from the normalization factor a by the method described in the following. We have calculated a at an angle where the contribution of the evaporation residues is not present in the yields. By using the Jacobian (seen previously) it is possible to express a as function of $\theta_{c.m.}$ and other quantities in the laboratory frame, as the number of counts N_{lab}, the velocity v_{lab} and the angle θ_{lab}. For each angle N_{lab}, the contribution of the production from fission-like processes to evaporation residues, is estimated by the expression of the normalization factor a in the laboratory frame, and then subtracted from the total yields.

The final obtained results are reported up to Z = 38 in Fig. 3.9, charge by charge for fragments directly identified (Z ≤ 17) and by averaging Z cross sections for two consecutive charges, for fragments whose atomic number is reconstructed, (Z ≥ 17). The known underestimation of the berillium yields is due to the missed ^8Be detection because ^8Be is an unstable isotope that decays in 2 alpha particles. Since, in general, the neutron rich system prefers to produce more neutron rich isotopes of the same element respect to neutron-poor one, this reduction in Be yields is more evident for the neutron poor system than the neutron rich one.

A strong even-odd staggering effect in the charge distributions is observed. This effect is due to a preferential production of fragments with an even value of
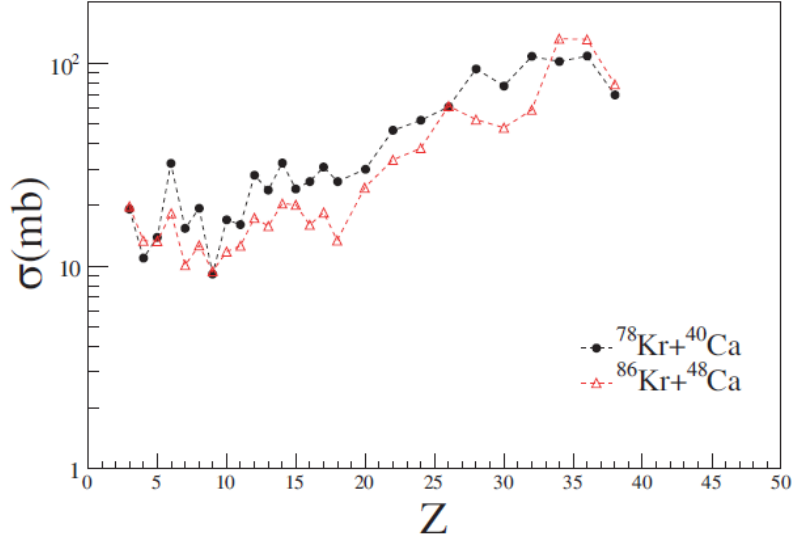
Figure 3.9: Charge distribution for the two systems

the atomic number, because of the greater stability, due to larger binding energy. We found, in agreement with some other examples in the literature, [69, 70, 71] that the staggering is more pronounced for the neutron poor system than the neutron rich one, in particular, it is observed for $Z \leq 10$ reaction products. This effect persists also for charges $Z \geq 10$, albeit with a smaller amplitude. It is not possible to observe the staggering for $Z \geq 17$, because the cross sections were grouped two by two. We can also note that fragments production is globally favored in the $^{78}Kr + ^{40}Ca$ reaction, for which the cross sections are systematically higher. The neutron enrichment seems thus to lower the cross sections of the lighter fragments, whose production can also be affected by structure effects, related to the pairing forces [72]. The experimental charge distributions in both systems show an asymmetry around $Z = 28$, which would correspond to the symmetric fission fragments . The choice to integrate over angular distributions along the $1/sin\theta_{c.m.}$ lines seems to be insufficient to remove all the contamination of this very dissipative binary process, not fully relaxed in mass. One possibility to exclude it could be the use of the completeness of the event, in fact because of the target-like fragment loss in the event reconstruction, the total detected mass would be too low. The "complete events", are selected by imposing the condition of a to-
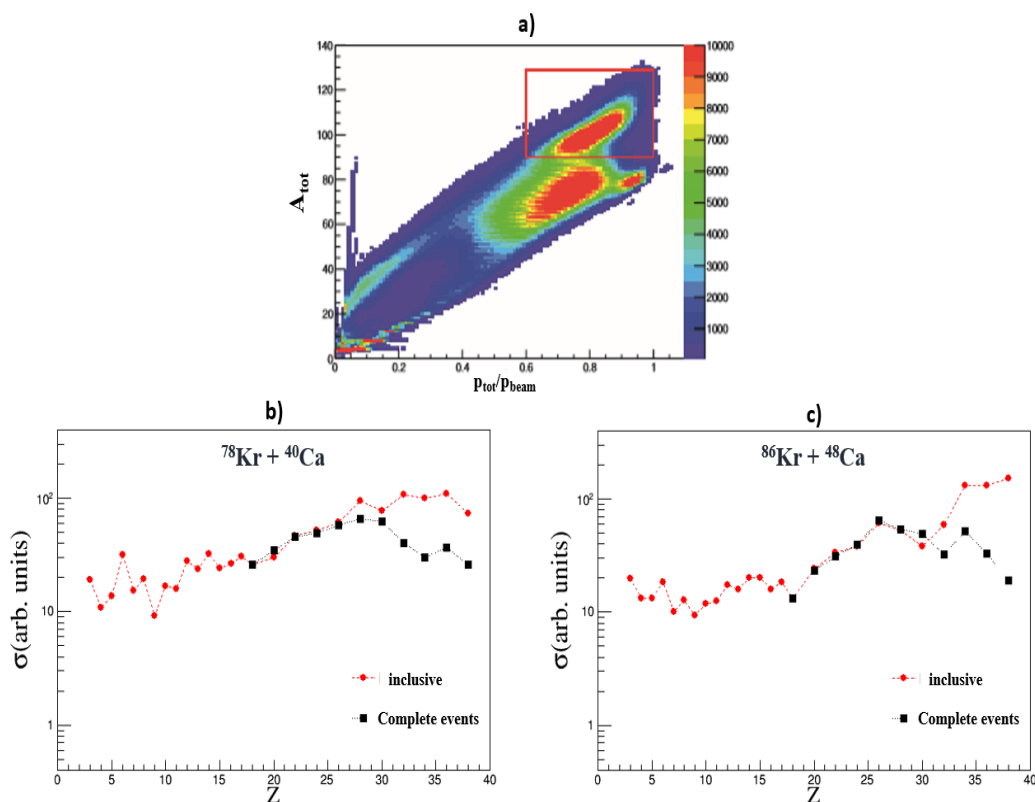
Figure 3.10: Two-dimensional plot showing the total detected mass as a function of the total transferred momentum a). Charge distribution, in arbitrary units, in red for an inclusive analysis and in black with a complete events selection, on b) for the n-poor system and on c) for the n-rich one

tal measured momentum, p_{tot}, in the range 0.6 $p_{beam} \leq p_{tot} \leq 1.0 p_{beam}$, where p_{beam} is the total beam momentum, and a total detected mass A_{tot}, in the range $0.75 \, A_{CN} \leq A_{tot} \leq 1.1 A_{CN}$, for both systems. In the two-dimensional plot of Fig. 3.10 a), showing the total detected mass as a function of the total transferred momentum for the system $^{78}Kr + ^{40}Ca$ (normalized to the beam momentum), the "complete events" are those which lie in the red rectangle. It is possible to recognize quasi-elastic scattering and DICs processes, corresponding to the two regions centered at A = 80, p_{tot}/p_{beam}=0 .90 and at A = 75, p_{tot}/p_{beam}= =0 .75, respectively. A similar result is obtained for the $^{86}Kr + ^{48}Ca$ reaction. Charge distribution, in arbitrary units, in red for an inclusive analysis and in black with

a complete events selection, normalized to the point corresponding to $Z = 20$, are displayed for the n-poor system and for the n-rich one in Fig. 3.10 b) and c) respectively. As evident for exclusively complete events, the charge distributions
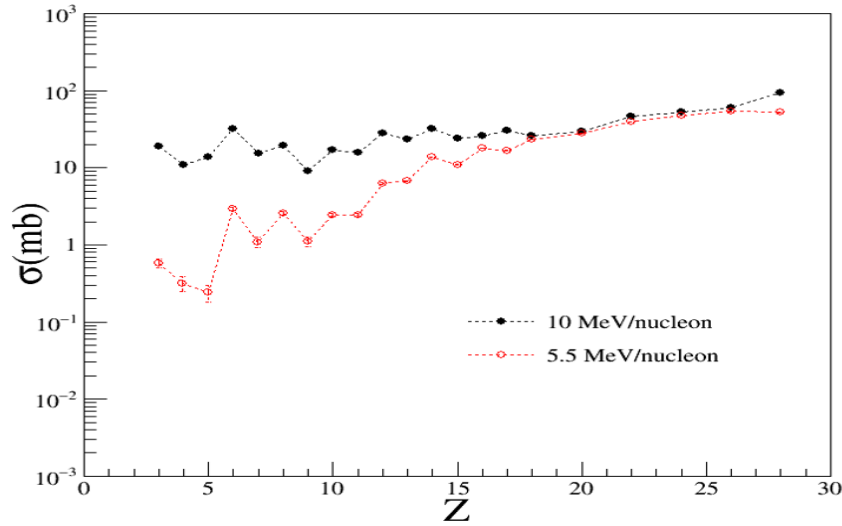

Figure 3.11: Charge distribution for the $^{78}Kr + ^{40}Ca$ reaction at two different energies (in red at 5.5 AMeV and in black at 10 AMeV)

are clearly symmetric, around $Z = 28$ for the neutron poor system and around $Z = 26$ for the neutron rich one. Thus the contamination of the fragment yields by DICs starts from around $Z = 30$ and 28 for poor and rich system respectively.

It is possible to compare the charge distribution of the fragments for the system $^{78}Kr + ^{40}Ca$ with the results for the same system at lower energy, 5.5 AMeV available up to $Z = 28$ [70], as shown in Fig. 3.11. One can note that for all the fragments, the cross section is systematically larger at higher energy, and the difference decreases with increasing of the atomic number, Z. This trend (in agreement with [73]) confirms the obtained results by considering the kinematic features of the produced fragments. In fact, at the both energies the behavior of energy spectra and angular distributions indicates that the fragments are emitted by an equilibrated composite system formed in the fusion process between projectile and target. However at lower energy the favored decay mode is the evaporation process, in which there is a large production of light particles, while at higher

energy the fusion-fission channel prevails, with a higher relative production of heavier fragments.

The measured production cross section for each fragment can provide an estimate

	σ_{ER} (mb)	σ_{FL} (mb)	σ_{fus} (mb)	l_{fus} ($\hbar$)	σ_{react}^{qp} (mb)
$^{78}Kr + ^{40}Ca$	455 ± 70	850 ± 120	1305 ± 190	117	2390 ± 250
$^{86}Kr + ^{48}Ca$	400 ± 60	530 ± 85	930 ± 105	115	2520 ± 260

Table 3.1: Evaporation-Residues, Fission-Like, Fusion and total quarter point reaction cross sections for the two reactions

.

of contributions of different decay modes of the composite systems in the two reactions. In particular, the cross section for evaporation residues are obtained by considering all fragments with $Z \geq 40$. Note that the contribution of fission-like processes to the yield of very heavy fragments (Z =41–44) has been evaluated, as previously explained, and subtracted from their production cross sections, in order to obtain just the evaporation contribution.

The cross section for all fission-like mechanisms are calculated by summing the contributions from $Z = 3$ to Z=28/26 for neutron poor/neutron rich system respectively, which correspond to the maximum yield in charge distributions. This will exclude from any contamination from DICs, whose contributions were discussed above. The results obtained, l_{fus} calculated from the σ_{fus} value, and the values for reaction cross section obtained with the quarter point formula [74] are reported in table 3.1. Errors are a combination of the uncertainties in the integration procedure of the angular distributions and in the uncertainties in the calculation of the normalization constant. The already cited unequilibrated binary decay, more pronounced for the neutron rich system, could be the responsible of the difference between these values and the total reaction cross sections. The neutron poor system shows globally more fusion than the neutron rich one in fact, while the fusion evaporation probability is comparable for the two systems, the fusion-fission

probability is much higher for the neutron poor system. The neutron enrichment seems thus to limit the formation of the composite system and to inhibit the fission decay channel. This behavior could be due to very different fission barriers for the two barium isotopes. However it should be noted that the values experimentally obtained for l_{fus}, for both systems, are higher than the values of the angular momentum for which fission barrier drops to zero [21] ($l_{Bf=0} = 90\hbar$ and $l_{Bf=0} = 98\hbar$ for neutron poor and rich respectively). The contributions of the partial waves with higher values of the angular momentum, corresponding to quasi-fission events, should be considered as fission events. The larger difference between l_{fus} and $l_{Bf=0}$, and thus the higher contribution of fast-fission, for the neutron poor system, should explain why Fission-Like cross section are larger for this system.
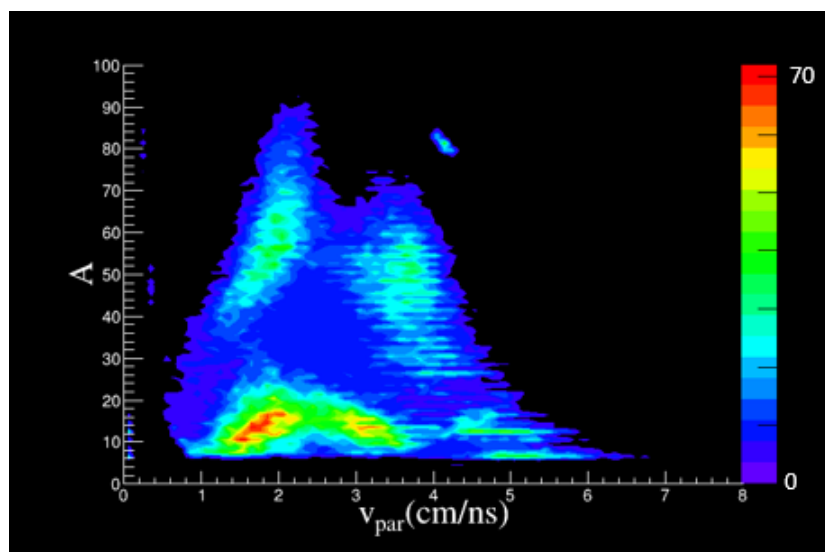
3.2   PLF Break-up

Figure 3.12: Correlation between the fragment mass and parallel velocity of the reaction products in events with 3 IMFs well detected and identified.

In literature many indications about the break-up of the Quasi-Projectile are reported ([75] - [81]). Processes with three fragments of nearly equal size in the final state, were observed in about 10 AMeV Ar and Fe induced reactions [83, 84].
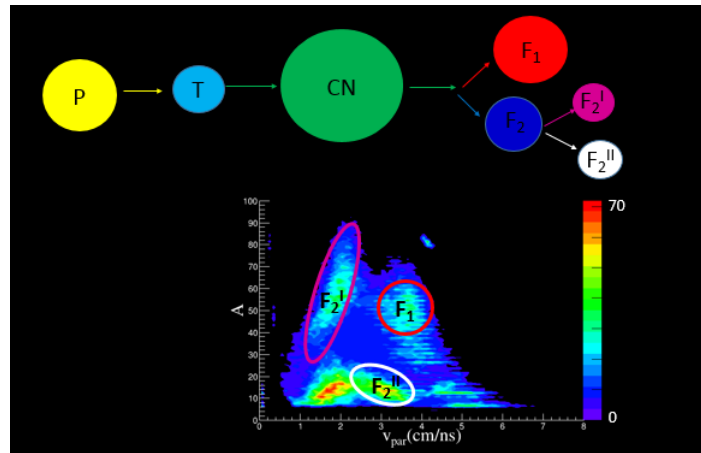
Figure 3.13: schematic representation of the break-up of the slow fragment produced in the fission of the Compound Nucleus, and localization of the fragments produced in the mass versus parallel velocity plot in events with 3 IMFs well detected and identified.

In these early experiments it was not possible to establish if fragments are produced by statistical fission following a conventional dissipative collision or in a dynamical process. In later experiments [85, 77] an evidence of the dynamical nature of the PLF breakup, for a part of the ternary events, was found by Glassel *et al.* in $^{129}Xe + \,^{122}Sn$ reaction at 12.5 AMeV and later by Stefanini *et al.* in $^{100}Mo +^{100} Mo$ and $^{120}Sn +^{120} Sn$ collisions at about 20 AMeV. In both these studies the coexistence of the dynamical partitioning processes with the statistical fission of one of the reaction partners was observed.

This ternary process is largely studied also by the CHIMERA collaboration ([86] - [89]), in experiments performed with systems of different sizes and at various bombarding energies. For example, in $^{197}Au +^{197} Au$ collisions at 15 AMeV, it was found that ternary break-up belong to the same wide class of deep inelastic collisions as the conventional binary dissipative reactions. Moreover, in the same study, it was showed that while at more peripheral collisions, binary deep inelastic reactions occur, extremely inelastic collisions lead to the ternary break-up at small impact parameters.

It should be emphasized that the mechanism of ternary breakup into fragments of comparable size, observed in reactions realized at energies below 20 AMeV, should not be mixed up with the neck fragmentation processes, typical of the
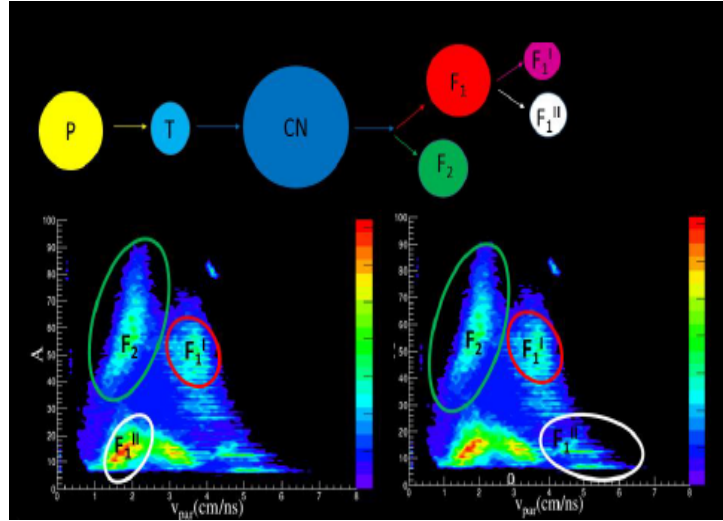
Figure 3.14: Schematic view of the break-up of the fast fragment produced in the fission of the Compound nucleus, and localization of the fragments produced in the mass versus parallel velocity plot in events with 3 IMFs well detected and identified.

Fermi-energy domain [80, 81]. At higher energy, in the experiments REVERSE ($^{124,112}Sn + ^{64,58}Ni$ at 35 AMeV) and InKiIsSy ($^{124}Xe + ^{64}Zn$, $^{124}Xe + ^{64}Ni$ at 35 AMeV) [82], one of the most important results observed is an evident influence of the $\frac{N}{Z}$ ratio of the entrance channel on the dynamical break-up of the Quasi-Projectile [50, 51, 89]. Thus also at low energy it is expected that the isospin should play a crucial role.

In agreement with other cases in literature [90, 85], the experiments, performed by the CHIMERA group have evidenced the angular distributions alignment of the massive fragments emitted in the dynamical break-up of the PLF. A possible explanation of the ternary aligned breaking at low energy, the energy domain in which the reactions of interest ($^{78}Kr + ^{40}Ca$ and $^{86}Kr + ^{48}Ca$) are realized, is given by Shvedov, Colonna and Di Toro [91]. These effects could still be explained in terms of the persistence of the excitation of shape and rotational modes in the projectile-like (PLF) fragments that are formed in binary-like events, that would lead to further reseparation along a preferential axis. In previous sections of this chapter we have presented the study of Fusion-Evaporation and Fission-Like processes in reactions $^{78}Kr + ^{40}Ca$ and $^{86}Kr + ^{48}Ca$ at 10 AMeV, in particular
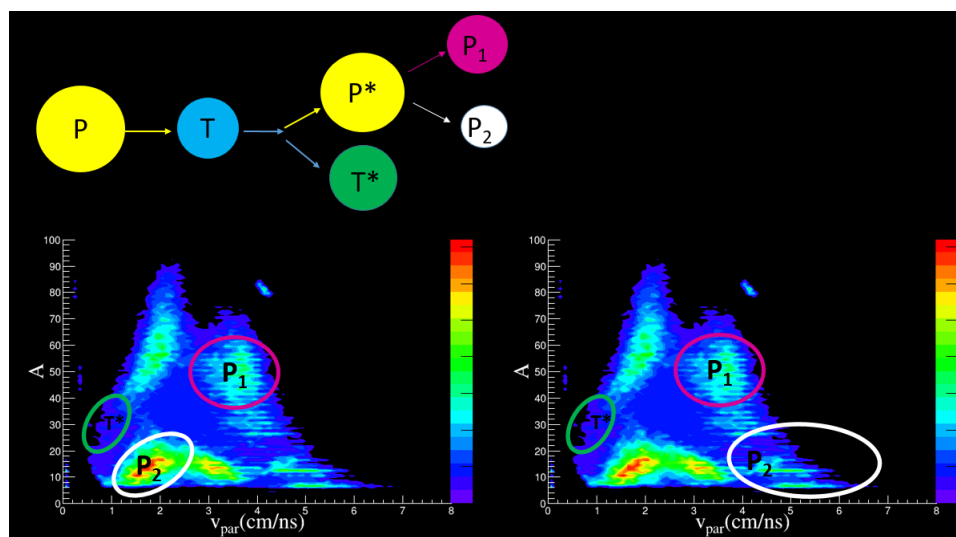
Figure 3.15: Schematic view of the break-up of the PLF and localization of the fragments produced in the mass versus parallel velocity plot in events with 3 IMFs well detected and identified.

putting on evidence the influence of isospin on the fragments production.

The reactions studied offer also the possibility to investigate the Projectile-Like Fragment (PLF) binary splitting into two massive fragments after very dissipative peripheral collisions. Before to show the results relative to the analysis of the PLF break-up, we will present a selection method, developed in order to discriminate the splitting of the PLF from events due to the other mechanisms, which populate the same region of the phase-space. In fact, because of the low energy, the available phase space is reduced and an overlap of contributions of different processes is observed. For both reactions we looked just at events with three IMF ($Z \geq 3$), well detected and identified. For reasons which will be clarified later, our selection criterion of considering only events with three IMF derives from the requirement that one of them is the Target-Like Fragment. The requirement of the recording coincidence of the PLF and TLF will result in the limitation of available phase-space and in a drastic reduction of the statistic. Despite of the high performance of the CHIMERA multidetector, the TLF detection efficiency is very low, due to threshold.

For a general idea about the processes involved, one can look at the correlation between the fragment mass and parallel velocity of the reaction products. The

plot, constructed with the starting condition of requiring contemporary detection of three Intermediate Mass Fragments and shown for the neutron-poor system in Fig. 3.12, is populated from different reactions mechanisms: the break-up of the slow fission fragment from Compound Nucleus FF_{slow}, the break-up of the fast fission fragment from Compound Nucleus FF_{fast} and the break-up of the PLF. It should be noted that the value of the masses are obtained by using the Time of Flight technique and the velocity are directly measured.

After its formation the Compound Nucleus could decay though fission and then the slow fission fragment can break-up into two fragments. In this case we observe, due to threshold and detector efficiency, just the kinematical solution where the light fragment is emitted in forward direction. As shown in Fig. 3.13 at the end of this process one can observe three body: the fast fragment emitted in the fission of the Compound Nucleus (F_1) and the two fragments produced in the break-up of the slow- fission fragment (F_2^I and F_2^{II}).

The other case which can we meet is the one, in which, after the fission of the Compound Nucleus, the fast fragment produced, breaks up into two massive fragments, and the three body in the final state are: the slow fragment produced in the fission of the Compound Nucleus (F_2) and the two fragments due to the break-up of the fast- fission fragment (F_1^I and F_1^{II}), with the lighter fragment backward or forward emitted Fig. 3.14. A final reaction mechanism, which is the process which we are interested in, is the break-up of the projectile. In these events one of the three fragments is a part of the Target-Like Fragment (T^*) and the other two fragments originate from the break-up of the PLF (P_1 and P_2), with the lighter backward or forward emitted Fig. 3.15. In any event with three-body in the final states, there are three possible pairs of fragments coming from the decay of an intermediate system (PLF, fast fission fragment and slow fission). The source of each combination of fragments pairs, in events with the total multiplicity of the particles equal three, was reconstructed as the center of mass of such subsystems. By examining Fig. 3.16, in which the mass versus parallel velocity plot for the reconstructed source is shown, it is possible to recognize three source: the slow fragment emitted in the fission of the Compound nucleus (F_2), the PLF (P^*) and the fast fission fragment (F_1), these latter populate the same region of the plot. In our selection method in order to be sure to take into account only events due the PLF break-up we required that the reconstructed source of two fragments is $(P^*)^*/(F_1)$ and that the third fragment, which is the partner of the source, does not belong to the slow branch of fission from Compound Nucleus.
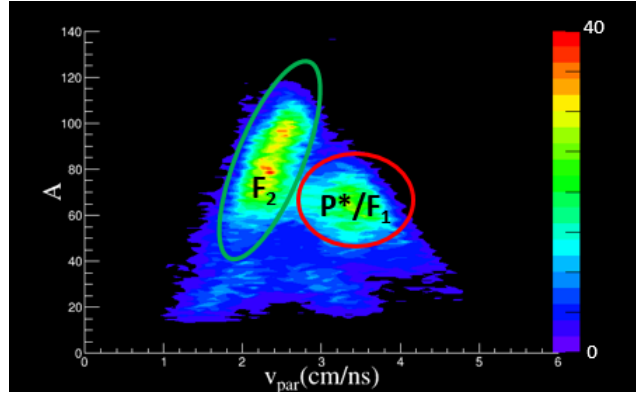
Figure 3.16: Mass versus parallel velocity plot of the reconstructed source of each combination of two fragments in events with 3 IMFs well detected and identified.

The pictures shown until now regard the $^{78}Kr + {}^{40}Ca$ system, but similar results have been obtained for the $^{86}Kr + {}^{48}Ca$ system, thus the same approach is applied to the selection method for this system. Finally the correlation between the mass and the parallel velocity of the fragments produced int the PLF break-up selected as previously explained, is shown in Fig. 3.17 on the left for $^{78}Kr + {}^{40}Ca$ and on the right for the $^{86}Kr + {}^{48}Ca$ system.

Crucial information about the nature of the break-up process can be extracted from the angular distribution in the PLF reference frame. It is useful to describe the relative motion between the PLF and TLF in the reference frame of the total system, while the relative motion of the (P_1 and P_2) subsystem in the reference frame of the reconstructed PLF.

As seen previously the main signature of a dynamical break-up is the alignment of the break-up axis with the separation direction of the two primary fragments (PLF and TLF), with the lighter breakup fragment backward emitted. A very nice observable, that allows to disentangle between statistical and dynamical break-up, is the cosine of $\theta_{proximity}$ [51]. The proximity angle is defined as the angle between the recoil velocity of the reconstructed PLF in the center of mass frame and the break-up axis oriented from the light L to the heavy fragment H Fig. 3.18.

We reconstructed the PLF velocity v_{PLF}, as the velocity of the center of mass of P_1 and P_1, when they are in anticoincidence with slow fission fragments from the CN,
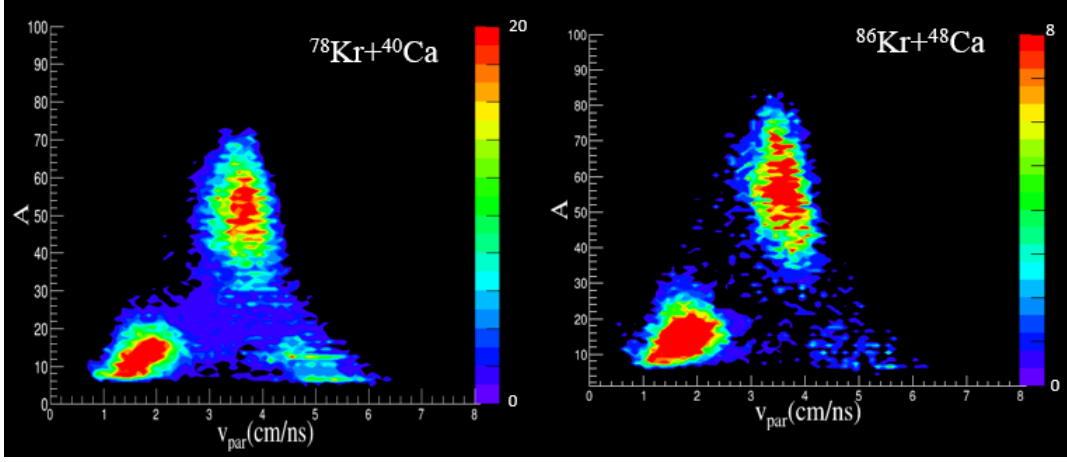
Figure 3.17: Mass versus parallel velocity lot for the PLF break-up on the left for $^{78}Kr +^{40}Ca$ and on the right for the $^{86}Kr +^{48}Ca$ system.

$$v\vec{P}_{LF} = \frac{v\vec{P}_1 * m_{P_1} + v\vec{P}_2 * m_{P_2}}{m_{P_1} + m_{P_2}} \tag{3.7}$$

and break-up or fission axis, directed along the relative velocity of the fragments v_{rel} produced in the break-up

$$\vec{v_{rel}} = v\vec{P}_1 - v\vec{P}_2 \tag{3.8}$$

In case of statistical emission of the fission fragments, the angular distribution should be symmetric with respect to $cos(\theta_{prox}) = 0$ and isotropic in the reaction plane because a preferential emission direction doesn't exist. The spin effect, if there is any, is to favor the reaction plane, and thus the angular distributions should be slightly peaked around $cos(\theta_{prox}) = \pm 1$, but maintaining the symmetry with respect to $cos(\theta_{prox}) = 0$. The main signature of the dynamical emission is a strong anisotropy of the angular distributions of the break-up fragments in the reaction plane. The alignment of the three fragments proves the persistence of the memory of the previous deep inelastic step and in particular of the direction of the separation axis between PLF and TLF . The obtained distribution in θ proximity, for different mass asymmetry parameters (A_H/A_L), when the reconstructed PLF is in anticoincidence with the slow fission fragment from CN, are shown in purple for $^{78}Kr +^{40}Ca$ and in green for $^{86}Kr +^{48}Ca$, in Fig. 3.19. The area of each
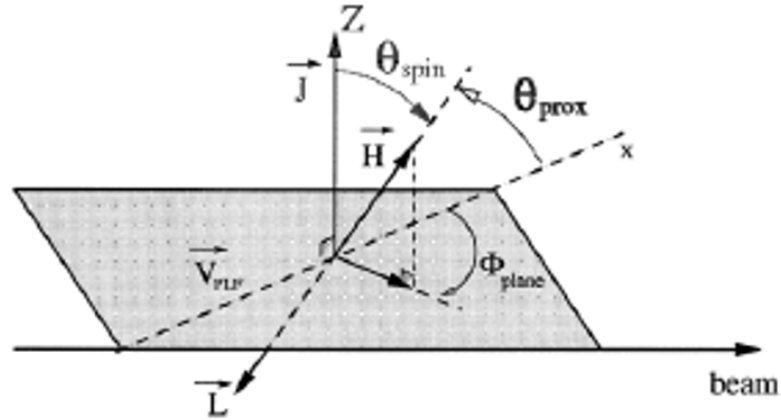
Figure 3.18: A schematic view of $\theta_{proximity}$, defined as angle between the recoil velocity of the reconstructed PLF in the center of mass frame and the break-up axis oriented from the light L to the heavy fragment H.

contribution are normalized to the unity.

For almost symmetric splitting ($1 < A_H/A_L < 1.6$) even if there is an anisotropy in the angular distribution, its amplitude is very small, in particular for the neutron-poor system. By increasing the mass asymmetry, for both systems one can observe that the distribution are peaked around 1, independently of A_H/A_L, suggesting a preference for a dynamical break-up. After its interaction with the target the PLF highly excited inevitably de- excites through a very fats break-up.

These dynamical effects seem to be more pronounced for the neutron rich system, in agreement with the results obtained in previous experiments performed at higher energy from the CHIMERA group [90].

In order to be sure that this effect is not due some error in our selection procedure, we have done the distribution when the reconstructed source is the fast fission fragment from CN, thus when P^*/F_1 is in coincidence with the slow fission fragment, and we have obtained a flat distribution as it is expected in the case of fully statistical break-up.
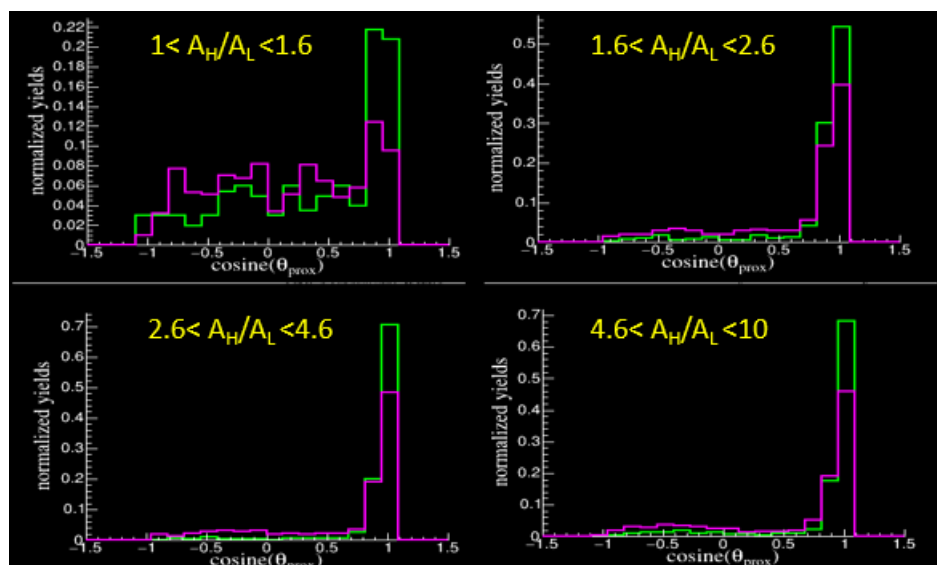
Figure 3.19: Distribution in cosine of θ proximity for the two studied systems (in purple for $^{78}Kr +^{40}Ca$ and in green for d $^{86}Kr +^{48}Ca$ reactions) at different values of A_H/A_L ratio.

3.3   Comparison with theoretical models for capture reactions

Many phenomena are present in the reaction mechanisms and in the process of de-excitation of the excited nuclei in these collisions. The description of an initial state consisting of two nuclei with a given kinetic energy and a final state consisting of a multitude of products of different size involves many degrees of freedom (relative distance between nuclei , quadrupole moments, development of a neck between the nuclei, asymmetry of mass, isospin, etc ...) and the couplings between these collective degrees of freedom and intrinsic degrees of freedoms (relaxation of the relative energy, transfer of angular momentum and excitation energy in fragments, isospin relaxation, etc. ...). In the wide variety of models to describe the process of de-excitation, we need an approach, able to treat the distribution of fragments covering a wide range of the region of masses (from light charge particles and Intermediate Mass Fragments up to fission fragments and evaporation residues) and high angular moments. These aspects, suggested by the characteristics of the reaction products in our data, are satisfied by different

models, $GEMINI++$, HIPSE and the Dinuclear System model.

Comparison with HIPSE followed by GEMINI++ code

HIPSE (Heavy-ion Phase-Space Exploration) [92] is a phenomenological model developed by D. Lacroix, dedicated to the description of heavy ion collisions, allowing a detailed comparison with experimental data and accounting for both dynamical and statistical effects. The model, with the main goal to identify minimal physical hypothesis to reproduce experimental data, allows the access to partitions before and after statistical decay. The macroscopic-microscopic "phenomenology" of the HIPSE model combines two extreme approaches, namely, the statistical approach based on the reduction of the reaction to a few important parameters [93, 94] and the microscopic approach based on the transport theory [95] - [98]. HIPSE has only three free parameters all depending just from the beam energy, in fact, in order to be predicted, the model was developed with the philosophy to provide an event generator where the parameters are independent of the entrance channel. The values of the parameters (Hardness of potential, percentage of exchange, percentage of nucleon-nucleon collisions) area tabulated by the authors of the model, for different beam energy, in particular also for 10 AMeV.

The reaction is described in three steps. First there is the approaching phase of the collision, which ends at maximum overlap of the two partners. This phase is considered by solving the classical equation of motion of the two partners in their mutual interaction potential.

In the second phase one can observe the formation of the so called "partition", the rearrangement of the nucleons into several clusters and light particles according to the impact parameter of the reaction. The partition is built following coalescence rules in momentum and position spaces. As main consequence of this approximation, a strong memory of the entrance channel will be reflected in the angular distributions and the kinetic energy of species produced in highly fragmented collisions.

The last step is the exit channel and after-burner phase up to the detectors. This phase consists in propagating the fragments in the Coulomb field and possible reaggregation effects due to the strong nuclear and Coulomb interactions among the various species of the partition are considered. If the fragments are generated in excited states, secondary decays are taken into account by means of an

evaporation code. In general the decay is achieved by using the SIMON event generator [99], which takes into account all the decay channel from neutron evaporation up to symmetric fission. However SIMON presents some known problems, emerged in the comparison between the data and HIPSE: iso-scaling is not in de-excitation code and fission is overestimated compared to the data for heavy fragments [100]. For this reason we have used $GEMINI + +$ code [58] for de-excitation of the fragments produced by HIPSE. Moreover $GEMINI + +$ was compared to a large number of experimental data, relative to experiments involving systems of different size and produced by using a large range of beam energies. We performed our calculation by using the value of $A/7$ for the level density parameter in $GEMINI + +$ code, because in different test which we have done in the comparison between just $GEMINI + +$ and the experimental data, $A/7$ was the best in reproducing the experimental results.

HIPSE can conveniently simulate heavy-ion interactions at all impact parameters and thus is a good tool for the understanding of processes in peripheral or/and central collisions. For the neutron-poor system at beam energy of 10 AMev, in Fig. 3.20 the correlation between the mass and parallel velocity to the beam direction, of the fragments produced by HIPSE are shown after the de-excitation by $GEMINI + +$, for different range of the impact parameter b. It should be noted that of course also primary fragments produced by HIPSE with a low excitation energy, and thus not de-excited by GEMINI stage, are considered in the plot. .

In central collisions (Fig. 3.20 a)), at very small parameters ($b < 2 fm$), the only reaction mechanism present is the fusion-evaporation, in fact masses are centered around 100 and have values of the velocity close to the Compound Nucleus velocity (2.79 cm/ns). By increasing the impact parameters it is possible to observe the contribution of other processes. In the range between 2 fm and 4 fm (Fig. 3.20 b)) one can observe also the two branches due to the two possible solutions of the fission-Like processes. For $4 < b < 6$ fm (Fig. 3.20 c)) there is an overlap of the contributions of different reaction mechanisms: Fusion-Evaporation, Fission-Like processes and Deep Inelastic Collisions. In fact DIC start to come into play as evidenced by the higher presence of fragments with $A \sim$ mass of the target (40) and $A \sim$ mass of the projectile (78). If the enhancement in the yields of such mass zones was due to fission-like processes, the two Kinematical solution would symmetrically populate the branches of the plot and this is not the case. In peripheral collisions ($6 < b < 8$) fm (Fig. 3.20 d)) just the contribution of DIC is observed. Similar results were obtained for the neutron-rich system.
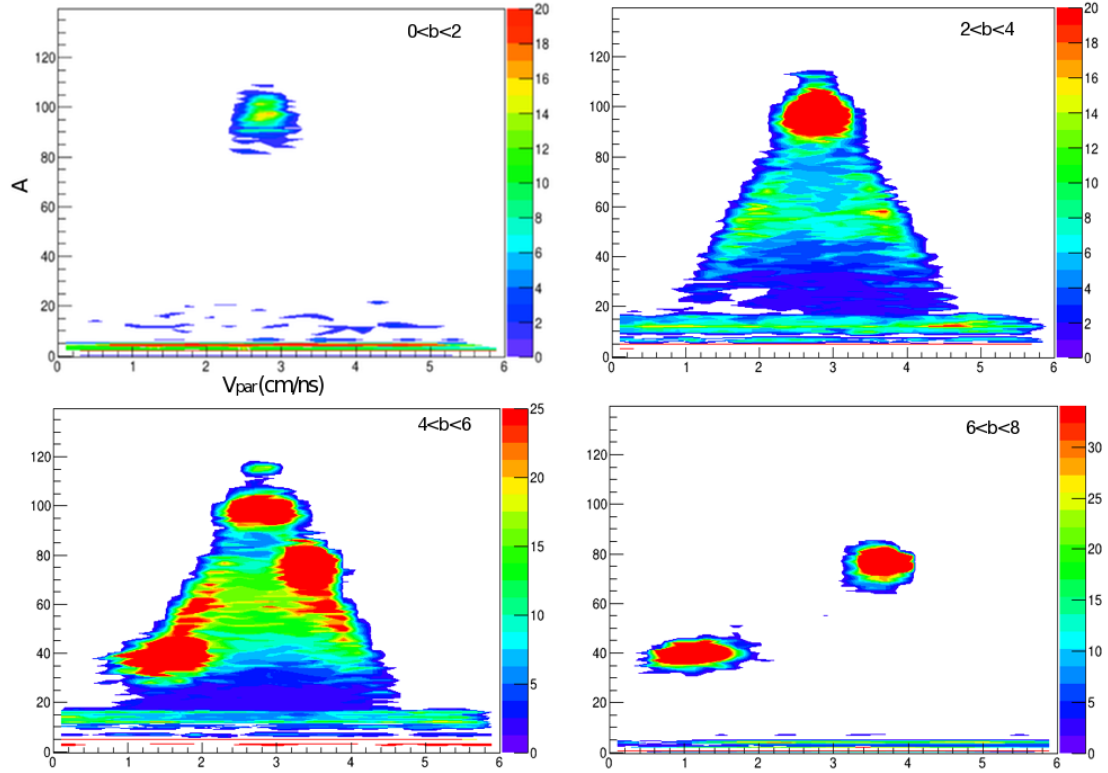
Figure 3.20: For the neutron-poor system, mass versus parallel velocity plot, for fragments produced by HIPSE followed by GEMINI++ at different range of the impact parameter. The results obtained for the considered range $b < 2$, $2 < b < 4$, $4 < b < 6$, and $6 < b < 8$ are shown, in panel a),b), c) e d) respectively

In order to compare the HIPSE predictions to the production cross section, obtained for $^{78}Kr + ^{40}Ca$ and for $^{86}Kr + ^{48}Ca$ reactions at 10 Mev/nucleon, the theoretical calculation uses as maximum impact parameter the value deduced from the experimental data. The impact parameter, as defined in the first chapter, is the perpendicular distance from the asymptotic trajectory of the projectile, during its approaching to the target, to the parallel line passing trough the center of the target nucleus. It is not a direct measurable quantity but can be related to global variables, calculated from experimental data. In the Fermi energy domain and at relativistic energy, multiplicity, which is the simplest observable linked to the

violence of the collision, is exploited for the estimation of the impact parameter through the method of Cavata [101].
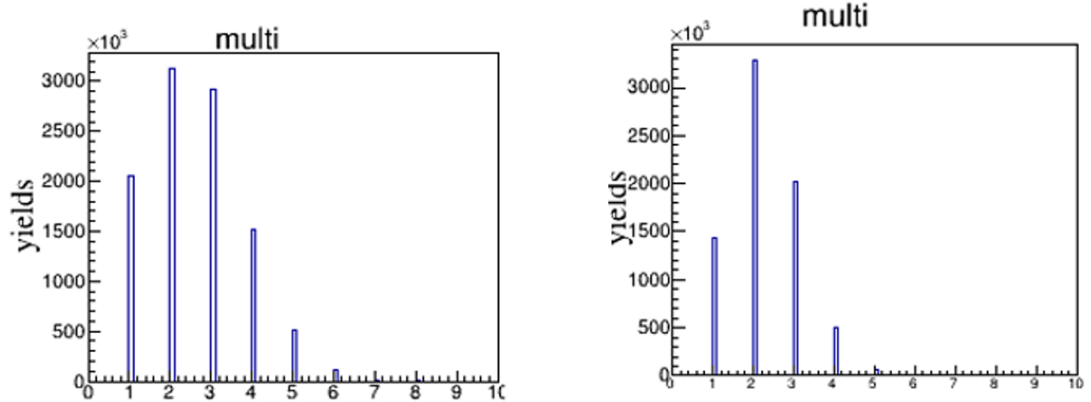

Figure 3.21: Total charged particles multiplicity, on the left for the $^{78}Kr + ^{40}Ca$ and on the right for $^{86}Kr + ^{48}Ca$ reactions at 10 AMeV

The low energy domain is characterized by very low multiplicity and thus multiplicity is not a good observable to use as centrality selector. Fig. 3.21 shows the total charged particles multiplicity, the total number of fragments detected in each event, for the two studied system at 10 AMeV, in particular on the left for the $^{78}Kr + ^{40}Ca$ reaction and on the right for the reaction $^{86}Kr + ^{48}Ca$. We can observe the tendency of the neutron-poor system to produce higher multiplicity respect to neutron-rich one. Probably this may be explained by considering that, in neutron-rich nuclear reactions, light clusters with an excess of neutrons are more likely to be emitted and de-excitation of these fragments should involve the emission of neutrons, while the neutron-poor clusters de-excite more easily by emitting protons. With the CHIMERA device we are able to detect just charged particles and thus the missed detection of neutrons lowers the total multiplicity, mainly for the neutron-rich system.

Because of the impossibility to apply the Cavata method, we have estimated the impact parameter from the experimental fusion cross section, presented in tab3.1. We have obtained the values ~ 6.5 fm for the system $^{78}Kr + ^{40}Ca$ and ~ 5.4 fm for the $^{86}Kr + ^{48}Ca$ system. It should be considered that the HIPSE calculation, performed by using these maximum impact parameters, provide values of J_{max} lower than the experimental values, $J_{max} \sim 80\hbar$ for the neutron-poor system and

$J_{max} \sim 100\hbar$ for the neutron-rich one.
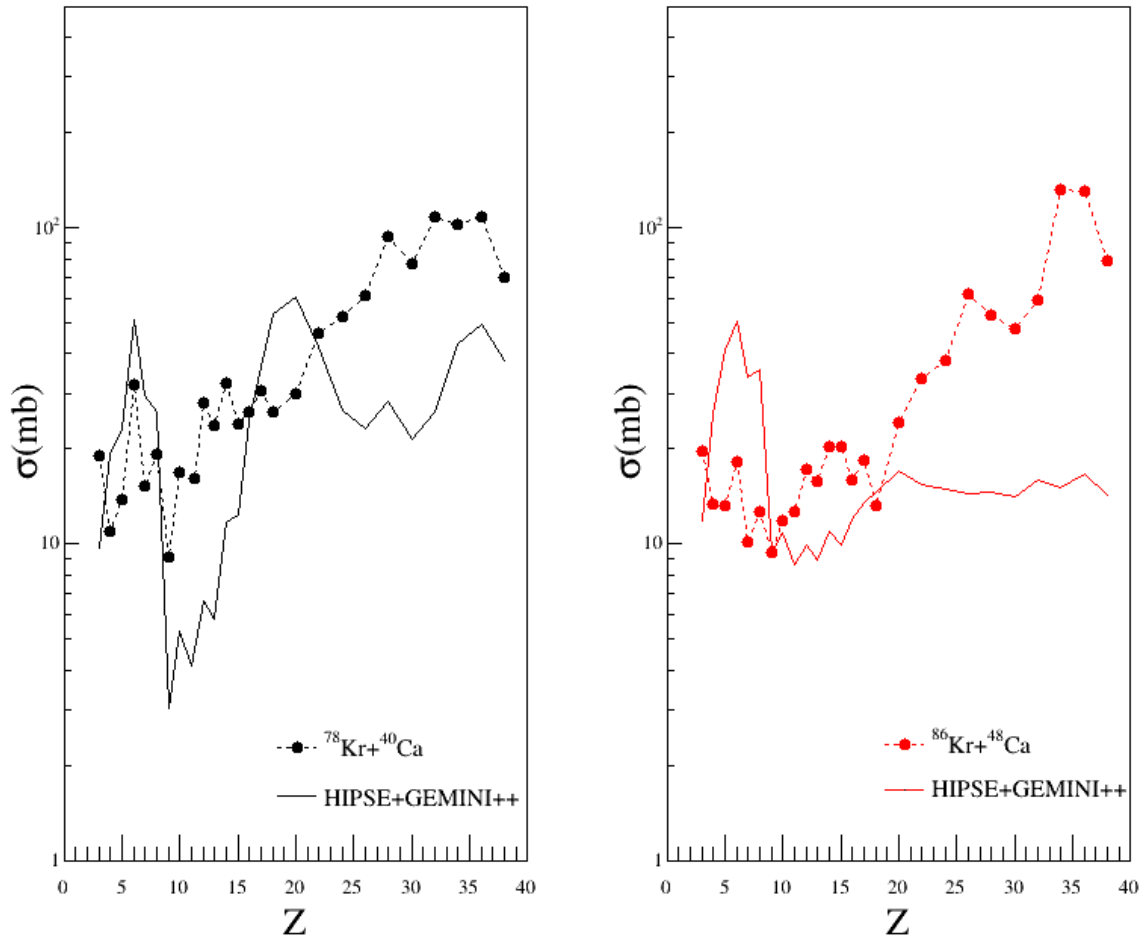
Figure 3.22: Comparison for the two systems between experimental charge distribution and HIPSE followed by $GEMINI++$, with the maximum impact parameter obtained from the experimental fusion cross sections

The charge distribution calculated by HIPSE, followed by $GEMINI++$ (solid line) are compared to our data and the results are shown in Fig. 3.22 in black for neutron poor system and in red for the neutron-rich one. It is evident that in the comparison with the neutron-poor system the cross sections of fragments with $3 \leq Z \leq 8$ are overestimated while an underestimation of those of reaction

products with $10 \leq Z \leq 15$ is observed. A possible explanation is that these latter fragments are produced so excited to undergo to secondary decays and their de-excitation populates the region of charge between 3 and 8. Analogous consideration should be made for the neutron-rich system.

The contribution of the Deep Inelastic Collisions are taken into account, by using the considered values of the maximum impact parameter just for the neutron-poor system, as emerged from the Fig. 3.23, where A vs parallel velocity plot is shown on panel a) for $^{78}Kr + ^{40}Ca$ system and on panel b) for the $^{86}Kr + ^{48}Ca$.

This should provide a possible explanation for the enhanced production of fragments with $17 \leq Z \leq 21$ obtained with the model for the neutron-poor system. In fact, this region, with values of the charge very close to that of target, should be populated by fission from CN and by conventional binary deep inelastic, however a correspondent enhancement on the cross section of the partner of these fragments is not observed. Maybe, according to HIPSE model, there should be a contribution of another reaction mechanism, the almost symmetric splitting of the PLF, following a very dissipative collision. After this process, three fragments of nearly equal size are expected in the final state, two coming from the break-up of the PLF and the third is the TLF. The observation of this statistical almost symmetric break-up of the PLF, should be in agreement with the experimental data. In fact, as we have seen in the previous section, for the two systems, there is a preference for the dynamic break-up, however, for a value of the asymmetry mass around 1, the ratio between dynamic and statistic is smaller respect to the values obtained for the others mass asymmetry parameters. This effect is more pronounced for the neutron-poor system.

Such behavior was also observed by using SIMON instead of GEMINI++ as de-excitation code.

Anyway the calculated cross sections of heavier fragments are obviously lower than the experimental value. Probably HIPSE produces the fragments with an excitation energy too low to be statistically de-excited by $GEMINI ++$ and there is also an underestimation of the contribution of the quasi-fission. These hypotheses can explain the behavior for the neutron-poor system, for which the calculated total fission-like cross section (678 mb) is lower than experimental value (850 mb), in favor of the total fusion-evaporation cross section (627 mb against the 455 mb obtained experimentally). This is not true for the neutron-rich in fact the theoretical predictions fail in the description of the ratio between symmetric and asymmetric fission, in favor of this latter, but the global fission-like cross section (460

mb) is consistent with the experimental value (530 mb). The total fission cross section is evaluated by summing the production cross section of each fragment with $3 \leq Z \leq 28$, while the total evaporation residues contribution is estimated by subtracting the total fission cross section from the total reaction cross section, assuming for the impact parameters the values reproducing the experimental fusion cross section.
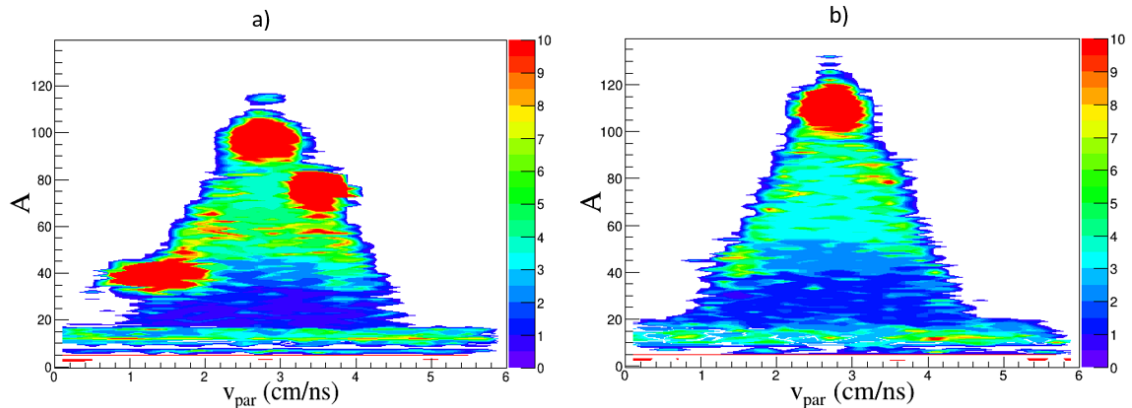

Figure 3.23: Mass (A) vs parallel velocity (v_{par} plot, with the maximum impact parameter obtained the experimental fusion cross sections for the neutron-poor system a) for the neutron-rich one b)

Comparison with $GEMINI + +$ model

GEMINI is a statistical model, developed by Charity [58], which combines the Hauser-Feshbach evaporation formalism [102] with the binary decay formalism. The advantage to use this model is that it consider not only light-particle evaporation and symmetric fission, but all the possible binary-decay modes, taking into account the IMF production. The decay of a compound nucleus is followed through a series of sequential binary decays, until the excitation energy is above the particles separation threshold or particles decay becomes improbable due to γ decay competition. The Moretto's binary-decay formalism, used for the fragment production, works quite well [103] for light system but fails to reproduce the mass distribution of the decay products originating from the symmetric fission of heavy compound nuclei. However, the Moretto formalism is used in GEMINI++ also for the heavier systems, but only for mass-asymmetries outside of the symmetric

fission peak. Otherwise, the total fission yield is obtained from the Bohr-Wheeler formalism [104], and the width of the fission-fragment mass distribution is taken from the systematics compiled by Rusanov [105]. In $GEMINI++$ one of the input parameter is the maximum angular momentum J_{max} . It is possible to fix this quantity by assuming a numerical value or it can be calculated by means of the Bass model [106, 107]. In order to establish a connection with the results of the DNS which will be described later, we started the calculations by taking the same J_{max} values used by the DNS model for the two systems, $73\hbar$ for the n-poor system and $90\hbar$ for the n-rich one. Thus, one assumes that the CN formation occurs up to J_{max} and neglects the contribution of quasi-fission events. A constant value A/7 for the level density parameter is used in all the calculation.
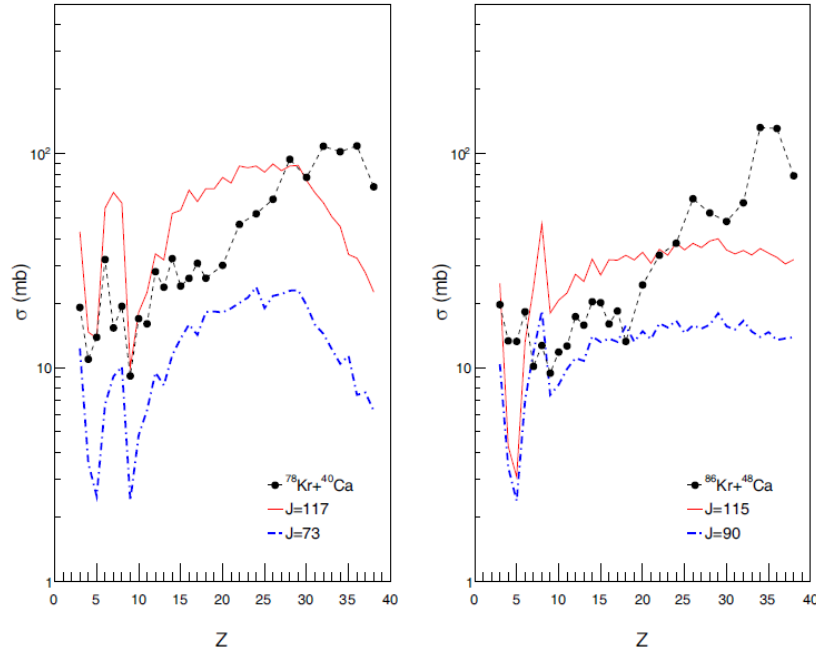
Figure 3.24: Comparison between experimental charge distribution and $GEMINI++$ predictions, with J_{max} equal to $73\hbar$ for the n-poor system and equal to $90\hbar$ for n-rich one (blue dash-dotted lines), and J_{max} obtained by the σ_{fus} (J_{max} = $117\hbar$ and J_{max}= $115\hbar$ for neutron poor and neutron rich systems respectively) (red lines)

In Fig. 3.20 is shown the comparison between the experimental charge distribu-

tions up to Z = 38 for the two systems and the predictions of *GEMINI* + +, obtained with these first values of J_{max} (blue dash-dotted lines). The strong disagreement for heavier fragments (Z>28) can be attributed to the DIC process not considered by the code. Furthermore, production cross section is globally underestimated and the ratio between the light products and almost symmetric fission fragments is not well reproduced, particularly for the neutron rich system. It should be noted that GEMINI++ calculations do not take into account pre-equilibrium effects, which lead to incomplete fusion and can already be significant at 10 AMeV for mass-asymmetric reactions such as those under study. In a second step of the work, we used for the GEMINI++ calculations the values of J_{max} consistent with the measured σ_{fus} and the associated l_{fus} presented in table 3.1. The obtained theoretical predictions for $J_{max} = 117\hbar$ and $J_{max} = 115\hbar$ for neutron poor and neutron rich systems respectively, are presented in Fig. 3.24 with red lines. The calculated values are obviously higher and thus closer to the experimental values, and the deduced global σ_{fus} are very close to experimental values reported in tab3.1, for both systems. Nevertheless, the general behavior of fragments yields does not change with the higher J_{max} , so the balance of the contributions of different mechanisms to the yields is still not very well reproduced.

Comparison with *DNS* model

The DNS model treats the cluster emission as complex fragments emission due to the collective motion of the composite system in the charge (mass) asymmetry coordinate, with additional thermal escape over the Coulomb barrier. The double-folding procedure (with the Skyrme-type density-depending effective nucleon-nucleon interaction) is used for the calculation of the nuclear part of the nucleus -nucleus potential, in the determination of the emission barrier. In this model a dinuclear system is formed, at the stage of capture of the projectile by the target nucleus, after the exchange of nucleons between the two nuclei constituting the dinuclear system. The, so formed, system can evolve or towards a compact configuration, assimilated to the Compound Nucleus formation, which eventually decays by evaporation processes and fission, or towards the energetically possible dinuclear system configurations which decay by quasi-fission. The decay process is traced until all fragments become cold. The maximum angular momentum, compatible with the dinucler system formation, J_{max}, is not an adjustable parameter, but it is determined, within the model, by using the nucleus-nucleus interaction

potential [108] - [111].

The theoretical predictions of the DNS model were compared to the charge distributions experimentally obtained for the systems $^{78,82}Kr + ^{40}Ca$ at 5.5 AMeV incident energy [70, 111]. The model reproduces quite well the experimental data but underestimates the cross sections near the entrance channel, where they are mostly affected by the contributions of the deep inelastic collisions . In this thesis work we present the application of the DNS model for the prediction of the charge distributions of the products detected in $^{78}Kr + ^{40}Ca$ and $^{86}Kr + ^{48}Ca$ at 10 AMeV, already published in [112]. The reaction studied are at higher bombarding energy, thus inevitably the effects of pre-equilibrium emission of light particles start to come into play. Masses, charges, energies and angular momentum carried away, are taken into account in order to consider all the various dinucelar systems produced with different probabilities. For this reason, for the evaluation of the pre-equilibrium emission of light particles, for the first time, the DNS code was combined with the HIPSE model [92], described in the previous section.

The calculated J_{max} values are $73\hbar$ and $90\hbar$ for the reactions $^{78}Kr + ^{40}Ca$ and $^{86}Kr + ^{48}Ca$, respectively. The neutron rich system will present a larger critical angular momentum because by increasing the N/Z ratio of the system the potential pocket becomes deeper. The excitation energies of the CN in these two reactions would be quite different, due to the different Q-value, and they amount to 215 MeV and 270 MeV for the neutron poor and for the neutron rich systems, respectively (neglecting the reduction due to the pre-equilibrium emission). This may reduce the influence of the N/Z ratio of the reactions on the cross sections for final reaction products, due to the increased neutron evaporation from the neutron rich system. To calculate the nuclear temperature, which enters the decay formalism, the asymptotical value (for high excitation energies) of the level density parameter given by Ignatiuk [113], was used corresponding to $a \simeq A/7$. In Fig. 3.25 the comparison between the predictions of the DNS model for the charge distribution of the reaction products with the experimental results, is shown up to Z = 38. The experimental charge distributions don't exhibit a bell shape behavior of the theoretical predictions, because of, as previously discussed, the contamination by a fast dynamic component for heavier residues in the experimental yields. In the un-affected region Z<28, one can indeed see, that the model is unable to fully reproduce the experimental data, though the trend of the charge distribution for lower atomic number is qualitatively described. The same problem was observed in the study of the reaction $^{93}Nb + ^{27}Al$ at 11.4 AMeV [109], where the DNS

model strongly underestimates the production cross sections of the fragments and a proper description of the data, at a quantitative level, would require a very high value of J_{max}. Such quantitative discrepancy between model predictions and experimental data may indicate that the maximum impact parameter used by the model could be too small. The reaction mechanism (complete/incomplete fusion followed by evaporation, fission or quasi-fission) is in fact mostly determined by the angular momentum deposited in the system. According to the DNS model, the complex fragments and the fission-like fragments in the reactions $^{78}Kr + ^{40}Ca$ and $^{86}Kr + ^{48}Ca$ at 10 AMeV mainly originate from the quasi-fission process. The underestimation of the fragment production cross section thus implies that the occurrence of incomplete fusion and quasi-fission events also at impact parameters larger than those used by the mode is possible. The maximum angular momenta used by the DNS (J_{max}= 73ℏ and J_{max} = 90ℏ for neutron poor and neutron rich respectively), are indeed much lower than the l_{fus} deduced for the two systems from the fusion cross sections, reported in table 3.1. This point deserves further investigations. In particular, a comparison with the predictions of stochastic microscopic transport models may be useful in shedding light on reaction mechanisms and the interplay between CN formation, quasi-fission and deep-inelastic processes, as a function of the impact parameter. Quite interestingly, we can see the persistence of odd-even staggering effects in the charge distributions of the reaction products, which is in agreement with the experimental observation, although the amplitude of the staggering is much larger in the calculations. The latter effect may be due to the use of experimental tables for the nuclear masses in the calculations; indeed this discrepancy can be removed by considering the excitation energy dependence of the pairing energy, and by fitting the level density parameter to the experimental results. For example, a change of the level density parameter from A/7 to A/13 will increase the nuclear temperature, making the charge distributions flatter, thus leading to a better agreement with the experimental data. One can also notice that the calculated charge distribution for the neutron rich system is flatter that the one corresponding to the neutron poor system, in agreement with the experimental results. The reason is the different Q-value for fragment production in neutron rich and neutron poor systems. Finally the possible overestimation of pre-equilibrium component calculated by HIPSE could be the origin of the need for an hotter source to reproduce the data.
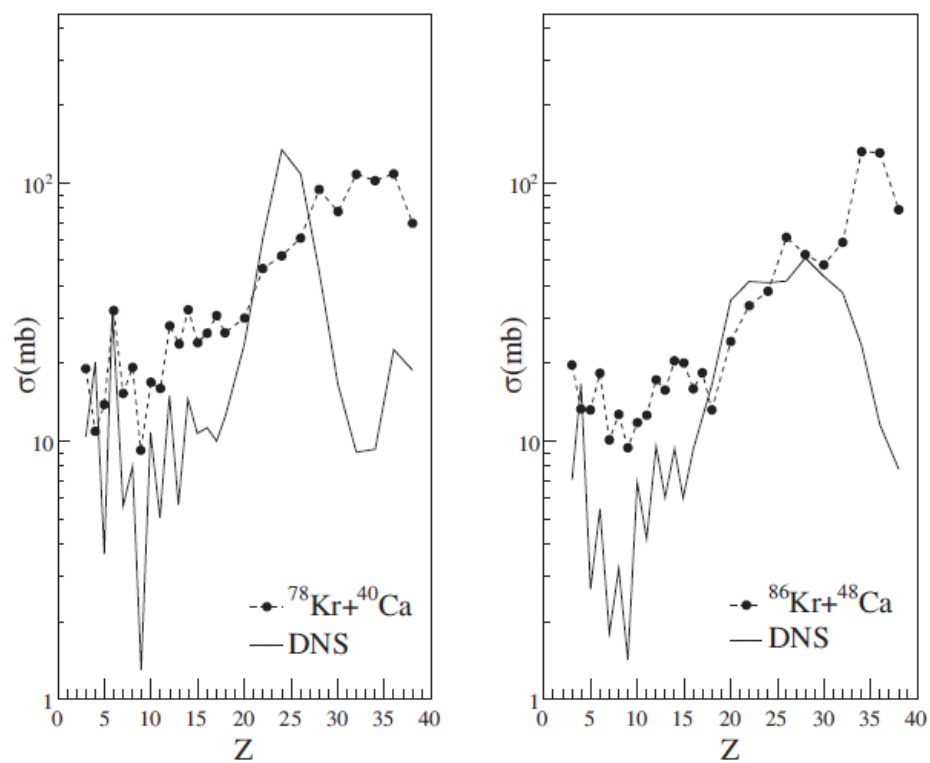
Figure 3.25: Comparison between experimental charge distributions and *DNS* predictions, with J_{max} equal to $73\hbar$ for the n-poor system and equal to $90\hbar$ for n-rich one

Conclusions

In the present thesis work we have shown the principal results of the analysis of the reactions $^{78}Kr +^{40}Ca$ and $^{86}Kr +^{48}Ca$ at laboratory energy of 10 AMeV. The experiment was performed with the 4π multidetector CHIMERA, which is used for the first time in the low energy regime, thanks to the implementation of its identification capabilities (pulse shape discrimination on silicon detectors). We have investigated the isospin influence on the reaction mechanisms in central and semi-peripheral collisions. In particular we have analyzed the Fusion- Evaporation, Fission-like processes and the break-up of the Projectile-like Fragment competitive processes

Very important information on the reaction mechanisms investigated were extracted from the analysis of fragments kinematics features and their angular distributions. Velocity spectra and angular distributions of the reaction products, in the center of mass reference frame, indicated a high relaxation of the degrees of freedom of a long lived source, suggesting the identification of their production mechanisms with Fusion -Fission and Quasi- Fission. The characteristics of the emitted heavier fragments are compatible with a production via an evaporation process following complete and incomplete fusion of the two colliding nuclei. Moreover, a strong enhancement of the yields of the heavier fragments at very forward angles in angular distributions, suggest an overlap with the contribution of a binary process not completely relaxed in mass asymmetry.A deeper study of the latter contributions has to be done by analyzing the coincidences between the reaction products, we will perform this kind of investigation in the future.

By integrating the angular distributions and by applying the normalization factor extracted from the elastic scattering measurements, the production cross sections of each fragment were calculated. In this way the total cross section of each reaction mechanism can be evaluated in both systems, in order to look for differences due to the N/Z degree of freedom. The charge distributions exhibit for fragments

with $Z < 17$ an even-odd effect (*s*taggering), which is more pronounced for the neutron poor system. The neutron enrichment seems to lower the cross sections of the light fragments and thus to inhibit their production mechanisms, as the Fission -Like processes. The obtained angular momentum l_{fus} (given in table 3.1) exceed the values for which fission barrier drops to zero for the two reactions , i.e. $l_{Bf=0} = 90\hbar$ and $l_{Bf=0} = 98\hbar$ for neutron poor and rich respectively. Consequently, these higher partial waves should actually contribute with quasi-fission events. This contribution is clearly stronger in the neutron poor system, which may explain why the cross sections of Fission-Like process, which includes quasi-fission yields, is quite larger in this case.

The experimental production cross sections were compared to the theoretical prediction of different models : HIPSE followed by the statistical code GEMINI++, GEMINI++ and DNS. For these latter two models calculations deviates from data for heavy fragments ($Z > 28$), due to the DIC contamination, not accounted by either of them. In the HIPSE calculation followed by GEMINI++, the choice of a large value for the maximum input parameter selected, permits to take into account also the contribution of binary DIC in neutron poor system. Anyway, also in this case, the predicted cross-sections remain underestimated with respect the experimental data. This can be explained by an underestimation of Quasi-Fission. In DNS model, despite of the well reproduced general trend, the calculated yields are globally lower. We suppose that this can be due mainly to an underestimation in the model of the maximum angular momentum associated with the reaction mechanisms, namely Fusion- Evaporation and Fission-Like processes.

It is important, on light of the current results to compare our data with microscopic transport models giving a different insight on dissipation mechanism and its description.

In the above mentioned reactions we have also investigated the Projectile-Like Fragment (PLF) binary splitting into two massive fragments in non-central collisions, i.e. collisions that do not lead to a compound nucleus formation. In this analysis, first step was the development of a method capable of discriminating binary like-reaction leading to formation of the PLF from to other reaction mechanisms which populate the same region of the phase, i.e. fission of the compound nucleus, fast-fission in di-nuclear like processes. This consists in selecting events with 3 IMFs well identified and detected. By assuming a PLF* break-up in two fragments, we have reconstructed the primary PLF* properties from a pair of fragments. When such a combination gives "good" PLF properties, that is charge and

velocity similar to the ones of the projectile, the third fragments has been taken into account, investigating if it populates kinematical and mass region associated with fusion-fission or the one of the TLF residue. In the latter case, the event can be taken as a deep-inelastic like collsions. In order to study the nature of the PLF break-up, we have looked at the angular distributions of the fragments produced in the splitting of the PLF, in the reference frame of their reconstructed source. We have found a preference for an aligned break-up with the lighter fragment backward emitted, toward the TLF fragment. The asymmetry observed is in favour of a fast non equilibrated splitting of the PLF*, since the preferred splitting direction indicates a memory of preceding reaction step, the binary PLF* + TLF^* mechanism. This a clear signature of the presence of dynamical effects, that are very relevant in the fermi energy regime. It is important to say that when the third fragment populates the region associated to the fusion-fission process, flat-equilibrated angular distributions are found. The angular distributions were evaluated for different mass asymmetry between the 2 fragments coming from the PLF* break-up. More asymmetric is the splitting strongest is the anisotropy observed in the angular distributions. By comparing the two systems, stronger anisotropies have been found in the case of the neutron rich systems. This is in agreement with other experiments, performed at higher energy and with heavier systems, from the CHIMERA collaboration, where the dynamical effect of the PLF breakup resulted to be more pronounced for the neutron-rich system. This preliminary work proves that also at lower energy, dynamical effects can be found in the non-central collisions as reported in the work of Glassel and represent a stimulating point for transport model aiming to reproduce collision dynamical in the low energy regime. A comparison of this observation with model can lead to a better tuning of the parameters aimed to describe the fundamental properties of nuclear matter and microscopic properties of the N-N interaction in this energy regime. The natural evolution of the these new described results on isospin studies underscore the importance to perform the reactions by using radioactive beams, in order to obtain systems with very different N/Z ratios and to investigate the interplay between isospin and nuclear structure. We proposed via a Letter of Intent to perform the reactions $^{92}Kr +^{40,48}Ca$ with the radioactive ion beams produced by the facility SPES at INFN Laboratori Nazionali di Legnaro.

Acknowledgments

There are many people to thank, that supported and guided me in these years, in different ways. First of all, I would like to thank my tutors, Dr. Sara Pirrone and Prof. Francesca Rizzo, not only for their invaluable scientific support but also for helping me in the worst period of my life. Special thanks go to my other scientific guide, Prof. Giuseppe Politi for his precious suggestions and the stimulating discussions. Billions of thanks to Dr. Paolo Russotto and Dr. Enrico De Filippo for the fruitful discussions, in particular for helping me to solve any problems, met during the developing of the software for the analysis of the data. I would like to thank also other members of my research group Dr. Giuseppe Cardella, Dr. Elena Geraci, Prof. Angelo Pagano, Prof. Antonio Trifirò and Prof. Marina Trimarchi for the stimulating discussions and the pleasant time working together.

Special thanks to Prof. Denis Lacroix, working with him has been a fruitful experience in which he taught me the HIPSE model. Thanks a lot to Prof. Jersey Lukasik for kindly welcoming during my stay at IFJ -PAN, in Krakow and for the fruitful discussions. I would like to thank Dr. Konstanze Boretzky and other people from R^3B group with which I worked, for the fruitful scientific experience at GSI. Special thanks to Emanuele and Nancy wonderful colleagues and friends with which I have the pleasure to work. I would like to thank Lucia, Nella, Tommaso, Vicky, Maria and Enrica, always close to me with their precious friendship. I sincerely thank the Big Family, Mauro, Roberta, Alfio, Silvia, Manu and in particular Valentina... thanks to their presence in my life I know that despite everything life can still be beautiful. Thanks a lot also to Anna Maria and Martina...special gifts from Danilo.

I would like to thank Salvo, Rossana and in particular Francesco for their love.

The biggest thanks goes to my parents for always believing in me and for their love which gives me the strength to carry on.

THANKS to Danilo... the missing part of myself...the half of my life...

Bibliography

[1] Durand D, Suraud E and Tamain B., Nuclear dynamics in the nucleonic regime IOP, 2001

[2] Ngo C. and Lefort M.,Ann. De Phys **3**, 5, 1978

[3] Bonasera A.,Phys. Rev. C **34**, 740, 1986

[4] Pirrone S. *et al.*,Eur. Phys Jour. A **55**, 22, 2019

[5] Peilert G., Stocker H. and Greiner W.,Rep. Prog. Phys. **57**, 533, 1994

[6] Guerreau D.,Nucl. Phys. A **447**, 37c, 1985

[7] Dayras D. *et al.*, Nucl. Phys. A **460**, 299, 1986

[8] Dayras D. *et al.*, Phys. Rev. Lett. **62**, 1017, 1989

[9] Nöremberg W. and Weidenmüller H. A.,Lecture Notes in Physics., SpringerVerlag, 1980

[10] Satchler G. R., Introduction to Nuclear Reactions., MacMillan Education LTD, 1990

[11] Povh B. *et al.* Particelle e nuclei, Bollati Boringhieri,1998

[12] Schroder W. U. and Huizenga J. R., Ann. Rev. Nucl. Sci.**27**, 465, 1977

[13] Wilczynski J., Phys. Lett. B **47**, 484, 1973

[14] Trautmann W.*et al.*, Phys. Rev. Lett. **39**, 1062, 1977

[15] Schroder W.*et al.*, Phys. Rep.**45**, 301, 1978

[16] Bohr W., Nature, 137, 1936

[17] National Nuclear Data Center – Brookhaven National Laboratory `www.nndc.bnl.gov`.

[18] Morgenstern H. *et al.*, Phys. Rev. Lett.**52**, 1104, 1984

[19] Borderie B. *et al.*, Z. Phys. A - Atoms and Nuclei **99**, 263, 1981

[20] Zhang H. Q.*et al.*,Phys. Rev. C**81**, 034611, 2010

[21] Cohen S.*et al.*, Ann. Phys. (N.Y.)**82**, 557, 1974

[22] Sierk A. J.*et al.*,Phys. Rev. C**33**, 2039, 1986

[23] Gnoffo B.,Il Nuovo Cimento C**39**, 275, 2016

[24] Politi G. *et al.*, JPS Conf. Proc.**6**, 030082, 2015

[25] Pagano A. *et al.*, Nucl. Phys. A**681**, 331, 2001

[26] Aiello S. *et al.*, Nucl. Phys. A**583**, 461c, 1995

[27] Kemmer J. *et al.*, Nucl. Instr. Meth. A**226**, 89, 1984

[28] Rijken H. A., *et al.*, Nucl. Instr. Meth. B**64**, 271, 1992

[29] Aiello S. *et al.*, Nucl. Instr. Meth. A**369**, 50, 1996

[30] Kreutz P. *et al.*, Nucl. Instr. Meth. A**260**, 120, 1987

[31] Meijer R. J. *et al.*, Nucl. Instr. Meth. A**264**, 285, 1988

[32] Alderighi M. *et al.*, IEEE Trans Nucl. Sci **52**, 1624, 2006

[33] Alderighi M. *et al.*, Nucl. Phys. A**734**, E88, 2004

[34] Aiello S. *et al.*, IEEE Trans Nucl. Sci **45**, 1798, 1998

[35] Aiello S. *et al.*, IEEE Trans Nucl. Sci**45**, 1877, 1998

[36] Aiello S. *et al.*, Nucl. Instr. Meth. B**136**, 1172, 1998

[37] Aiello S. *et al.*, IEEE Trans Nucl. Sci **47**, 114, 2000

[38] Aiello S. *et al.*, IEEE Trans Nucl. Sci **47**, 196, 2000

[39] Alderighi M. *et al.*, IEEE Trans Nucl. Sci **49**, 432, 2002

[40] Bethe H. A., Ann. Phys.**5**, 325 1930.

[41] Guinet M. *et al.*, Nucl. Instr. Meth. A**278**, 614, 1989

[42] Schneider W. F. *et al.*, Nucl. Instr. Meth.**87**, 253, 1970

[43] Lanzalone G textitet al., LNS Activity Report 1252004

[44] Boiano C. *et al.*, IEEE Trans Nucl. Sci **51**, N5, 2004

[45] Emmerich W. D. *et al.*, IEEE Trans Nucl. Sci **83**, 131, 1970

[46] Paush G. *et al.*, Nucl. Instr. Meth. A**337**, 573, 1994

[47] England J. B. A. *et al.*, Nucl. Instr. Meth. A**280**, 291, 1989

[48] Han J., Psd
t Program 2010

[49] Lombardo I. *et al.*, Nucl. Phys. A **834**, 458, 2010

[50] De Filippo E., Pagano A., Eur. Phys. Jour. A **50**, 32, 2014 and the referencce therein.

[51] Russotto P. *et al.*, Phys. Rev. C **81**, 064605, 2010

[52] Beck C, de Toledo A. S., Phys. Rev. C **53**, 1989, 1996

[53] Catchen G. L. *et al.*, J. Chem. Phys. **69**, 1737, 1978

[54] Drake and Gordon W. F.,Handbook of Atomic, Molecular and Optical Physics, Springer. 2005

[55] HO H., Gonthier P. L., Nucl. Instr. Meth. **190**, 75, 1981

[56] Sobotka L. G. *et al.* Phis. Rev. Lett. **51**, 2187, 1983

[57] Moretto G. L., Nucl. Phys. A **247**, 211, 1975

[58] Charity R. J. *et al.*, Nucl. Phys. A **476**, 516 1988

[59] Jing K. X. *et al.*, Nucl. Phys. A **645**, 203, 1999

[60] Auger F.. *et al.*, Phys. Rev. C **35**, 190, 1987

[61] Viola V. E.*et al.*,Phys. Rev. C **31**, 1550, 1985

[62] Hinde D. J. *et al.*, Phys. Rev. C **60**, 054602, 1999

[63] Tarasov O. B., Bazin D., Nucl. Instr. Meth. B **204**, 174, 2003

[64] Blair J. S. *et al.*, Phys. Rev. **95**, 1218, 1954

[65] Frahn W. E. *et al.*, Nucl. Phys. A **302**, 267, 1978

[66] Hinde D. J. *et al.*, Nucl. Phys. A **472**, 318, 1987

[67] Gomez del Campo J., Stokstad R. G., ORNL-TM **7295**, 1981

[68] Gnoffo B.,Il Nuovo Cimento C **41**, 177, 2018

[69] Lombardo I. *et al.* Phys. Rev. C **84**, 024613, 2011

[70] Ademard G. *et al.* Phys. Rev. C **83**, 054619, 2011

[71] Casini G. *et al.* Phys. Rev. C **86**, 011602, 2012

[72] D'Agostino M. *et al.*, Nucl. Phys. A **861**, 47, 2011

[73] Boger J. M. *et al.* Phys. Rev. C **49**, 1597, 1994

[74] Wilcke W. W. *et al.*, Atomic dara and nuclear data tables **25**, 389, 1980

[75] Montoya C. P., Phys. Rev. Lett. **73**, 3070, 1994

[76] Töke J. *et al.*, Phys. Rev. Lett. **75**, 2920, 1995

[77] Stefanini A. A. *et al.*, Zeit Phys. A **351**, 167, 1995

[78] Sobotka L. G. *et al.* Phys. Rev. C **55**, 2109, 1997

[79] Lukasik J. *et al.* Phys. Rev. C **55**, 1906, 1997

[80] De Filippo E. *et al.*, Phys. Rev. C **71**, 044602, 2005

[81] De Filippo E. *et al.*, Phys. Rev. C **71**, 064604, 2005

[82] De Filippo E. *et al.*, ,Il Nuovo Cimento C **42**, 97, 2019

[83] Fleischer R. L. *et al.*, Phys. Rev. **143**, 943, 1966

[84] Becker H. J. *et al.* Phys. Lett. B**50**, 445, 1974

[85] Glässel P. *et al.*, Zeit Phys. A **310**, 189, 1983

[86] Skwira-Chalot I. *et al.* Phys. Rev. Lett. **262701**, 2008

[87] Wilczynski J. *et al.*, Phys. Rev. C**81**, 024605, 2010

[88] Wilczynski J. *et al.*, Phys. Rev. C**81**, 067604, 2010

[89] Russotto P *et al.*, Phys. Rev. C**91**, 014610, 2015

[90] Bocage F. *et al.*, Nucl. Phys. A **676**, 391, 2000

[91] Shvedov L. *et al.* Phys. Rev. C**81**, 054605, 2010

[92] Lacroix D. *et al.* Phys. Rev. C**69**, 054604, 2004

[93] Gross D.. H. E. *et al.*, Rep. Prog. Phys. **53**, 605, 1999

[94] Bondorf J. P. *et al.*, Phys. Rep. **257**, 133, 1995

[95] D'Agostino M. *et al.*, Phys. Lett. B **473**, 219, 2000

[96] Ayik S. *et al.*, Phys. Lett. B **212**, 269, 1988

[97] Guarnera A. *et al.*, Phys. Lett. B **373**, 267, 1996

[98] Ono A. *et al.*, Nucl. Phys. A **630**, 148c, 1998

[99] Durand D. Nucl. Phys. A**451**, 256, 1992

[100] Lacroix D. Private Communication, 2018

[101] Cavata C. *et al.*, Phys. Rev. C**42**, 1760, 1990

[102] Hauser F. Feshbach H. Phys. Rev.**87**, 366, 1952

[103] Mancusi D. *et al.*, Phys. Rev. C**82**, 044610, 2010

[104] Bohr N., Wheeler J. A., Phys. Rev.**56**, 426, 1939

[105] Rusanove A. Y. *et al.*, Phys. At. Nucl.**60**6831997

[106] Bass R., Phys. Lett. B.**47**, 139, 1973

[107] Bass R., Nucl. Phys. A.**231**, 45, 1974

[108] Kalandarov Sh. A. *et al.*, Phys. Rev. C**82**, 044603, 2010

[109] Kalandarov Sh. A. *et al.*, Phys. Rev. C**83**, 054611, 2011

[110] Kalandarov Sh. A. *et al.*, Phys. Rev. C**84**, 054607, 2011

[111] Kalandarov Sh. A. *et al.*, Phys. Rev. C**83**, 064601, 2011

[112] Kalandarov Sh. A. *et al.*, Phys. Rev. C**93**, 024613, 2016

[113] Ignatiuk A. V., Statistical Properties of Excited Atomic Nuclei, Energoizdat Moscow, 1983